# Modelling the floating-catalyst method for carbon nanotube production

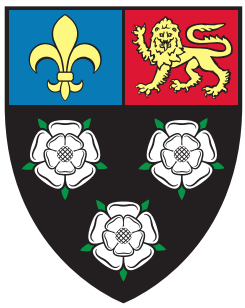

**Filip Karl Arvid Gökstorp**

Supervisor: Prof. Matthew P. Juniper
Advisor: Dr. Adam M. Boies

Department of Engineering
University of Cambridge

This dissertation is submitted for the degree of
*Doctor of Philosophy*

King's College June 2022

*Plötsligt händer det...*

# Declaration

I hereby declare that except where specific reference is made to the work of others, the contents of this dissertation are original and have not been submitted in whole or in part for consideration for any other degree or qualification in this, or any other university. This dissertation is my own work and contains nothing which is the outcome of work done in collaboration with others, except as specified in the text and Acknowledgements. This dissertation contains fewer than 65,000 words including appendices, bibliography, footnotes, tables and equations and has fewer than 150 figures.

Filip Karl Arvid Gökstorp
June 2022

# Acknowledgements

This thesis is the product of a lot of personal toil during a very strange time in history. The start of the thesis was a wonderful time with lots of new friends. The end of the thesis saw some tumultuous world events, beginning with COVID-19 and continuing with the invasion of Ukraine. But I have made it through and I want to thank everyone along the way who helped me.

I start with everyone in the lab. Many thanks to Hans, Jack, Petr, Jose, Max, Francesco, Stefano, Ushnish, Ubaid, Dante, Jenna, Pau, Maxim, Peter, and everyone else. I also want to thank my supervisor, Matthew, for his endless patience with me, and sufficient amount of encouragement.

I also want to thank Fiona, Adarsh, Mabel, Liron, Lee, my advisor Adam, and everyone else in the ANAM project for

All my friends in Cambridge also deserve credit for taking care of me socially. A big thank you to Shaun, Laura, Nathanael, Ollie, Cathy, Tagore, Jeremy, and of course Ada and Sveta.

More academically, I want to thank Adarsh Kaniyoor for the many discussions we had about his work, which helped guide me in my investigation in chapter 7, and Fiona Smail for helping me with understanding her published data, which guided me in chapters 9 and 10.

Finally I want to thank my parents for everything, and especially my brother for putting up with me when I moved to Stockholm in the summer of 2021. It has taking longer than I planned, but now it is finally complete. Suddenly, it happens.

# Abstract

Carbon nanotube fiber, as a material, promises superior material properties to ordinary carbon fiber. It has higher tensile strength, as well as high electrical and thermal conductivity. The production process is implemented in several university rigs, as well as in some industrial settings, but the process is not well understood or modelled physically. This thesis investigates several different components of this process, presents computational models of the key physical processes, and assimilates experimental data into those models in order to improve their accuracy.

The production process consists of a heated quartz reactor tube that is continuously fed with hydrogen, methane, ferrocene, and thiophene. First, a hydrodynamic computational fluid dynamics solver is developed to simulate the flow in the reactor and to model the temperature gradient in the flow. This solver is also extended to model the hydrodynamic stability of the flow through a gas exchange valve attached to the outlet of the production reactor. A simplistic model of the finished carbon nanotube aerogel is presented to evaluate the influence of a convecting solid structure on the flow through the gas valve.

Further detail of the production process is then investigated by calculating the decomposition rate of thiophene from experimental observations. The problem of finding the decomposition rate is set up using a Bayesian inference framework and the resulting objective function is minimised using a gradient-based method. An adjoint method is used to calculate the gradient of the objective function with respect to the model parameters. This decomposition rate of thiophene in a hydrogen atmosphere is then used to compare the decomposition of ferrocene and thiophene in the reactor using two different reactor inlet conditions. The implications for the production of carbon nanotubes are presented.

Finally the nucleation, growth and evaporation of the catalyst nanoparticles in the reactor is investigated. A simple particle model that can quantitatively describe the mass fraction of the particles in the flow is developed. This model is first applied to predict how the radial particle mass fraction distribution varies with flow rate and the input ferrocene concentration. Then the particle model is fitted using the Bayesian inference

framework, again using gradient-based minimisation with an adjoint method to calculate the gradient of the objective function with respect to the model parameters. The implications of the best-fit parameters are discussed, and a parameter set that is closer to the decomposition rate of thiophene than the decomposition rate of ferrocene is found to describe the experimental results best.

The models presented in this study can be used to guide further experimental studies into the carbon nanotube production process, and to improve the design of the reactor used. The adjoint method presented can be applied to other fields in which analytical and quantitative models can be paired with experimental data to improve the model's parameters. Further experimental data can be easily assimilated into the models presented here, because the Bayesian interference framework is a rigorous process to assimilate both new and existing data. Finally this thesis can also explain why the final carbon nanotube product forms a sock-like structure, and highlights that the availability of sulphur is critical to the formation of the catalyst nanoparticles from which carbon nanotubes can grow.

# Table of contents

# List of figures

# List of tables

# Part I

# Introduction

# 1 Background to the Cambridge process for carbon nanotube production

The Cambridge process of producing carbon nanotubes (CNTs) is based on the initial discovery by Li et al. (2004). In this process, shown graphically in figure 1.1, a heated reactor is continuously fed with a working fluid of hydrogen mixed with the CNT feedstock. The CNT feedstock consists of a carbon source, typically methane, an iron source, typically ferrocene, and a sulphur source, typically thiophene. The reactor is heated to high temperatures, typically 1250 °C, which causes the feedstock chemicals to break down into their primary components: carbon, iron, and sulphur. The iron forms into nanoparticles, onto which the released sulphur deposits and promotes the formation of carbon nanotubes. The carbon nanotubes then grow sufficiently long to interact with other carbon nanotubes and tangle together in a two-stage process, first to form bundles in the order of tens of CNTs, second to connect the bundles together in an aerogel. The aerogel is a macroscopic material like a spider web or candy floss (cotton candy). This aerogel can be manually or automatically extracted from the reactor, and collected or further processed.

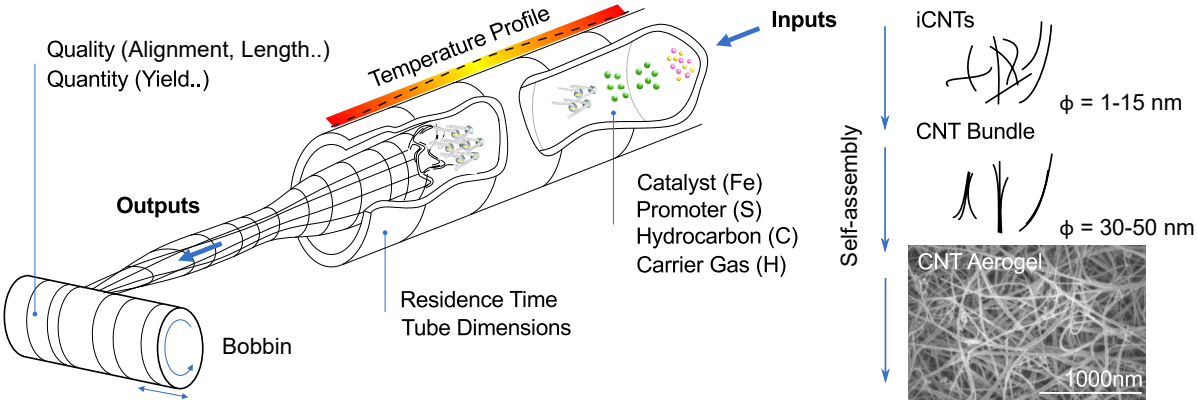


Figure 1.1 The Cambridge process used to produce carbon nanotubes with a single-step floating catalysts chemical vapour deposition process. Diagram adapted from Stallard et al. (2018).

Table 1.1 Comparison of dimensions and typical operating conditions of the CUED and MML reactors.

| | Typical values | | |
|---|---|---|---|
| **Property** | **CUED** | **MML** | **Tortech** |
| Length | 700 mm | 1700 mm | 1605 mm |
| Inner diameter | 40 mm | 65 mm | 85 mm |
| Orientation | horizontal | vertical | vertical |
| Peak temperature | 1250 °C | 1300 °C | 1300 °C |
| Flow rate | 1.0 L min$^{-1}$ | 2.5 L min$^{-1}$ | O(10) L min$^{-1}$ |

## 1.1 The reactors

In this study we examine two different reactor configurations in two different laboratories: the Cambridge University Engineering Department (CUED) reactor, and the Macromolecular Materials Laboratory (MML) reactor (also at the University of Cambridge). Additionally we have briefly investigated the fluid flow in an industrial reactor, operated by Tortech Nano Fibers Ltd. The length, diameter, and operating conditions of the reactor vary between different laboratories. The dimensions and typical operating conditions are listed in table 1.1. Figure 1.2 shows the reactor dimensions to scale. The wall temperature profile of each reactor is shown in figure 1.3.

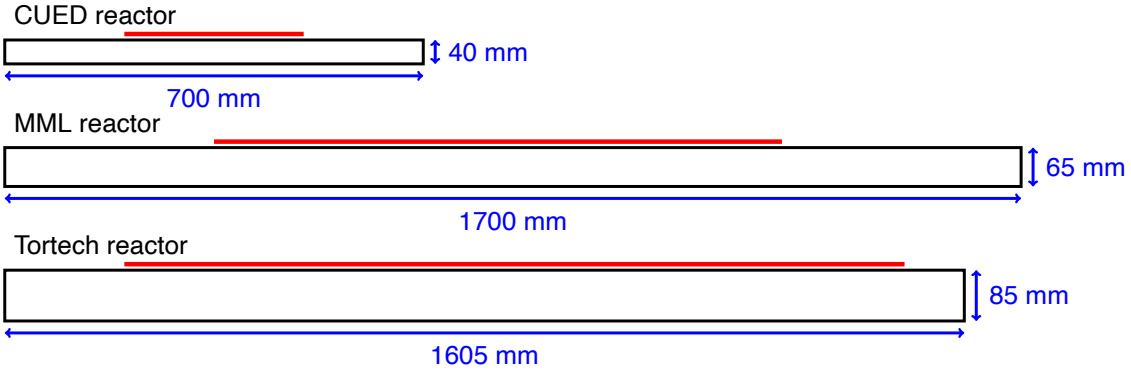


Figure 1.2 Diagrams of the three reactors investigated and their relative dimensions. The red line above each reactor gives the approximate region where the wall temperature exceeds 1000 °C.

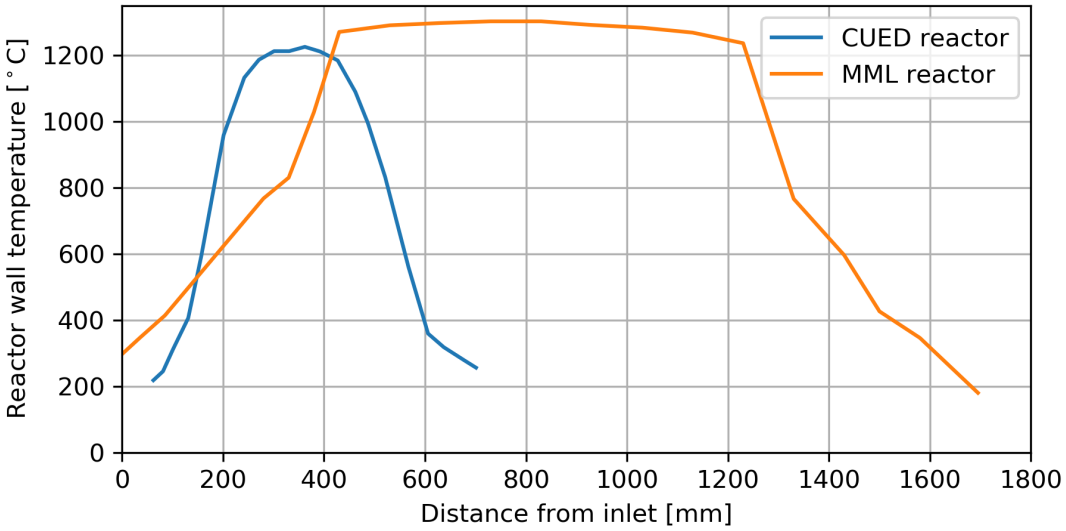


Figure 1.3 The measured wall temperature of the CUED and MML reactors plotted against the distance from the reactor inlet.

### The CUED reactor

We investigate the CUED reactor most thoroughly in this study. It is the shortest and narrowest of the three with a length of 700 mm and an inner diameter of 40 mm. The flowrate is typically 1.0 L min$^{-1}$ and the peak temperature is typically 1250 °C. The reactor tube is arranged horizontally and heated by a clam-shell furnace. To prevent the hydrogen from venting directly into the laboratory the end of the reactor is attached to a gas valve that extracts the hydrogen rich gas before it can exit into the laboratory, diluting it sufficiently so as not to pose an explosion risk. This reactor was previously studied by Hoecker et al. (2016, 2017a,b).

### The MML reactor

The second reactor we investigate is the MML reactor. It is the longest reactor with a length of 1700 mm and an inner diameter of 65 mm. The flowrate is typically 2.5 L min$^{-1}$ and the peak temperature is typically 1300 °C. The reactor is arranged vertically and heated by rods. A gas valve is attached to the end of the reactor in order to dilute the reactor fluid. The reactor was studied by Bulmer et al. (2020); Kaniyoor et al. (2019); Li et al. (2004), and a similar reactor was studied by Conroy et al. (2010).

### The Tortech reactor

A third reactor is investigated briefly. It is used for industrial production of CNTs by Tortech Nano Fibers Ltd. It has a length of 1605 mm and an inner diameter of 85 mm. The flowrate is an order of magnitude higher than the flowrates used by the CUED and MML reactors. The peak temperature is similar, at 1300 °C. This reactor is arranged vertically and is run without a gas valve in order to minimise the disruption to the CNT production. Instead the production environment is kept isolated while the reactor is running.

## 1.2 Motivation and objectives

This study is part of the ANAM initiative, which is a collaboration between the University of Cambridge, the University of Ulster, and several industrial partners. The research goal of the ANAM initiative is to work towards a commercial realisation of producing CNTs using the Cambridge process. CNTs promise significant improvements of mechanical (Koziol et al., 2007; Motta et al., 2007b), electrical (Sundaram et al., 2011), and thermal (Gspann et al., 2017) properties compared to alternative organic materials.

To present the Cambridge process, and CNT production in general, as a viable commercial endeavour the production capability of the Cambridge process needs to scale up. Current production capability is in the order of a few grammes of CNTs per day. For commercial viability, the yield of the process needs to scale up by several orders of magnitude. This thesis is motivated by this aim to scale up the production of CNTs. The focus is on understanding the underlying precursor and particle dynamics in the reactor and developing a model which will guide further practical work. This thesis presents:

i) an investigation of the fluid mechanics of the gas valve: how to recycle reactor gas while operating safely (chapter 4),

ii) a simplistic model of the aerogel: to understand the motion of the aerogel during extraction (chapter 5),

iii) a model of the decomposition of the precursors (ferrocene and thiophene): to better understand how the release of iron and sulphur impacts the production of the catalyst nanoparticles (chapters 6 and 7),

iv) a model of the nucleation, growth, and evaporation of the iron nanoparticles: to predict how the reactor parameters (flowrate, temperature, and iron input) affect the nanoparticle properties (chapters 8, 9, and 10),

v) the application of a Bayesian framework to the models: to update the precursor and particle models as experimental data is made available (chapters 2, 6, and 10).

# 2 Designing CFD for optimisation

To understand how the carbon nanotube aerogel is produced in the Cambridge process, we develop a computational model of the fluid and particle dynamics inside the reactor. We use computational fluid dynamics (CFD) to solve the fluid problem and find the velocity, pressure, density, and temperature fields in the reactor (chapter 3). In chapter 6 we model the decomposition of the process precursors and compare the model results with experimental data. Then in chapter 8 we simulate the creation and growth of particles in the reactor. In chapter 9 we compare the models to experimental data of the particle mass measured in the reactors. In chapter 10 we optimise the model parameters to minimise the discrepancy between the experiments and the model predictions.

We use a gradient-base optimisation method to speed up the optimisation process. We design our CFD to calculate the gradients more cheaply than a finite-difference method. For this we use the adjoint method, which allows us to solve a linear set of equations in order to calculate the gradient of an objective function with respect to model parameters. We use finite elements to solve the governing equations, because the weak form is well suited to applications of the adjoint equations.

## 2.1 The numerical computer code

The ability to construct adjoint equations from a direct code and an objective function is not common in existing commercial CFD codes, so we develop a new code in Python based on the finite-element partial-differential equation solving framework `FEniCS` (Alnæs et al., 2015; Logg et al., 2012). The developed code is supplemented with a meshing program, `Gmsh` (Geuzaine and Remacle, 2009), and its Python wrapper `PyGmsh` (Schlömer et al., 2018). The numerical solutions are found using `PETSc` (Abhyankar et al., 2018). The eigenvalue solver `SLEPc` (Hernandez et al., 2005) is used for stability analysis.

## 2.2 Introduction to adjoints

The adjoint variables are Lagrangian multipliers, and the governing equations that define the adjoint variables are the adjoint equations. The main benefit of using the adjoint equations and variables to find the gradient of an objective function is that the gradient expression is a simple product or integral involving the adjoint variable, and the adjoint governing equations are linear and only need to be solved once per iteration. This means the gradient information only requires a single extra *linear* solution. In contrast, a finite-difference approach for finding the gradient information requires a nonlinear solution of the original problem for each parameter. As the number of parameters in the problem increases, the computational savings of using adjoints becomes very significant.

To explain how adjoints are used, we present an abstracted optimisation problem, inspired by Lemke et al. (2014). We start with an objective function, $J$, that is a function of a set of model variables, $\boldsymbol{s}$:

$$J = J(\boldsymbol{s}), \tag{2.1}$$

where the objective function is a real scalar value.

The model variables are in turn a function of the model parameters, $\boldsymbol{\theta}$, because they fulfil a set of governing equations which are parameterised by $\boldsymbol{\theta}$:

$$G(\boldsymbol{s}, \boldsymbol{\theta}) = 0, \tag{2.2}$$

$$J = J(\boldsymbol{s}(\boldsymbol{\theta})). \tag{2.3}$$

Next we linearise the governing equations $G$ and the objective function $J$ around a fixed solution $(\boldsymbol{s}, \boldsymbol{\theta}) = (\boldsymbol{s}_0, \boldsymbol{\theta}_0) + (\delta\boldsymbol{s}, \delta\boldsymbol{\theta})$:

$$\delta G = \frac{\partial G}{\partial \boldsymbol{s}}\delta\boldsymbol{s} + \frac{\partial G}{\partial \boldsymbol{\theta}}\delta\boldsymbol{\theta} = 0, \tag{2.4}$$

$$\delta J = \frac{\partial J}{\partial \boldsymbol{s}}\delta\boldsymbol{s} + \frac{\partial J}{\partial \boldsymbol{\theta}}\delta\boldsymbol{\theta} = 0. \tag{2.5}$$

We add the constraint on $\delta \boldsymbol{s}$, (2.4), to (2.5), multiplied by a Lagrangian multiplier, $\boldsymbol{\lambda}$, to construct the Lagrangian:

$$\begin{aligned}\delta L &= \delta J + \langle \boldsymbol{\lambda}, \delta G \rangle && (2.6)\\ &= \frac{\partial J}{\partial \boldsymbol{s}}\delta \boldsymbol{s} + \frac{\partial J}{\partial \boldsymbol{\theta}}\delta \boldsymbol{\theta} + \left\langle \boldsymbol{\lambda}, \frac{\partial G}{\partial \boldsymbol{s}}\delta \boldsymbol{s} + \frac{\partial G}{\partial \boldsymbol{\theta}}\delta \boldsymbol{\theta} \right\rangle = 0, && (2.7)\\ &= \left\langle \delta \boldsymbol{s}, \frac{\partial J}{\partial \boldsymbol{s}}^{\top} + \frac{\partial G}{\partial \boldsymbol{s}}^{\top} \boldsymbol{\lambda} \right\rangle + \frac{\partial J}{\partial \boldsymbol{\theta}}\delta \boldsymbol{\theta} + \left\langle \boldsymbol{\lambda}, \frac{\partial G}{\partial \boldsymbol{\theta}} \right\rangle, && (2.8)\end{aligned}$$

where $\langle \cdot, \cdot \rangle$ is an inner product appropriate to the space $\boldsymbol{s}$ resides in. In the cases looked at in this thesis a volume integral is used.

The value of the Lagrangian multiplier $\boldsymbol{\lambda}$ is arbitrary. We chose $\boldsymbol{\lambda}$ to fulfil an adjoint governing equation in order to remove the dependency of $\delta L$ on $\delta \boldsymbol{s}$:

$$\frac{\partial J}{\partial \boldsymbol{s}}^{\top} + \frac{\partial G}{\partial \boldsymbol{s}}^{\top} \boldsymbol{\lambda} = 0. \tag{2.9}$$

This governing equation allows us to solve for the Lagrangian multiplier $\boldsymbol{\lambda}$, which we now call the adjoint variable. The adjoint variable can then be used to find the gradient of the objective function $J$ with respect to the model parameters $\boldsymbol{\theta}$, through the Lagrangian:

$$\frac{\delta L}{\delta \boldsymbol{\theta}} = \frac{\partial J}{\partial \boldsymbol{\theta}} + \left\langle \boldsymbol{\lambda}, \frac{\partial G}{\partial \boldsymbol{\theta}} \right\rangle. \tag{2.10}$$

Higher order gradients can be found in the same manner as the first order gradient was constructed. Here we present an approach inspired by Papadimitriou and Giannakoglou (2008).

To find the second-order gradient, we first linearise (2.9) and (2.10) around a point $(\boldsymbol{s}, \boldsymbol{\theta}, \boldsymbol{\lambda}) = (\boldsymbol{s}_0, \boldsymbol{\theta}_0, \boldsymbol{\lambda}_0) + (\delta \boldsymbol{s}, \delta \boldsymbol{\theta}, \delta \boldsymbol{\lambda})$:

$$\begin{aligned}&\delta \left( \frac{\partial J}{\partial \boldsymbol{s}}^{\top} + \frac{\partial G}{\partial \boldsymbol{s}}^{\top} \boldsymbol{\lambda} \right) = \\ &\quad \left( \frac{\partial^2 J}{\partial \boldsymbol{s} \partial \boldsymbol{\theta}}^{\top} + \frac{\partial^2 G}{\partial \boldsymbol{s} \partial \boldsymbol{\theta}}^{\top} \boldsymbol{\lambda} \right) \delta \boldsymbol{\theta} + \left( \frac{\partial^2 J}{\partial \boldsymbol{s}^2}^{\top} + \frac{\partial^2 G}{\partial \boldsymbol{s}^2}^{\top} \boldsymbol{\lambda} \right) \delta \boldsymbol{s} + \frac{\partial G}{\partial \boldsymbol{s}}^{\top} \delta \boldsymbol{\lambda} = 0, \qquad (2.11)\end{aligned}$$

and

$$\delta\left(\frac{\delta L}{\delta \boldsymbol{\theta}}\right) = \frac{\partial^2 J}{\partial \boldsymbol{\theta}^2}\delta\boldsymbol{\theta} + \frac{\partial^2 J}{\partial \boldsymbol{\theta}\partial \boldsymbol{s}}\delta\boldsymbol{s} + \left\langle \delta\boldsymbol{\lambda}, \frac{\partial G}{\partial \boldsymbol{\theta}}\right\rangle + \left\langle \boldsymbol{\lambda}, \frac{\partial^2 G}{\partial \boldsymbol{\theta}^2}\delta\boldsymbol{\theta}\right\rangle + \left\langle \boldsymbol{\lambda}, \frac{\partial^2 G}{\partial \boldsymbol{\theta}\partial \boldsymbol{s}}\delta\boldsymbol{s}\right\rangle, \tag{2.12}$$

$$= \left(\frac{\partial^2 J}{\partial \boldsymbol{\theta}^2} + \left\langle \boldsymbol{\lambda}, \frac{\partial^2 G}{\partial \boldsymbol{\theta}^2}\right\rangle\right)\delta\boldsymbol{\theta} + \left(\frac{\partial^2 J}{\partial \boldsymbol{\theta}\partial \boldsymbol{s}} + \left\langle \boldsymbol{\lambda}, \frac{\partial^2 G}{\partial \boldsymbol{\theta}\partial \boldsymbol{s}}\right\rangle\right)\delta\boldsymbol{s} + \left\langle \delta\boldsymbol{\lambda}, \frac{\partial G}{\partial \boldsymbol{\theta}}\right\rangle \tag{2.13}$$

We now add the equation governing $\delta\boldsymbol{\lambda}$ (2.11), multiplied by a Lagrangian multiple $\boldsymbol{\phi}$, and the equation governing $\delta\boldsymbol{s}$ (2.4), multiplied by a Lagrangian multiple $\boldsymbol{\psi}$, to (2.13), to construct the second order Lagrangian:

$$\begin{aligned}
\delta\left(\frac{\delta L}{\delta \boldsymbol{\theta}}\right) &= \left(\frac{\partial^2 J}{\partial \boldsymbol{\theta}^2} + \left\langle \boldsymbol{\lambda}, \frac{\partial^2 G}{\partial \boldsymbol{\theta}^2}\right\rangle\right)\delta\boldsymbol{\theta} + \left(\frac{\partial^2 J}{\partial \boldsymbol{\theta}\partial \boldsymbol{s}} + \left\langle \boldsymbol{\lambda}, \frac{\partial^2 G}{\partial \boldsymbol{\theta}\partial \boldsymbol{s}}\right\rangle\right)\delta\boldsymbol{s} + \left\langle \delta\boldsymbol{\lambda}, \frac{\partial G}{\partial \boldsymbol{\theta}}\right\rangle \\
&\quad + \left\langle \boldsymbol{\phi}, \left(\frac{\partial^2 J}{\partial \boldsymbol{s}\partial \boldsymbol{\theta}}^{\top} + \frac{\partial^2 G}{\partial \boldsymbol{s}\partial \boldsymbol{\theta}}^{\top}\boldsymbol{\lambda}\right)\delta\boldsymbol{\theta} + \left(\frac{\partial^2 J}{\partial \boldsymbol{s}^2}^{\top} + \frac{\partial^2 G}{\partial \boldsymbol{s}^2}^{\top}\boldsymbol{\lambda}\right)\delta\boldsymbol{s} + \frac{\partial G}{\partial \boldsymbol{s}}^{\top}\delta\boldsymbol{\lambda}\right\rangle \\
&\quad + \left\langle \boldsymbol{\psi}, \frac{\partial G}{\partial \boldsymbol{s}}\delta\boldsymbol{s} + \frac{\partial G}{\partial \boldsymbol{\theta}}\delta\boldsymbol{\theta}\right\rangle, \qquad (2.14) \\
&= \left(\frac{\partial^2 J}{\partial \boldsymbol{\theta}^2} + \left\langle \boldsymbol{\lambda}, \frac{\partial^2 G}{\partial \boldsymbol{\theta}^2}\right\rangle\right)\delta\boldsymbol{\theta} + \left\langle \boldsymbol{\phi}, \frac{\partial^2 J}{\partial \boldsymbol{s}\partial \boldsymbol{\theta}}^{\top} + \frac{\partial^2 G}{\partial \boldsymbol{s}\partial \boldsymbol{\theta}}^{\top}\boldsymbol{\lambda}\right\rangle\delta\boldsymbol{\theta} + \left\langle \boldsymbol{\psi}, \frac{\partial G}{\partial \boldsymbol{\theta}}\right\rangle\delta\boldsymbol{\theta} \\
&\quad + \left\langle \boldsymbol{\psi}, \frac{\partial G}{\partial \boldsymbol{s}}\delta\boldsymbol{s}\right\rangle + \frac{\partial^2 J}{\partial \boldsymbol{\theta}\partial \boldsymbol{s}}\delta\boldsymbol{s} + \left\langle \boldsymbol{\lambda}, \frac{\partial^2 G}{\partial \boldsymbol{\theta}\partial \boldsymbol{s}}\delta\boldsymbol{s}\right\rangle + \left\langle \boldsymbol{\phi}, \frac{\partial^2 J}{\partial \boldsymbol{s}^2}^{\top}\delta\boldsymbol{s} + \left(\frac{\partial^2 G}{\partial \boldsymbol{s}^2}^{\top}\boldsymbol{\lambda}\right)\delta\boldsymbol{s}\right\rangle \\
&\quad + \left\langle \delta\boldsymbol{\lambda}, \frac{\partial G}{\partial \boldsymbol{\theta}}\right\rangle + \left\langle \boldsymbol{\phi}, \frac{\partial G}{\partial \boldsymbol{s}}^{\top}\delta\boldsymbol{\lambda}\right\rangle \qquad (2.15) \\
&= \left(\frac{\partial^2 J}{\partial \boldsymbol{\theta}^2} + \left\langle \boldsymbol{\lambda}, \frac{\partial^2 G}{\partial \boldsymbol{\theta}^2}\right\rangle + \left\langle \boldsymbol{\phi}, \frac{\partial^2 J}{\partial \boldsymbol{s}\partial \boldsymbol{\theta}}^{\top}\right\rangle + \left\langle \boldsymbol{\phi}, \frac{\partial^2 G}{\partial \boldsymbol{s}\partial \boldsymbol{\theta}}^{\top}\boldsymbol{\lambda}\right\rangle + \left\langle \boldsymbol{\psi}, \frac{\partial G}{\partial \boldsymbol{\theta}}\right\rangle\right)\delta\boldsymbol{\theta} \\
&\quad + \left\langle \delta\boldsymbol{s}, \frac{\partial G}{\partial \boldsymbol{s}}^{\top}\boldsymbol{\psi} + \frac{\partial^2 J}{\partial \boldsymbol{\theta}\partial \boldsymbol{s}}^{\top} + \frac{\partial^2 G}{\partial \boldsymbol{\theta}\partial \boldsymbol{s}}^{\top}\boldsymbol{\lambda} + \frac{\partial^2 J}{\partial \boldsymbol{s}^2}\boldsymbol{\phi} + \boldsymbol{\lambda}^{\top}\frac{\partial^2 G}{\partial \boldsymbol{s}^2}\boldsymbol{\phi}\right\rangle \\
&\quad + \left\langle \delta\boldsymbol{\lambda}, \frac{\partial G}{\partial \boldsymbol{\theta}} + \frac{\partial G}{\partial \boldsymbol{s}}\boldsymbol{\phi}\right\rangle. \qquad (2.16)
\end{aligned}$$

As before, we choose the Lagrangian multipliers to satisfy an equation in order to eliminate the terms involving $\delta\boldsymbol{s}$ and $\delta\boldsymbol{\lambda}$:

$$\frac{\partial G}{\partial \boldsymbol{s}}^{\top}\boldsymbol{\psi} + \frac{\partial^2 J}{\partial \boldsymbol{\theta}\partial \boldsymbol{s}}^{\top} + \frac{\partial^2 G}{\partial \boldsymbol{\theta}\partial \boldsymbol{s}}^{\top}\boldsymbol{\lambda} + \frac{\partial^2 J}{\partial \boldsymbol{s}^2}\boldsymbol{\phi} + \boldsymbol{\lambda}^{\top}\frac{\partial^2 G}{\partial \boldsymbol{s}^2}\boldsymbol{\phi} = 0, \tag{2.17}$$

$$\frac{\partial G}{\partial \boldsymbol{\theta}} + \frac{\partial G}{\partial \boldsymbol{s}}\boldsymbol{\phi} = 0. \tag{2.18}$$

This leaves the second-order Lagrangian as:

$$\delta\left(\frac{\delta L}{\delta \boldsymbol{\theta}}\right) = \left(\frac{\partial^2 J}{\partial \boldsymbol{\theta}^2} + \left\langle \boldsymbol{\lambda}, \frac{\partial^2 G}{\partial \boldsymbol{\theta}^2} \right\rangle + \left\langle \boldsymbol{\phi}, \frac{\partial^2 J}{\partial \boldsymbol{s}\partial \boldsymbol{\theta}}^\top + \frac{\partial^2 G}{\partial \boldsymbol{s}\partial \boldsymbol{\theta}}^\top \boldsymbol{\lambda} \right\rangle + \left\langle \boldsymbol{\psi}, \frac{\partial G}{\partial \boldsymbol{\theta}} \right\rangle\right) \delta\boldsymbol{\theta}, \tag{2.19}$$

$$\frac{\delta^2 L}{\delta \boldsymbol{\theta}^2} = \frac{\partial^2 J}{\partial \boldsymbol{\theta}^2} + \left\langle \boldsymbol{\lambda}, \frac{\partial^2 G}{\partial \boldsymbol{\theta}^2} \right\rangle + \left\langle \boldsymbol{\phi}, \frac{\partial^2 J}{\partial \boldsymbol{s}\partial \boldsymbol{\theta}}^\top + \frac{\partial^2 G}{\partial \boldsymbol{s}\partial \boldsymbol{\theta}}^\top \boldsymbol{\lambda} \right\rangle + \left\langle \boldsymbol{\psi}, \frac{\partial G}{\partial \boldsymbol{\theta}} \right\rangle. \tag{2.20}$$

## 2.3 Optimisation in a Bayesian framework

Using an optimisation technique, which may use gradients, one can find the parameters that achieve a local minimum of the objective function. This can be used to minimise the discrepancy between a set of observation points $\boldsymbol{x}$ and the model predictions $\boldsymbol{q} = \boldsymbol{q}(\boldsymbol{s})$:

$$J \equiv \tfrac{1}{2}(\boldsymbol{x} - \boldsymbol{q})^\top (\boldsymbol{x} - \boldsymbol{q}). \tag{2.21}$$

We use the optimisation for statistical inference by working in a Bayesian framework (MacKay, 2003). We first create a model $H$ *a priori*, with a corresponding set of parameters $\boldsymbol{\theta}$. We set a prior value of these parameters, based on prior knowledge. We assume that the probability distribution of the parameter values is Gaussian, which enables us to express the prior probability of the parameters, given the model $H$:

$$P(\boldsymbol{\theta} \mid H) = \tfrac{1}{Z_{\boldsymbol{\theta}}} \exp\left(-\tfrac{1}{2}(\boldsymbol{\theta} - \boldsymbol{\mu}_{\boldsymbol{\theta}})^\top \boldsymbol{\Sigma}_{\boldsymbol{\theta}}^{-1} (\boldsymbol{\theta} - \boldsymbol{\mu}_{\boldsymbol{\theta}})\right), \tag{2.22}$$

where $\boldsymbol{\mu}_{\boldsymbol{\theta}}$ is the mean of the probability distribution, $\boldsymbol{\Sigma}_{\boldsymbol{\theta}}$ is the uncertainty of the probability distribution, and $Z_{\boldsymbol{\theta}} = |2\pi\boldsymbol{\Sigma}_{\boldsymbol{\theta}}|^{-1/2}$ is the normalisation constant of the Gaussian distribution.

We assume that the experimental observation are noisy samples around some ground truth value, and that the noise follows a Gaussian distribution. We further assume that the chosen model $H$ is able to match the ground truth values, with an optimal set of parameters $\boldsymbol{\theta}$. Using these assumptions, we phrase the optimisation problem as finding the maximum *a posteriori* probability of the parameters given the data: $\max_{\boldsymbol{\theta}} P(\boldsymbol{\theta} \mid \boldsymbol{x}, H)$. This posterior probability is derived from the likelihood of the parameters, $P(\boldsymbol{x} \mid$

$\boldsymbol{\theta}, H)$, and the prior probability of the parameters, $P(\boldsymbol{\theta} \mid H)$, using Bayes' rule:

$$P(\boldsymbol{\theta} \mid \boldsymbol{x}, H) = \frac{P(\boldsymbol{\theta} \mid H) P(\boldsymbol{x} \mid \boldsymbol{\theta}, H)}{P(\boldsymbol{x} \mid H)}, \tag{2.23}$$

where $P(\boldsymbol{x} \mid H)$ is the probability of the data over all parameters of model $H$, called the evidence:

$$P(\boldsymbol{x} \mid H) = \int P(\boldsymbol{\theta} \mid H) P(\boldsymbol{x} \mid \boldsymbol{\theta}, H) \, \mathrm{d}\boldsymbol{\theta} = Z_H. \tag{2.24}$$

At this stage we do not need to compute $Z_H$, and instead treat it as a normalising constant.

We assume the likelihood can be modelled as a Gaussian distribution:

$$P(\boldsymbol{x} \mid \boldsymbol{\theta}, H) = \tfrac{1}{Z_{\boldsymbol{x}}} \exp\left(-\tfrac{1}{2} (\boldsymbol{x} - \boldsymbol{q})^\top \boldsymbol{\Sigma}_{\boldsymbol{x}}^{-1} (\boldsymbol{x} - \boldsymbol{q})\right), \tag{2.25}$$

where $\boldsymbol{q}$ is the model predictions using model $H$ and parameters $\boldsymbol{\theta}$, $\boldsymbol{\Sigma}_{\boldsymbol{x}}$ is the variance of the experimental observations, and $Z_{\boldsymbol{x}} = |2\pi\boldsymbol{\Sigma}_{\boldsymbol{x}}|^{-1/2}$ is the normalising constant.

We take the negative log of the posterior distribution, which allows us to construct an objective function similar to (2.21):

$$\begin{aligned}
-\log P(\boldsymbol{\theta} \mid \boldsymbol{x}, H) &= \log P(\boldsymbol{x} \mid H) - \log P(\boldsymbol{\theta} \mid H) - \log P(\boldsymbol{x} \mid \boldsymbol{\theta}, H) && (2.26)\\
&= \underbrace{\log Z_H + \log Z_{\boldsymbol{\theta}} + \log Z_{\boldsymbol{x}}}_{\text{independent of } \boldsymbol{\theta}} \\
&\quad + \tfrac{1}{2}(\boldsymbol{\theta} - \boldsymbol{\mu}_{\boldsymbol{\theta}})^\top \boldsymbol{\Sigma}_{\boldsymbol{\theta}}^{-1} (\boldsymbol{\theta} - \boldsymbol{\mu}_{\boldsymbol{\theta}}) + \underbrace{\tfrac{1}{2} (\boldsymbol{x} - \boldsymbol{q})^\top \boldsymbol{\Sigma}_{\boldsymbol{x}}^{-1} (\boldsymbol{x} - \boldsymbol{q})}_{\text{equivalent to (2.21) with weights } \boldsymbol{\Sigma}_{\boldsymbol{x}}^{-1}} && (2.27)\\
&= J(\boldsymbol{\theta}, \boldsymbol{x}). && (2.28)
\end{aligned}$$

This expression becomes the new objective function, which now has a contribution from how well the model describes the experimental observations, and how close the parameters agree with the prior expectation. Using the first-order adjoints we converge to the parameters with the highest posterior probability.

Using the second-order adjoints, or an approximation of the second-order gradient information, we can use Laplace's method (MacKay, 2003, Chapter 27) to obtain the uncertainty of the fitted parameters. Additionally, the marginal likelihood of the model

$H$ can be calculated (MacKay, 2003, Chapter 28), and compared with other models. This way the model with the highest likelihood can be found.

## 2.4 Brief overview of optimisation techniques

A brief overview of the optimisation techniques used in this study is presented here. A more complete overview can be found in Nocedal and Wright (1999). The goal of optimisation is to find a set of parameters $\boldsymbol{\theta}$ that produces the optimal value of an objective function $J$. Canonically the objective function is constructed so that the optimal value is the minimum value:

$$\min_{\boldsymbol{\theta}} J(\boldsymbol{\theta}). \tag{2.29}$$

A typical procedure for optimisation is to:

1. find a search direction $\boldsymbol{d}$,
2. move a distance $\alpha$ in the search direction $\boldsymbol{\theta}' = \boldsymbol{\theta} + \alpha\boldsymbol{d}$,
3. evaluate the objective function at the new parameters, $J' = J(\boldsymbol{\theta}')$,
4. check if the algorithm should end, otherwise repeat from 1.

When gradient information is available the optimisation can be improved by searching in a direction suggested by the gradient. A straightforward method is to search in the direction of steepest descent, by setting the search direction to the negative of the gradient:

$$\boldsymbol{d} = -\boldsymbol{\nabla} J. \tag{2.30}$$

The step length $\alpha$ can be found by minimising $J$ along the search direction:

$$\min_{\alpha} J(\boldsymbol{\theta} + \alpha\boldsymbol{d}). \tag{2.31}$$

To avoid having to run a secondary minimisation at each iteration, we instead use the Wolfe conditions to find a suitable approximation of the optimal step length $\alpha$. First a large value of $\alpha$ is tested, and successively decreased until the *sufficient decrease* and

*curvature* conditions are met:

$$J(\boldsymbol{\theta} + \alpha \boldsymbol{d}) - J(\boldsymbol{\theta}) \leq c_1 \alpha \boldsymbol{\nabla} J^\top \boldsymbol{d}, \tag{2.32}$$

$$\boldsymbol{\nabla} J(\boldsymbol{\theta} + \alpha \boldsymbol{d})^\top \boldsymbol{d} \geq c_2 \boldsymbol{\nabla} J(\boldsymbol{\theta})^\top \boldsymbol{d}, \tag{2.33}$$

where $c_1$ and $c_2$ are constants which satisfy $0 < c_1 < c_2 < 1$. We have found that $c_1 = 10 \times 10^{-6}$ and $c_2 = 0.95$ produce good results.

If second order derivatives are available, the Newton method can be used, wherein the search direction and length is the negative of the gradient, multiplied by the inverse of the Hessian (the second derivative matrix, $\boldsymbol{\nabla}^2 J$):

$$\alpha \boldsymbol{d} = -(\boldsymbol{\nabla}^2 J)^{-1} \boldsymbol{\nabla} J. \tag{2.34}$$

The Newton method jumps directly to the minimum of the local parabolic approximation of the objective function $J$. If this parabolic approximation is accurate the Newton method significantly speeds up the optimisation. If not, the Newton method often diverges.

The Hessian can be approximated using the Broyden-Fletcher-Goldfarb-Shanno (BFGS) formula (Nocedal and Wright, 1999, Chapter 2):

$$\boldsymbol{B}_{k+1} = \boldsymbol{B}_k - \frac{\boldsymbol{B}_k \boldsymbol{s}_k \boldsymbol{s}_k^\top \boldsymbol{B}_k}{\boldsymbol{s}_k^\top \boldsymbol{B}_k \boldsymbol{s}_k} + \frac{\boldsymbol{y}_k \boldsymbol{y}_k^\top}{\boldsymbol{y}_k^\top \boldsymbol{s}_k}, \tag{2.35}$$

$$\boldsymbol{s}_k = \boldsymbol{\theta}_{k+1} - \boldsymbol{\theta}_k, \tag{2.36}$$

$$\boldsymbol{y}_k = \boldsymbol{\nabla} J_{k+1} - \boldsymbol{\nabla} J_k, \tag{2.37}$$

where $\boldsymbol{B}_k$ is the Hessian approximation at optimisation iteration $k$. If a good approximation of the Hessian is used then a step length $\alpha$ of 1 of often sufficient for satisfying the Wolfe conditions.

# Part II

# Hydrodynamics

# 3 Introduction to modelling the flow in the reactor

To model the flow in the reactor, we solve the partial-differential equations that describe the motion of a fluid. We use a version of the Navier–Stokes equations suitable for flows with low Mach numbers. We also describe three other fluid models. For each model, three conservation equations are solved, one for each of the fluid mass, momentum and energy. The features of the flows are:

- the Mach number is low, which means the compressibility of the fluid can be neglected,
- the Reynolds number is low, which means the flow can be assumed to be laminar with no turbulence,
- there are high temperature differences, which requires a model that can accurately model changes in fluid density due to temperature,
- there is a possibility of density variations due to composition, because the reactor may mix of hydrogen and nitrogen.

Using these features, we evaluate four different approaches to fluid modelling.

## 3.1 The uniform density Navier–Stokes model

The uniform density Navier–Stokes model is the most simple of the four models, and describes the behaviour of an incompressible fluid with uniform density.

For this model, the energy equation cannot influence the mass and momentum equations, which means the energy equation can be solved separately, after the mass and momentum

equations have been solved:

$$\boldsymbol{\nabla} \cdot \boldsymbol{u} = 0, \tag{3.1}$$

$$\rho \left( \frac{\partial \boldsymbol{u}}{\partial t} + (\boldsymbol{u} \cdot \boldsymbol{\nabla}) \boldsymbol{u} \right) = -\boldsymbol{\nabla} p + \mu \boldsymbol{\nabla} \cdot \left( \boldsymbol{\nabla} \boldsymbol{u} + (\boldsymbol{\nabla} \boldsymbol{u})^{\top} \right) + \rho \boldsymbol{g}, \tag{3.2}$$

$$\rho c_p \left( \frac{\partial T}{\partial t} + \boldsymbol{u} \cdot \boldsymbol{\nabla} T \right) = \boldsymbol{\nabla} \cdot (k \boldsymbol{\nabla} T), \tag{3.3}$$

where $\boldsymbol{u}$ is the fluid velocity, $\rho$ is the fluid density, $p$ is the fluid pressure, $\mu$ is the fluid viscosity, $\boldsymbol{g}$ is the acceleration due to gravity, $c_p$ is the specific heat capacity, $T$ is the fluid temperature (in an absolute scale, such as Kelvin), and $k$ is the fluid thermal conductivity. This model is useful when the fluid density is constant and the flow is laminar. It has the lowest computational cost of the models presented, and is preferred whenever the density can be assumed to be both constant and uniform.

## 3.2 The Boussinesq approximation model

The Boussinesq approximation extends the uniform density Navier–Stokes equations by modelling the buoyancy of the fluid as a force proportional to the temperature difference from a baseline temperature $T_0$. This extension allows the model to describe fluid motion due to temperature-dependent buoyancy, while still assuming uniform density for the inertial terms:

$$\boldsymbol{\nabla} \cdot \boldsymbol{u} = 0, \tag{3.4}$$

$$\rho \left( \frac{\partial \boldsymbol{u}}{\partial t} + (\boldsymbol{u} \cdot \boldsymbol{\nabla}) \boldsymbol{u} \right) = -\boldsymbol{\nabla} p + \mu \boldsymbol{\nabla} \cdot \left( \boldsymbol{\nabla} \boldsymbol{u} + (\boldsymbol{\nabla} \boldsymbol{u})^{\top} \right) + \alpha \rho (T - T_0) \boldsymbol{g}, \tag{3.5}$$

$$\rho c_p \left( \frac{\partial T}{\partial t} + \boldsymbol{u} \cdot \boldsymbol{\nabla} T \right) = \boldsymbol{\nabla} \cdot (k \boldsymbol{\nabla} T), \tag{3.6}$$

where $\alpha$ is the coefficient of thermal expansion, and $T_0$ is the baseline temperature, and the other symbols are the same as above. This model is useful when buoyancy cannot be neglected but the temperature differences are small, and the resulting density variations are small.

## 3.3 The fully compressible Navier–Stokes model

In the fully compressible Navier–Stokes model, the fluid density is a function of pressure and temperature. This means the fluid model can simulate sound waves. However, this also means the equations become badly conditioned at low Mach numbers (Hinch, 2020). The full equations are:

$$\frac{\partial \rho}{\partial t} + \boldsymbol{\nabla} \cdot (\rho \boldsymbol{u}) = 0, \tag{3.7}$$

$$\frac{\partial \rho \boldsymbol{u}}{\partial t} + \boldsymbol{\nabla} \cdot (\rho \boldsymbol{u}\boldsymbol{u}) = -\boldsymbol{\nabla} p + \mu \boldsymbol{\nabla} \cdot \boldsymbol{\tau} + \rho \boldsymbol{g}, \tag{3.8}$$

$$\frac{\partial \rho e}{\partial t} + \boldsymbol{\nabla} \cdot (\rho \boldsymbol{u} e) = -\boldsymbol{\nabla} \cdot (\boldsymbol{u} p) + \boldsymbol{\nabla} \cdot (\boldsymbol{u} \tau) + \boldsymbol{\nabla} \cdot (k \boldsymbol{\nabla} T) - \rho \dot{w}, \tag{3.9}$$

$$p = \rho R T, \tag{3.10}$$

$$\boldsymbol{\tau} \equiv \boldsymbol{\nabla} \boldsymbol{u} + (\boldsymbol{\nabla} \boldsymbol{u})^{\top} - \tfrac{2}{3} (\boldsymbol{\nabla} \cdot \boldsymbol{u}) \boldsymbol{I}, \tag{3.11}$$

$$e \equiv c_p T + \tfrac{1}{2} \boldsymbol{u} \cdot \boldsymbol{u}, \tag{3.12}$$

where $\tau$ is the fluid stress tensor, $e$ is the fluid energy, $\dot{w}$ is the rate of heat release per unit mass, $R$ is the universal gas constant, $\boldsymbol{I}$ is the identity tensor, and the other symbols are the same as above.

## 3.4 The Low Mach-number model

In the low Mach number limit ($\mathrm{Ma} \ll 1$) of the fully compressible Navier–Stokes equations, the hydrodynamic pressure, $p$, and the thermodynamic pressure, $p_{\mathrm{th}} = \rho R T$ can be decoupled, eliminating acoustic waves from the equations while keeping density variations due to temperature (McMurtry et al., 1986). This model converges to a solution faster than the fully compressible Navier–Stokes model, because acoustic waves do not exist in this model, so a Poisson solver for the pressure $p$ can be used. The low Mach-

number (LMN) model obeys:

$$\frac{\partial \rho}{\partial t} + \boldsymbol{\nabla} \cdot (\rho \boldsymbol{u}) = 0, \tag{3.13}$$

$$\frac{\partial \rho \boldsymbol{u}}{\partial t} + \boldsymbol{\nabla} \cdot (\rho \boldsymbol{u}\boldsymbol{u}) = -\boldsymbol{\nabla} p + \mu \boldsymbol{\nabla} \cdot \boldsymbol{\tau} + \rho \boldsymbol{g}, \tag{3.14}$$

$$\frac{\partial \rho c_p T}{\partial t} + \boldsymbol{\nabla} \cdot (\rho c_p \boldsymbol{u} T) = \boldsymbol{\nabla} \cdot (k \boldsymbol{\nabla} T) + \rho \dot{w}, \tag{3.15}$$

$$p_{\mathrm{th}} = \rho R T, \tag{3.16}$$

$$\boldsymbol{\tau} \equiv \boldsymbol{\nabla} \boldsymbol{u} + (\boldsymbol{\nabla} \boldsymbol{u})^{\top} - \tfrac{2}{3} (\boldsymbol{\nabla} \cdot \boldsymbol{u}) \boldsymbol{I}, \tag{3.17}$$

$$\boldsymbol{\nabla} p_{\mathrm{th}} = \boldsymbol{0}, \tag{3.18}$$

where $p_{\mathrm{th}}$ is the thermodynamic pressure and the other symbols are the same as above.

We use this model to solve the flow in the reactor, because it handles the large temperature variations without the added complexity, and accompanying increased convergence time, of acoustic waves. The Reynolds number of the flow is of order 100, therefore the flow remains laminar and we do not need to derive Reynolds-averaged versions of these equations to handle turbulence.

# 4 Investigating the reactor gas valve

First the reactor outlet and the gas valve is investigated. The gas valve removes the reactor gases (consisting mainly of hydrogen), and replaces them with nitrogen. The aim is to bring the concentration of hydrogen at the exit to below 4 %.

Figure 4.1 shows the diagram and a photo of the gas valve. The valve consists of four 30 mm sections, each with three 5 mm diameter nozzles. The wide metal ring, pictured at the top of both figures, is attached to the outlet of the reactor, while the exit, at the bottom of both figures, is open to the laboratory environment. The nozzles in the first (top) and third sections remove gas. The other nozzles, in the second and fourth (bottom) sections, inject nitrogen. Between each section there is a metal baffle which restricts the flow.

(a) Blueprint of the gas valve.

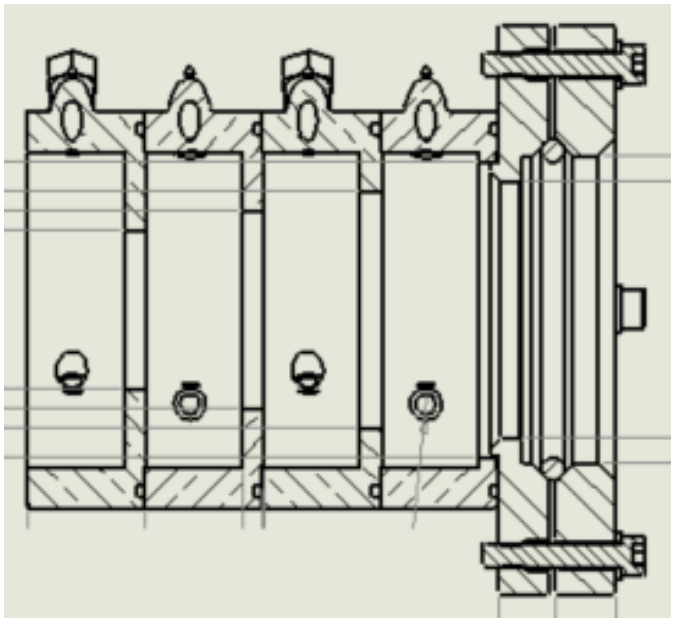

(b) Photo of the gas valve.

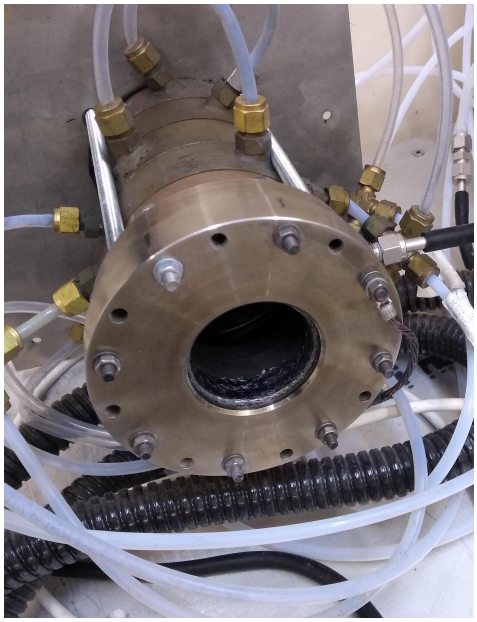

Figure 4.1 A diagram (*a*) and photo (*b*) of the gas valve attached to the reactor outlet. During operation it is fed with a total of 14 L min$^{-1}$ of nitrogen. Half of the nozzle sections are injecting nitrogen into the gas valve, the other half are extracting gas. The carbon nanotube product is extracted through the centre of the gas valve and rolled on a collection spool. Photo credit is for (*a*) James Elliot and for (*b*) Fiona Smail.

Figure 4.2 shows radial slices of the gas valve model. The dash-dotted line on the bottom of each diagram represents the centreline. The solid lines show the location of the walls. The inlet diameter is narrower than the gas valve diameter in order to model a narrow exhaust pipe attached to the end of the reactor. The reactor fluid enters on the left of the model, and exits through the exhaust on the right. The geometry of the laboratory gas valve is three-dimensional. We use an axisymmetric model, in order to reduce the numerical complexity and to speed up the computations required to model the fluid. This means we cannot simulate the jets of the three nozzles in each section. Instead we model the nozzles by a uniform radial flow that has the same flow rate as the three nozzles combined. This radial flow enters through the radial inlets and leaves through the radial outlets shown in the diagrams.

We look at the three different gas valve configurations shown in figure 4.2. For the 2-section configuration, the radial outlet flow (1a) and the radial inlet flow (1b) have the same flowrate, $Q_F$. For the 3-section configuration, the radial inlet 3 flow has an inlet flowrate equal to the sum of both radial 1 and 2 outlet flows. For the 4-section configuration the first two radial flows (1a and 1b) use the same flow rate $Q_{F1}$, while the second two radial flows (2a and 2b) use the same flow rate $Q_{F2}$. The radial flowrates are chosen to have net zero flowrate, so that no additional flow leaves through the exhaust. The blue numbers on the diagrams show the quantities that are fixed for the investigations in section 4.1.

The third configuration, figure 4.2c, corresponds to the gas valve used in the laboratory. The other two configurations are for comparison, and to investigate whether low concentrations of reactor gases, comparable to the 4-section configuration, can be achieved with a smaller gas valve.

The dimensions of the model are shown in figure 4.3. The radius of the inlet section is 25 mm. The radius of the radial flow sections and the outlet is 50 mm. The baffle hole radius is measured from the centreline to the tip of the baffle, and varies from 5 to 50 mm. The inlet section is 100 mm long to allow the inlet flow to develop fully before reaching the radial flow sections. We also add a 150 mm long outlet section in the model, in order to prevent the outlet conditions from affecting the flow in the radial flow sections.

The results of the main investigation are discussed in section 4.1. We model the concentration of the reactor gases in the gas valve for the three different configurations, shown

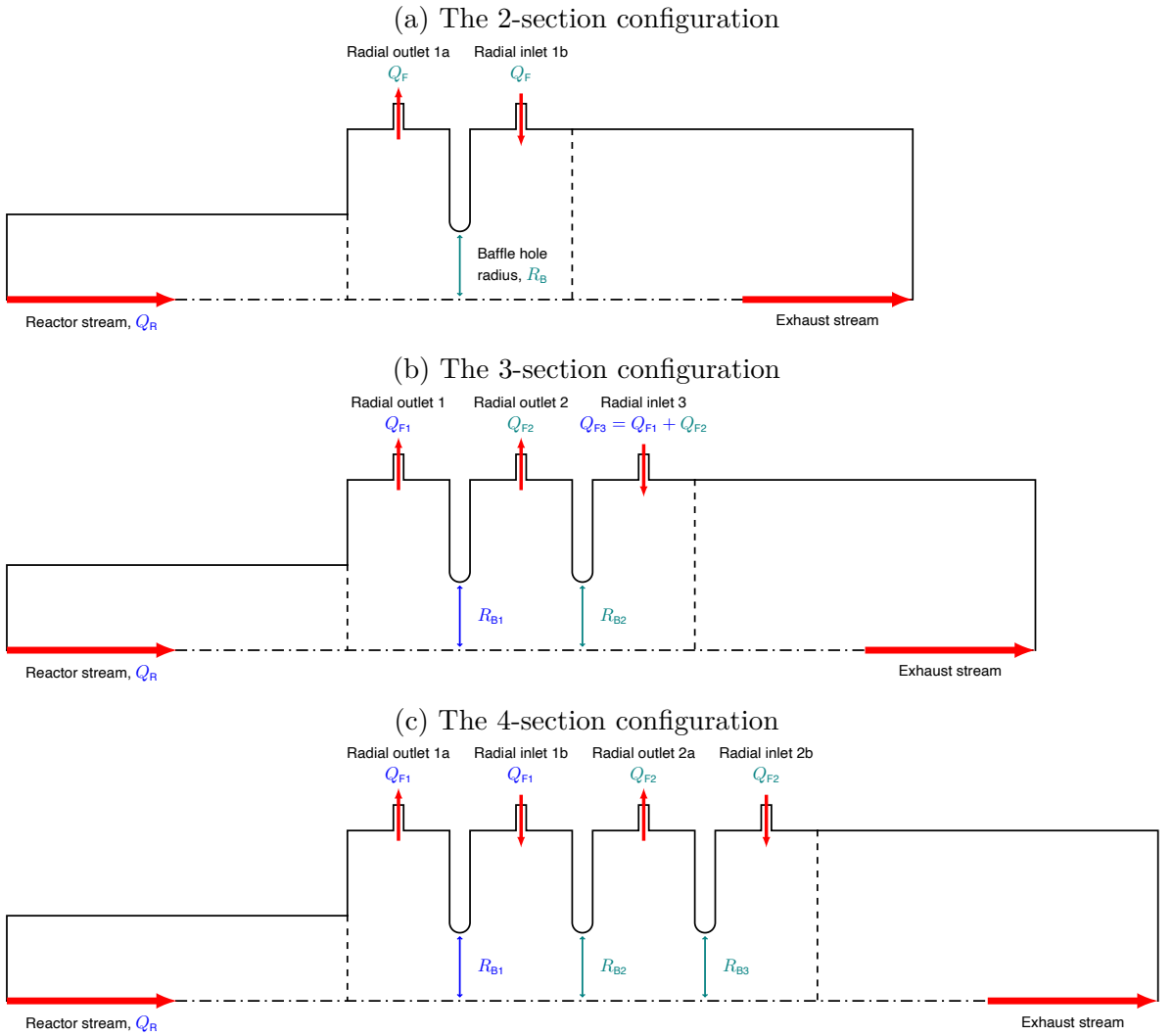


Figure 4.2 The three gas valve configurations investigated. The inlet section, outlet section, and all radial flow sections are identical between the configurations. Only a radial slice of the gas valve is shown, with the centreline on the bottom of each configuration.

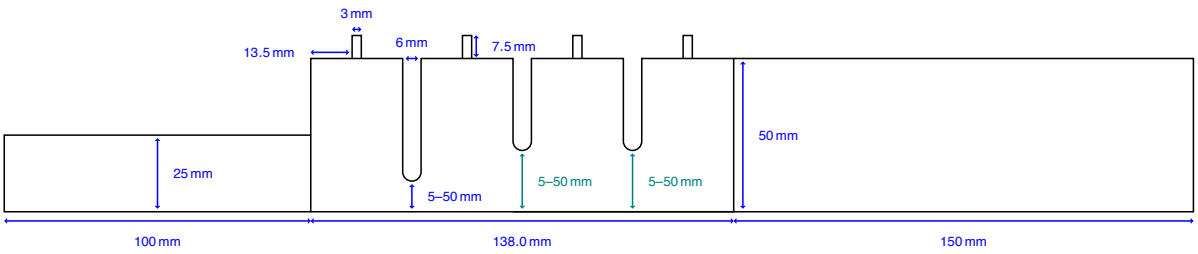


Figure 4.3 The dimensions of the gas valve, for the 4-section configuration. The three baffle hole radii vary between 5 mm and 50 mm. All other dimensions are constant during the investigation.

in figure 4.2. We vary the flowrates through the radial inlets and outlets, and the baffle hole radii. As the design space is relatively small, we search the design space without using a gradient-based optimisation process. To investigate the effect the nozzles have on the flow in the gas valve, we also perform a three-dimensional investigation, described in section 4.2.

## 4.1 Dilution and recovery of hydrogen

The first objective of this investigation is to find the gas valve design that produces safe conditions at the exhaust outlet. Lower concentrations of reactor gases at the outlet are preferable. The second objective is to recover high-concentration reactor gases that can be reused in the reactor. A higher concentration of reactor gases at one of the radial outlets in the gas valve is preferable. The third objective is to minimise the amount of nitrogen used in the gas valve. Reducing the total flowrate of nitrogen will reduce the running cost of the process.

To evaluate the first and second objectives we simulate the concentration of reactor gases in the reactor. We model the concentration of the reactor gases with a scalar that convects and diffuses with the flow. The reactor inlet flow enters with a scalar value of 1, representing pure reactor gases, while the radial inlet flows enter with a scalar value of 0, representing pure nitrogen. We evaluate the first objective by comparing the average scalar value at the exhaust outlet. Lower scalar values are preferable. The second objective is evaluated by the average scalar value at the first radial outlet. Here, higher scalar values are preferable.

The reactor flowrate is $1.4\,\mathrm{L\,min^{-1}}$ for all simulation runs. The flowrates through the radial inlets and outlets are varied between 0–$7\,\mathrm{L\,min^{-1}}$ in increments of $1.4\,\mathrm{L\,min^{-1}}$. On the figures below, the radial flowrate, $Q_F$, is given as a number between 0 and 5, after being nondimensionalised by the reactor flowrate, $Q_R$.

The baffle hole radii are varied between 5–50 mm in increments of 5 mm. On the figures below, the baffle hole radius, $R_B$, is given as a number between 0 and 1, after being nondimensionalised by the 50 mm gas valve radius, $R_E$.

### 4.1.1 The 2-section configuration

Figure 4.4 shows how the concentration of reactor gases at the exhaust ($a$), and the radial outlet ($b$) varies with the radial flowrate and baffle hole radius, for the 2-section configuration. The purple colour shows the parameter space where the concentration of the reactor gases is low, and the majority of the fluid is nitrogen. The orange colour shows the parameter space where the concentration of the reactor gases is high. The dotted lines at the 0.4 baffle hole radius ratio mark show the operating points further explored in figure 4.5 below. The solid 4 % contour line in ($a$) shows the limit of safe operation. Using a gas valve with a smaller baffle hole radius or a radial flowrate higher than points on that line will ensure the exhaust fluid is safe.

An optimal design using the 2-section configuration, which minimises the concentration of hydrogen at the exhaust while maximising the concentration of reactor gases at the radial outlet, has a 5 mm baffle hole radius ($R_B/R_E = 0.1$), and a radial flowrate of at least 1.7 L min$^{-1}$ ($Q_F/Q_R = 1.2$). This keeps the reactor gas concentration at the exhaust below 4 % (objective 1), while recovering reactor gases at the radial outlet of approximately 60 % purity (objective 2). Additionally, this design minimises the usage of nitrogen gas (objective 3).

Figure 4.5 explores how the radial flowrate affects the streamlines in the gas valve, and visualises the resulting change in reactor gas concentration. The baffle hole radius is fixed at 20 mm ($R_B/R_E = 0.4$). These operation points correspond to the dotted line in figure 4.4. The background colour of the gas valve corresponds to the reactor gas concentration. The white lines are streamlines that show the path the fluid takes through the gas valve. Only the lines that pass through the baffle hole are shown. When the radial flow is zero the inlet flow from the reactor passes directly to the exhaust outlet. In this case, the reduction in reactor gas concentration is due to diffusion through the radial inlet. At a radial flowrate ratio of $Q_F/Q_R = 1$, ($b$), a small portion of the inlet reactor flow passes directly to the exhaust outlet, while the majority of the reactor flow is captured and extracted by the radial outlet. Nitrogen entering from the radial inlet replaces this captured fluid, reducing the reactor gas concentration at the exhaust outlet. At higher radial flowrate ratios, $Q_F/Q_R = 2$ and above, ($c$–$f$), the flow from the reactor is fully captured and extracted by the radial outlet. Increasing the radial flowrate further reduces the reactor gas concentration in the exhaust outlet, making the configuration safer to operate (objective 1). Increasing the flowrates also reduces the concentration of reactor gases at the radial outlet, reducing the viability of reusing the reactor gas

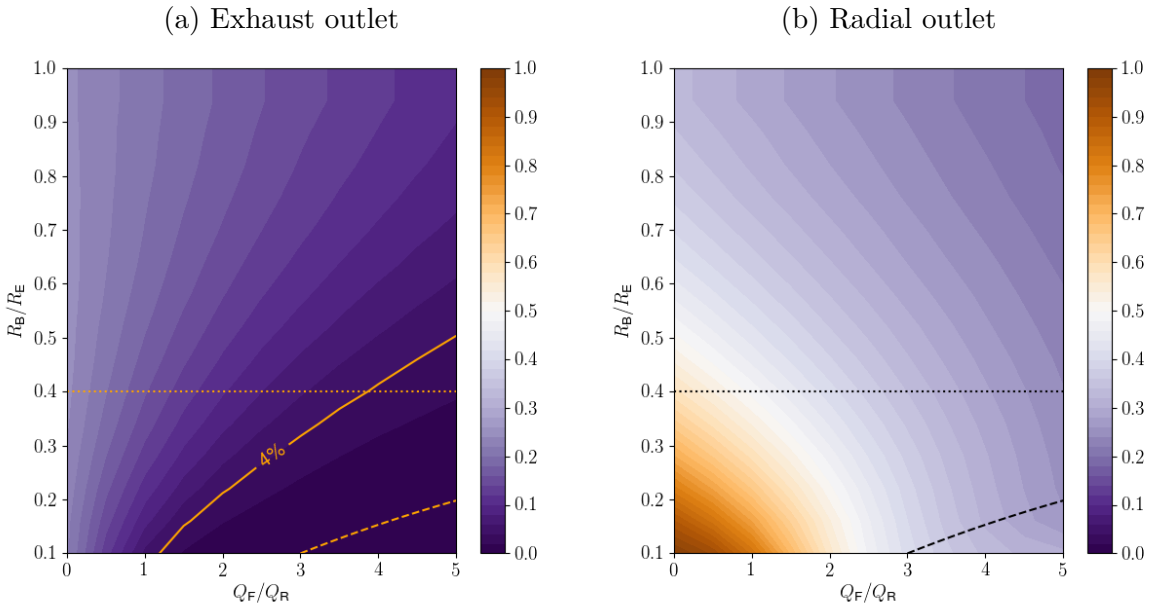


Figure 4.4 Concentration of reactor gases at the exhaust outlet ($a$) and radial outlet ($b$), for different baffle hole radii and radial flowrates, for the 2-section geometry. The dashed line in the lower right of each figure shows the region where the radial inlet flow enters the reactor inlet region, which is not desirable as it may disrupt the process upstream in the reactor. The solid line in ($a$) shows the 4 % hydrogen concentration contour. Regions below and to the right of this line are within safe levels of hydrogen gas at the exhaust outlet. The dotted lines show the operating conditions explored further in figure 4.5.

(objective 2). At the highest radial flowrate ratio investigated, $Q_F/Q_R = 5$, $(f)$, the flow from the radial inlet reaches the reactor inlet section. Usually pure hydrogen is the carrier gas, and the choice of carrier gas affects the optimal concentrations of the reactants (Weller et al., 2019). Reverse flow of nitrogen into the reactor is unwanted as it can disrupt the efficiency of the reactor.

### 4.1.2 The 3-section configuration

Adding an additional section to the gas valve enables a better trade-off between reducing the reactor gas concentration at the exhaust, and increasing the concentration at the radial outlet for reactor gas recovery. For the 3-section investigation we fix the flowrate through the first radial outlet to $1.4\,\mathrm{L\,min^{-1}}$ ($Q_{F1}/Q_R = 1$), and the baffle hole radius to 5 mm ($R_{B1}/R_E = 0.1$). Figure 4.6 shows the reactor fluid concentration contours at the exhaust outlet, $(a)$, and the first radial outlet, $(b)$, as the flowrate and baffle hole radius varies. The flowrate through the second radial outlet, $Q_{F2}$, is varied between 0–$7\,\mathrm{L\,min^{-1}}$ in intervals of $1.4\,\mathrm{L\,min^{-1}}$, and the flowrate through the radial inlet is set to the sum of the flowrates through flush outlets 1 and 2, $Q_{F3} = Q_{F1} + Q_{F2}$. Figure 4.6, the flowrate is normalised by the $1.4\,\mathrm{L\,min^{-1}}$ reactor flowrate, $Q_R$. The baffle hole radius of the second baffle, $R_{B2}$, is varied between 5–50 mm, normalised by the gas valve radius $R_E$ in the figure.

With the 3-section configurations, a safe reactor gas concentration at the exhaust outlet can be achieved with less nitrogen, compared to the 2-section configuration. With a narrow 5 mm second baffle hole radius, $R_{B2}$, a safe concentration is achieved without using radial outlet 2. In this case only the $1.4\,\mathrm{L\,min^{-1}}$ flowrate through radial outlet 1 is necessary, which is $0.3\,\mathrm{L\,min^{-1}}$ lower than the flowrate necessary to make the 2-section configuration safe. Lower flowrates through radial outlet 2, and a narrower baffle hole 2 also increases the concentration of the reactor gas recovered at radial outlet 1, up to 85 % concentrated, when using the conditions described above.

### 4.1.3 The 4-section configuration

The 4-section configuration uses two pairs of radial inlets and outlets. This allows us to set the flowrate and baffle hole radii in the first two sections to maximise the recovery of reactor gases, while setting the flowrate and baffle hole radius of the last two sections to ensure the concentration of reactor gases at the outlet is at a safe level. We set the flowrate through the first radial inlet and outlet to $1.4\,\mathrm{L\,min^{-1}}$ ($Q_{F1}/Q_R = 1$) to

(a) Flowrate ratio $Q_F/Q_R = 0$

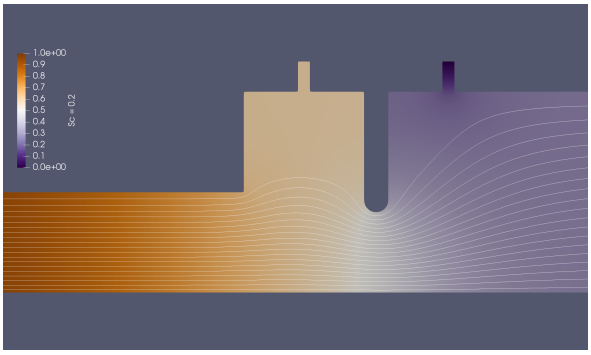


(b) Radial flowrate ratio $Q_F/Q_R = 1$

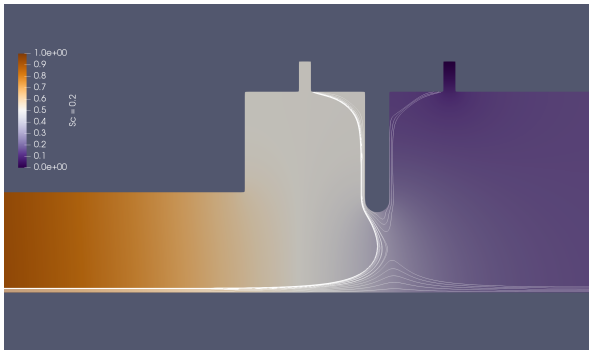


(c) Radial flowrate ratio $Q_F/Q_R = 2$

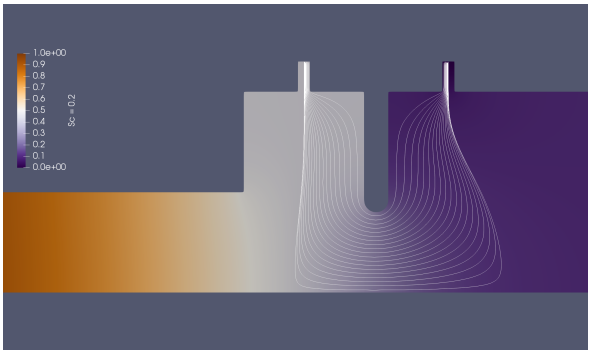


(d) Radial flowrate ratio $Q_F/Q_R = 3$

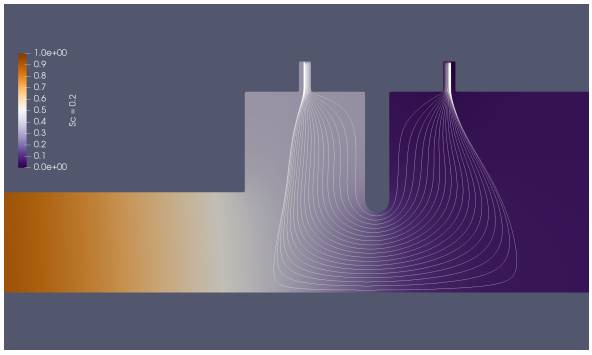


(e) Radial flowrate ratio $Q_F/Q_R = 4$

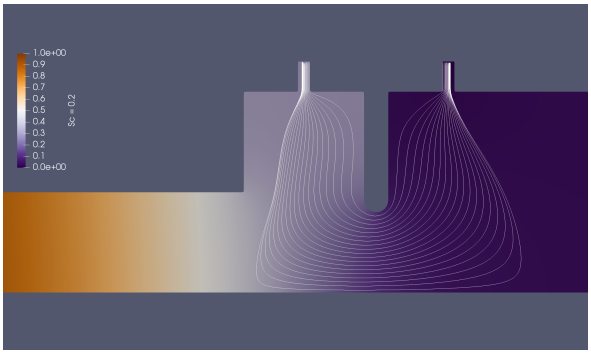


(f) Radial flowrate ratio $Q_F/Q_R = 5$

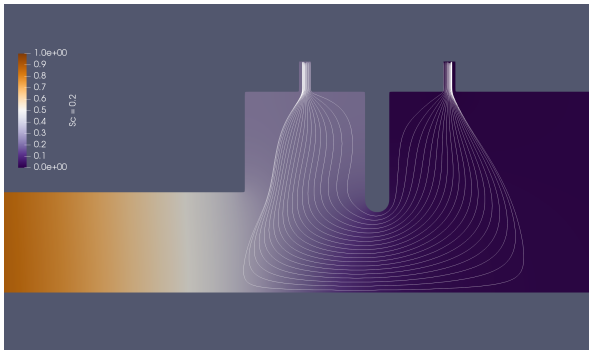


Figure 4.5 Streamlines across the baffle in the 2-section geometry. The coloured background shows the concentration of reactor gases in the flow. Orange colours correspond to higher concentrations of reactor gases, while purple colours correspond to lower concentrations. The baffle hole radius is 20 mm ($R_B/R_E = 0.4$). As the radial flowrate increases the nitrogen from the radial inlet is pushed further upstream, decreasing the concentration of reactor gases at the radial and exhaust outlets.

(a) Exhaust outlet

(b) Radial outlet 1

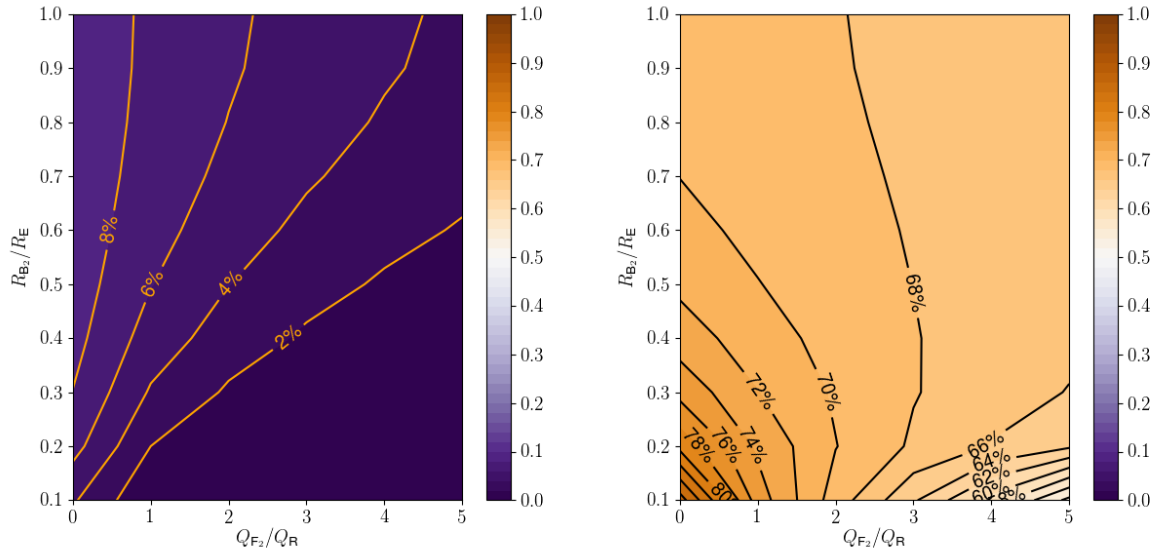


Figure 4.6 Reactor gas concentration contours for a 3-section configuration. The background colour shows the concentration of the reactor fluid. Orange corresponds to high concentrations of reactor fluid, while purple corresponds to low concentrations of reactor fluid.

extract all the fluid entering from the reactor. The first baffle hole radius is set to 10 mm ($R_{B1}/R_E = 0.2$) to reduce the diffusion of nitrogen into the reactor gas, while also not overly constricting the clearance for the aerogel to pass through.

Figure 4.7 shows the concentration contours at the exhaust outlet, for six different values of the second baffle hole radius, varying between 0.1–1 for subfigures (*a*–*f*). The third baffle hole radius ratio ($R_{B3}/R_E$) is shown on the vertical axis. The second radial flowrate ratio, $Q_{F2}$, is shown on the horizontal axis. The solid black lines show the contours of 1–4 % reactor gas concentration at the exhaust outlet. The concentration of reactor gases at the first radial outlet is not examined in this investigation. The concentration does not significantly deviate from the 60 % predicted by the 2-section configuration using the first radial pair flowrate and first baffle hole radius described above.

Increasing the flowrate in the second radial outlet and inlet always reduces the concentration of the reactor fluid at the exhaust outlet. A stronger decrease of the reactor fluid concentration at the exhaust outlet is seen when the second baffle hole radius is smaller. When the second baffle hole radius is at or below 20 mm ($R_{B2}/R_E \leq 0.4$, (*d*–*f*)) a concentration of reactor fluid at the outlet of less than 1 % can be achieved. This very low reactor gas concentration is possible with a radial flowrate through the second radial inlet and outlet of 1 L min$^{-1}$, 1.5 L min$^{-1}$, or 3 L min$^{-1}$, when the second baffle hole radius is 5 mm, 10 mm, or 20 mm respectively.

At low values of the second baffle hole radius ($R_{B2}/R_E \leq 0.2$, (*e*) and (*f*)) further restrictions of the flow, with lower third baffle hole radius ($R_{B3}$), does not affect the concentration of reactor fluid at the outlet. Only with a more open second baffle hole ($R_{B2}/R_E \geq 0.4$, (*a*–*d*)) does the third baffle ratio affect the concentration of reactor gases at the outlet. Only when the second baffle hole radius is at or above 40 mm is it possible to have a concentration of more than 4 % reactor fluid at the outlet, when there is no flow through flush outlet 2a and inlet 2b.

The efficiency of a narrow first baffle hole radius is demonstrated in figure 4.8, which shows example flows from the 4-section investigation. Both the left (*a*) and right (*b*) figure show the streamlines. The first baffle hole radius is set at 10 mm, and the first radial flowrate ($Q_{F1}$) is 1.4 L min$^{-1}$, as for the 4-section investigation. For these figures the second and third baffle hole radii are both 20 mm. The second radial flowrate ($Q_{F2}$) is 1.4 L min$^{-1}$ for the left figure (*a*), and 5 L min$^{-1}$ for the right figure (*b*). The

(a) Second baffle hole radius ratio of 1.0

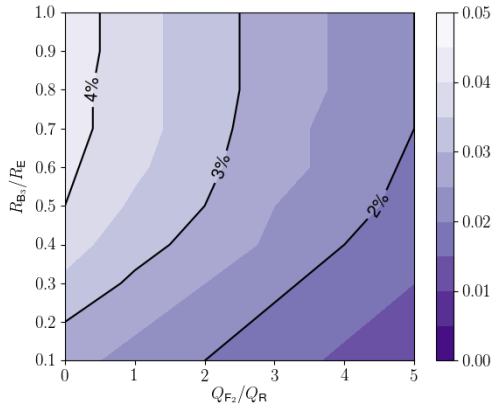


(b) Second baffle hole radius ratio of 0.8

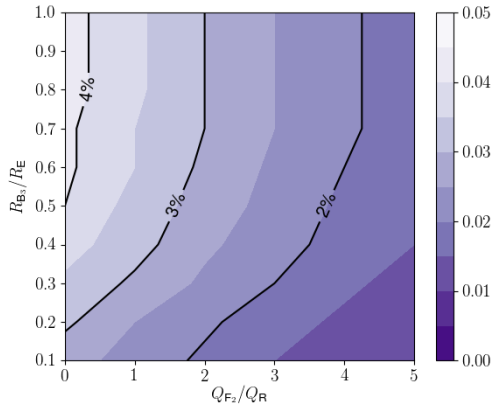


(c) Second baffle hole radius ratio of 0.6

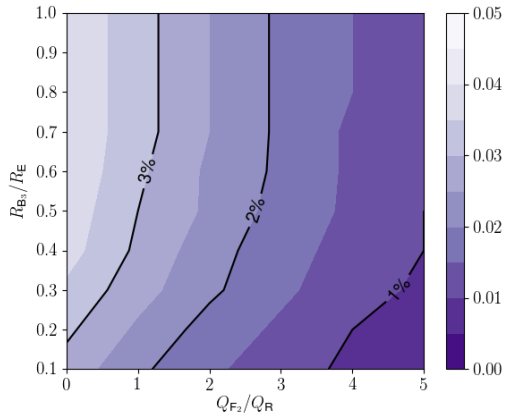


(d) Second baffle hole radius ratio of 0.4

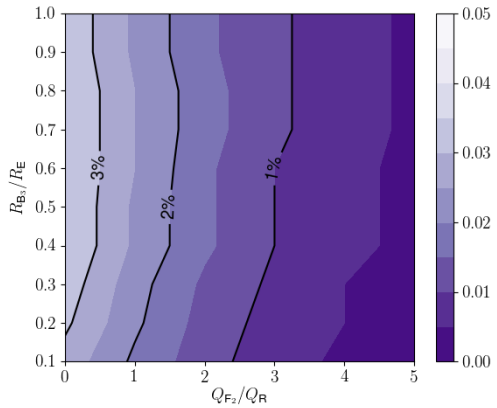


(e) Second baffle hole radius ratio of 0.2

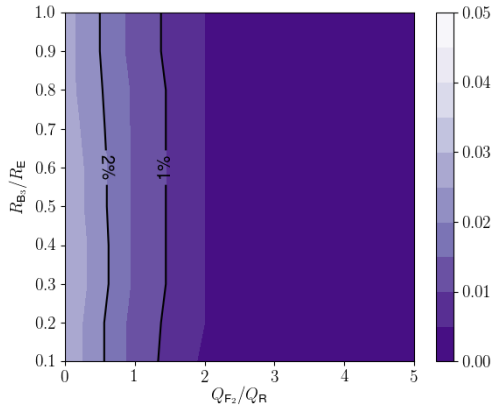


(f) Second baffle hole radius ratio of 0.1

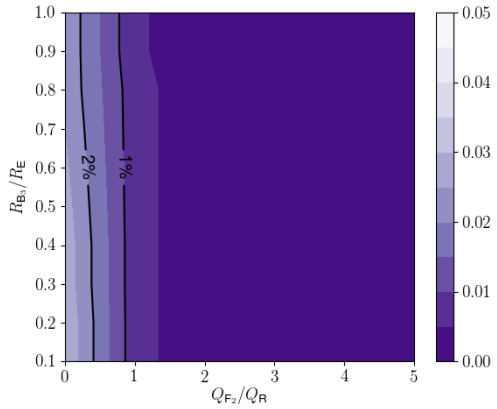


Figure 4.7 Reactor gas concentration contours for the 4-section configuration. Each figure shows the influence of the second radial flowrate and the third baffle hole radius on the concentration of reactor gases at the exhaust outlet. Each figure corresponds to a specific second baffle hole radius. The contours show the concentration at the exhaust outlet.

contours show the concentration of reactor gases, with the orange region signifying high concentrations of reactor gases, while the purple region signifies low concentrations. Because the flowrate through the first radial outlet is the same as the inlet flowrate from the reactor, the majority of reactor fluid is recovered, and can be reused. The narrow clearance under the first baffle hole reduces the cross-sectional area, reducing diffusion of nitrogen from the first radial inlet into the extracted reactor gases. Increasing the second radial flowrate from $1.4\,\mathrm{L\,min^{-1}}$ ($a$) to $5\,\mathrm{L\,min^{-1}}$ ($b$) does not affect the streamlines in the first section, where the reactor gas is extracted.

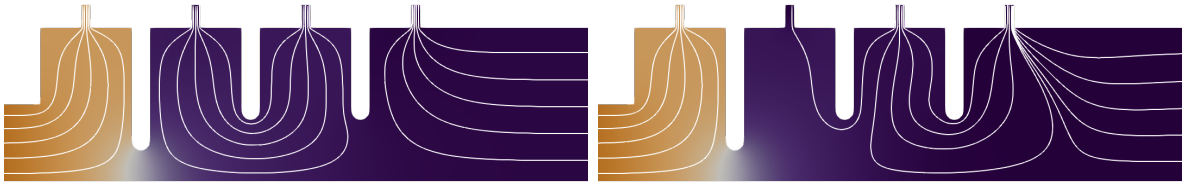

(a) Second radial flowrate of $1.4\,\mathrm{L\,min^{-1}}$ (b) Second radial flowrate of $7\,\mathrm{L\,min^{-1}}$

Figure 4.8 Streamlines plotted on a radial slice of a 4-section gas valve. The first baffle hole radius is 10 mm, the second and third baffle hole radii are 20 mm. The first radial flowrate ($Q_{F1}$) is $1.4\,\mathrm{L\,min^{-1}}$. The second radial flowrate ($Q_{F2}$) is $1.4\,\mathrm{L\,min^{-1}}$ on the left ($a$), and $7\,\mathrm{L\,min^{-1}}$ on the right ($b$). The colour scale is as for figure 4.6, with the orange colour corresponding to high concentration of reactor gases, and the purple colour corresponding to low concentration of reactor gases.

## 4.2 Three-dimensional investigation

Each section in the laboratory gas valve has three angled nozzles for inlet and outlet flow, in contrast to the radial flow we have used to model the nozzles in the axisymmetric investigation. These nozzles break the azimuthal symmetry of the flow and impose some azimuthal velocity (swirl). To understand how this symmetry breaking and swirl affect the reactor flow, we solve a three-dimensional model of the 2-section gas valve. We qualitatively compare the three-dimensional results with the results of the axisymmetric model. For model simplicity we do not include a baffle in the three-dimensional model. Figure 4.9 shows a three-dimensional view of the flow in the centre of the gas valve. The faint grey lines show the boundaries of the model geometry. The blue lines show the streamlines in the gas valve. The streamlines originate from the reactor inlet. The majority of the streamlines exit through the nozzles in the first section. A smaller number of streamlines are seen to exit towards the exhaust outlet of the gas valve to the

left on the figure. The nozzles are approximated by a Fourier series on the boundary condition in the first section, so a smaller number of streamlines exit through the region between the three nozzles. The green colours of the streamline at the outlet nozzles show the higher velocity of the flow as the fluid is extracted. The same high velocity is found in the inlet flow in the second section.

The angled inlet and outlet nozzles sustain a swirling vortex in the centre of the flow by the gas valve sections. This swirling flow will trap the aerogel as it leaves from the reactor and cause it to precess. This precession is unwanted as the aerogel may attach if it touches the wall of the gas valve. If the aerogel attaches to the wall the gas valve needs to be cleaned before the aerogel production process can resume. Because of the risk of wall-attachment, the angled nozzles negatively impact the design of the aerogel, requiring larger baffle hole radii to avoid wall-attachment. A non-swirling flow, where the aerogel can be contained at the centreline, enables a more efficient gas valve design, as the risk of wall-attachment is lower.

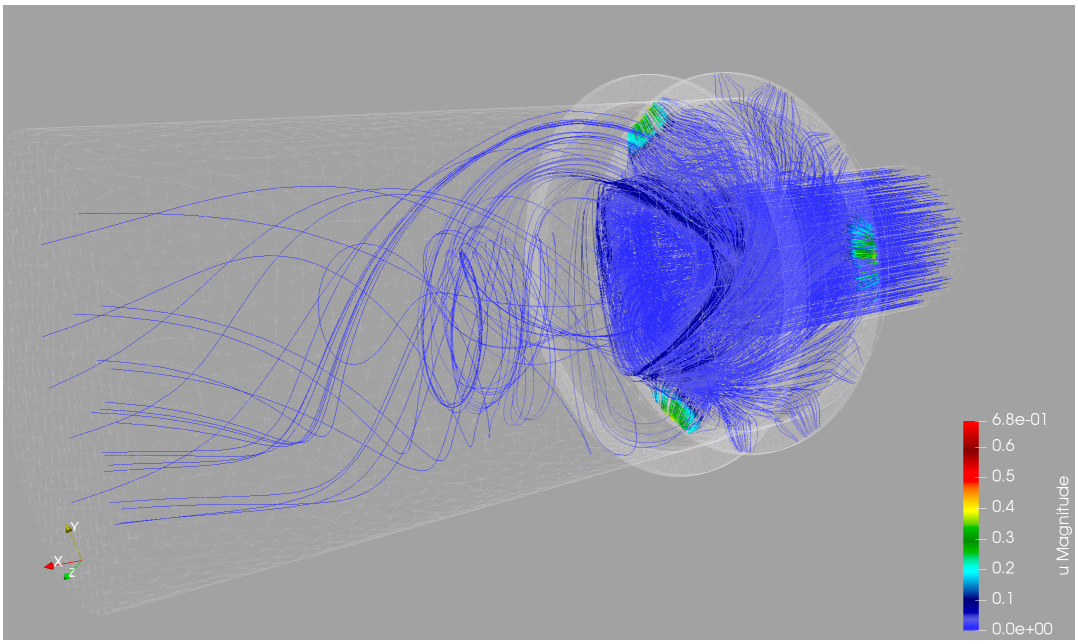


Figure 4.9 Streamlines in the three-dimensional gas valve model. The faint white lines show the boundaries of the model geometry. The mainly blue lines show the streamlines of the gas valve flow originating from the reactor inlet, on the right of the figure. The colour of streamlines correspond to the velocity magnitude, in $\mathrm{m\,s^{-1}}$.

## 4.3 Recommendations for future designs

Based of our investigation we recommend the following design points for the gas valve.

- We recommend using small baffle hole radii. Using a small radius for the first baffle hole gives the largest reduction in reactor gas concentration at the exhaust outlet, while also increasing the concentration of reactor gases at the first radial outlet. The reduced cross sectional area where the flow can pass reduces the cross-diffusion of reactor gases and nitrogen, resulting in higher concentration of reactor gases that can be recovered in the early sections, and lower concentration of reactor gases at the exhaust outlet. This reduced concentration in the later sections allows similar low outlet concentrations to be achieved with lower radial flowrates in the second radial flow $Q_{F2}$.
- We recommend that any nozzles point towards the centre, instead of being angled. Radially aligned nozzles will inhibit vortex formation in the gas valve. The vortex increases the risk that the aerogel attaches to the gas valve walls. Preventing the vortex from forming will allow the baffle hole radii to be lower.
- We find that a 3-section geometry is sufficient for achieving both safe levels of reactor gases at the exhaust outlet, and high concentration of reactor gases at the first radial outlet, for reactor gas reuse. This allows the gas valve to be shorter, and means less nitrogen is required to operate the gas valve, as one fewer section is in use. One baffle fewer in the gas valve also reduces the risk of the aerogel attaching to the wall.

# 5 Modelling the aerogel in the gas valve

After modelling the base flow in the gas valve, the next step is to look at how the carbon nanotube aerogel affects this flow. We use a flow-structure interaction model to simulate how the aerogel structure is affected by the flow in the reactor, and the internal flow enclosed by the aerogel. To reduce the complexity of the fluid model we assume the buoyancy force is negligible compared with the momentum, pressure, and viscous forces. This allows us to both use a simpler flow model, and to model the flow as axisymmetric in a horizontal reactor. This is reasonable for a vertical reactor, but should be treated with care if a more detailed investigation of the aerogel behaviour in a horizontal reactor is performed. Additionally we extend the axisymmetric assumption to the gas valve structure and flow as well. We will qualitatively show that this is reasonable later on.

We do not know quantitatively the properties of the aerogel, so to produce a qualitative model we make some further assumptions, which simplifies how the aerogel is modelled. We know that the aerogel is thin and light, so we do not model its thickness and mass. Additionally we know that the aerogel is flexible, so we assume it has negligible bending rigidity. In the video of the aerogel as it exits the reactor captured by Hoecker et al. (2016, Video 1) the radius decreases as the aerogel is convected away from the reactor outlet. Based on this evidence we assume the radius of the aerogel is determined by a hoop stress balancing a pressure difference between the inside and outside region of the aerogel. We assume this hoop stress is proportional to the radius of the aerogel. Additionally we assume that the axial tension in the aerogel is small compared to the hoop tension. In order to reduce the complexity of the aerogel model we also assume the aerogel is impermeable. This means we do not have to account for gas seepage through the aerogel as it moves through the reactor.

Finally we assume that the aerogel is wound up flat on a drum, condensed and shrunk to zero diameter, or undergoes a similar process preventing the reactor gases from collecting inside the aerogel. This means there is net zero flux of reactor gases on at the downstream boundary of the aerogel.

The new layout of the gas valve with the aerogel is presented in figure 5.1. The gas valve configuration is similar to the 4-section configuration used in chapter 4, with the addition of the aerogel interface around the centreline. The inlet radius of the aerogel, $R_S$, and the aerogel extraction velocity, $U_S$ is fixed during the modelling. The approach for modelling the aerogel is presented below.

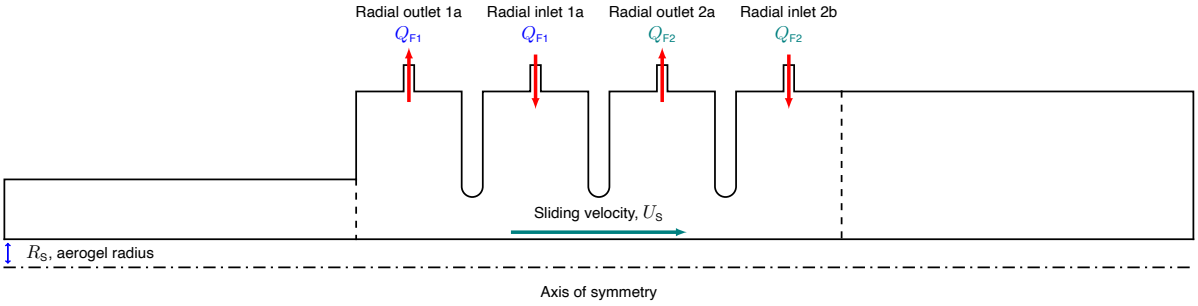


Figure 5.1 The 4-section gas valve configuration used to model the aerogel. The aerogel is manually extracted with a sliding velocity $U_S$ determined by the winding speed of the collector mechanism.

## 5.1 Introduction to fluid-structure interaction

In a fluid-structure interaction (FSI) problem, we solve both for the motion of the fluid, and the motion of a solid structure interacting with the fluid. In our case we solve for the steady-state position of the aerogel as it is extracted through the gas valve. The fluid flowing in the gas valve will change the shape of the aerogel as it is pulled through the gas valve.

There are two main approaches to solving a FSI problem. The first approach is the immersed boundary method, developed by Peskin (1972) to model the heart. (Mittal and Iaccarino (2005) also provides a good overview of the immersed boundary method.) In the immersed boundary method the boundary between fluid and structure is defined by a function that does not necessarily align with the mesh boundaries of the modelling grid. The force of the structure on the fluid is found by integrating the boundary-defining function over the modelling domain. As the structure moves, the function is updated to define the new location of the boundary. This approach is well suited for problems with elastic boundaries, such as the walls of the heart, or where the mesh grid is structured, or needs to be static due to numerical reasons, for example if a finite differences method is used for solving the partial differential equations of the flow model.

The second approach is the arbitrary Lagrange-Euler method (Donea et al. (2004); Sarrate et al. (2001) provide a good overview). In this method the boundary between the fluid and the solid is aligned with the edges of the modelling mesh. The force on the fluid can then be directly applied on the mesh nodes at the relevant edges. To update the position of the structure, all mesh points are shifted a small amount, slightly deforming the mesh. This approach works especially well with an unstructured mesh. An unstructured mesh can rearrange the internal mesh points at no great numerical cost, in order to restore any degradation of the mesh that builds up from the deformation of the mesh.

Both approaches work well with an iterative solution scheme, where a small displacement of the mesh is performed each iteration. For our simulations we use the arbitrary Lagrange-Euler method, as this works well with the unstructured mesh we use to find our solutions.

## 5.2 The aerogel structure model

The motion of the aerogel is modelled as an Euler beam, similarly to the way that Connell and Yue (2007); Shelley and Zhang (2011) model flapping flags and Alben et al. (2004) model a flexible structure in a flow. We model the motion of the aerogel similarly to Alben et al. (2004), where the position $\boldsymbol{x}$ of the aerogel interface obeys:

$$m_s \frac{\partial^2 \boldsymbol{x}}{\partial t^2} - (T_a \hat{\boldsymbol{s}})' + (E\kappa' \hat{\boldsymbol{n}})' - T_h \left(\boldsymbol{x} \cdot \hat{\boldsymbol{e}}_r\right) \hat{\boldsymbol{e}}_r = \boldsymbol{f}, \tag{5.1}$$

where $m_s$ is the mass per unit length, $T_a$ is the axial tension of the aerogel, $T_h$ is the hoop tension, $E$ is the bending rigidity (negligible), $\kappa$ is the curvature, $\hat{\boldsymbol{s}}$ is the unit vector in the tangential direction (relative to the aerogel), $\hat{\boldsymbol{n}}$ is the unit vector in the normal direction (relative to the aerogel), $\hat{\boldsymbol{e}}_r$ is the unit vector in the radial direction, and $\boldsymbol{f}$ is the force on the aerogel from the surrounding fluid. The prime $(\cdot)'$ denotes a derivative along the arc length of the aerogel.

Removing the negligible term and looking for a steady-state solution, in which the time derivatives are zero, leaves:

$$-(T_a \hat{\boldsymbol{s}})' - T_h \left(\boldsymbol{x} \cdot \hat{\boldsymbol{e}}_r\right) \hat{\boldsymbol{e}}_r = \boldsymbol{f}. \tag{5.2}$$

In the steady-state solution, the axial force is balanced by the axial tension $T_a$ component in the radial direction, and the radial force is balanced predominantly by the hoop tension $T_h$ multiplied by the radius of the aerogel $\boldsymbol{x} \cdot \hat{\boldsymbol{e}}_r$. We choose $T_h$ to be $1\,\mathrm{kN\,m^{-1}}$ in the absence of an experimental measurement.

The force on the aerogel, $\boldsymbol{f}$, is the resultant difference of the pressure and shear force on either side of the aerogel:

$$\boldsymbol{f} \equiv \left[\!\!\left[ -p\hat{\boldsymbol{n}} + \frac{\mu}{\rho}\frac{\partial \boldsymbol{u}}{\partial \mathrm{n}} \right]\!\!\right]. \tag{5.3}$$

The double brackets $[\![\cdot]\!]$ represent the jump in the value of pressure and shear force when measured on either side of the aerogel. In our model this jump is found by solving for the pressure and shear force on the aerogel interface separately in the region above the aerogel and the region below the aerogel, and taking the difference of the two results.

The force can be split into two components, a radial force and a axial force, which balance the tension forces in the aerogel:

$$f_r \equiv \boldsymbol{f} \cdot \hat{\boldsymbol{e}}_r = -\left(T_a \hat{\boldsymbol{s}}\right)' \cdot \hat{\boldsymbol{e}}_r - T_h \left(\boldsymbol{x} \cdot \hat{\boldsymbol{e}}_r\right), \tag{5.4}$$

$$f_a \equiv \boldsymbol{f} \cdot \hat{\boldsymbol{e}}_a = -\left(T_a \hat{\boldsymbol{s}}\right)' \cdot \hat{\boldsymbol{e}}_a, \tag{5.5}$$

where $\hat{\boldsymbol{e}}_a$ is the unit vector in the axial direction

In order to find the steady state solution of the $\boldsymbol{x}$ position of the aerogel we only need the radial component of the force balance. We assume that the axial tension is much smaller than the hoop tension ($T_a \ll T_h$), simplifying the force balance to:

$$f_r = -T_h \left(\boldsymbol{x} \cdot \hat{\boldsymbol{e}}_r\right). \tag{5.6}$$

We use a B-spline (de Boor, 1972) to describe the position of the aerogel interface $\boldsymbol{x}$. The B-spline is defined by 60 control points that together create a smooth curve spanning the length of the gas valve. The control points are placed so that the aerogel has a uniform radius $R_S$ at the start of the simulation. The control points' axial locations are constant but the radial positions change, to adjust the radius of the aerogel. Each control point defines a weighting field that is used to update its radial position. The first three are static, to keep the inlet radius constant, and the last three control points share the same radial position to ensure the aerogel is not angled at the outlet boundary.

Figure 5.2 shows the gas valve geometry split into two domains by the aerogel, in blue and pink. The domains are solved separately and the resulting difference in the pressure and shear force is used to update the position of the aerogel. The white arrows represent the weighting field belonging to one control point. The weighting field integrated over the radial force on the aerogel, $F_r$, gives the force on that control point. To find the steady-state solution where the force is balanced, each control point moves a small distance proportional to the difference between this force and the hoop tension.

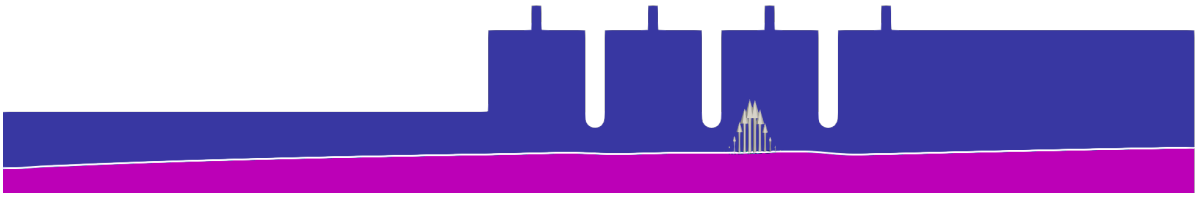

Figure 5.2 The 4-section gas valve configuration used to model the aerogel. The domain is split into two parts by the aerogel. The upper part (blue) and the lower part (pink) are solved independently, and the aerogel interface position is updated based on the resulting difference in pressure and shear force. The white arrows represents the magnitude of the weighting field belonging to one control point.

To find the steady-state equilibrium position of the aerogel we use an interactive method with four steps,

1. solve the flow fields (velocity and pressure) in each of the split domains,
2. calculate the resultant force on the aerogel $\boldsymbol{f}$,
3. move the aerogel interface a small distance proportional to the radial force $f_r$,
4. continue to step 1 until the force is sufficiently small.

Step 2 solves the flow inside and outside the aerogel using the same method as the two-dimensional investigations in chapter 4. The aerogel is extracted manually by winding it on a spool, meaning the aerogel in the gas valve has a prescribed speed, $U_S$. The velocity of the fluid on aerogel interfaces is fixed to the velocity of the aerogel, $U_S\hat{\boldsymbol{s}}$, in order to maintain a no-slip boundary condition.

In step 3 the aerogel is moved by adjusting the B-spline control parameters, and the modelling mesh is regenerated using the new aerogel shape. This iterative process is continued until the force on the aerogel is sufficiently small and the steady-state equilibrium position of the aerogel is approximated.

## 5.3 Results and discussion

The radial force on the interface is the resultant of the pressure differential between flow outside the aerogel, in the gas valve, and the flow within the hollow enclosure of the aerogel ($p_{\text{outside}} - p_{\text{inside}}$) and the hoop tension of the aerogel ($T_h r$). Stallard et al. (2018) found that a processed CNT mat of 60 µm thickness has a elastic modulus of 3 GPa, suggesting a hoop tension value in the order of 180 kN m$^{-1}$. In the model we use a hoop tension value of 1.0 kN m$^{-1}$. This value is chosen as a lower bound of the hoop tension of a much thinner, unprocessed, aerogel. The pressure differential is driven by the boundary condition at the outlet inside the aerogel. We assume there is no net fluid flux through the right boundary in the aerogel, corresponding to the aerogel being flattened as it is extracted and wound up. This corresponds to the common practice of winding up the aerogel on a spindle or drum, or shrinking the aerogel to zero diameter through a liquid bath.

Figure 5.3 shows the pressure field in the gas valve with the interface in place. The white line shows the position of the aerogel. The coloured background shows the pressure field. The pressure inside and outside the aerogel is assumed to be equal at the reactor inlet to the left on the figure. The pressure increases along the length of the gas valve as the flow slows down. The pressure on the inside, below the white line, increases in order to balance the shear force from the aerogel, which is moving left to right.


Figure 5.3 The pressure field in the gas valve. The white line shows the position of the aerogel. Darker / red colours shows higher pressure in the fluid, while bluer / lighter colours shows lower pressure in the fluid. The upper and lower sections separated by the aerogel line are equal at the reactor inlet on the left.

The presence of the aerogel further constricts the flow under the baffles. Under the first and third baffle the flow is flowing backwards causing very strong shear in the flow. Figure 5.4 shows the velocity magnitude of the flow both inside and outside the aerogel interface (white). The velocity is high in the positive horizontal direction (to the right on the figure) along the aerogel (white line), due to the imposed winding velocity of the aerogel. Inside the aerogel, there is high velocity backwards flow along the centreline,

as the flow continuing downstream is being forced back by the flattening of the aerogel. Figure 5.5 shows a more detailed view of the flow just underneath the third baffle, including streamlines in white. The green vertical line shows the location where the velocity has been plotted against the radial position in the flow, shown in figure 5.6. This figure shows the axial (`u_z`, red) and radial (`u_r`, blue) velocities of the fluid, as a function of radial distance from the centreline. The vertical axis shows the fluid velocity in $\mathrm{mm\,s^{-1}}$, the horizontal axis shows the distance from the centreline in mm. The dashed line shows the position of the aerogel interface.

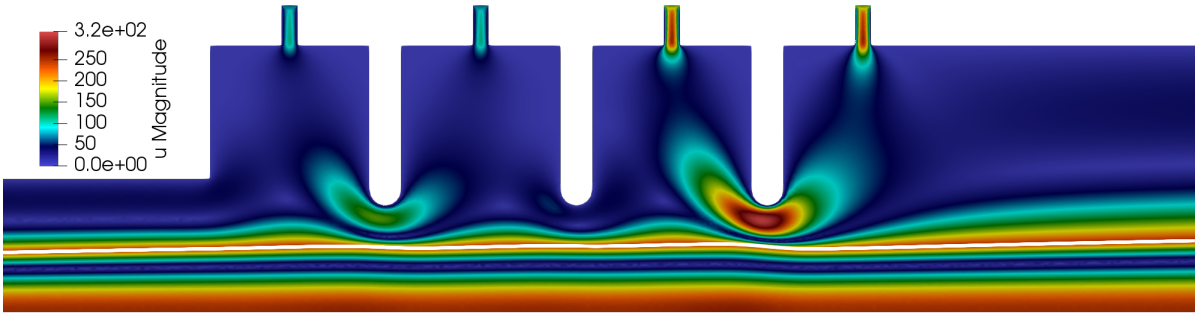


Figure 5.4 Velocity magnitude in the gas valve and the flow inside the aerogel. The velocity is in $\mathrm{mm\,s^{-1}}$. Red colours show high velocity while blue colours show low velocity. The high flow in the second radial inlet/outlet pair causes a strong velocity shear just below the third baffle.

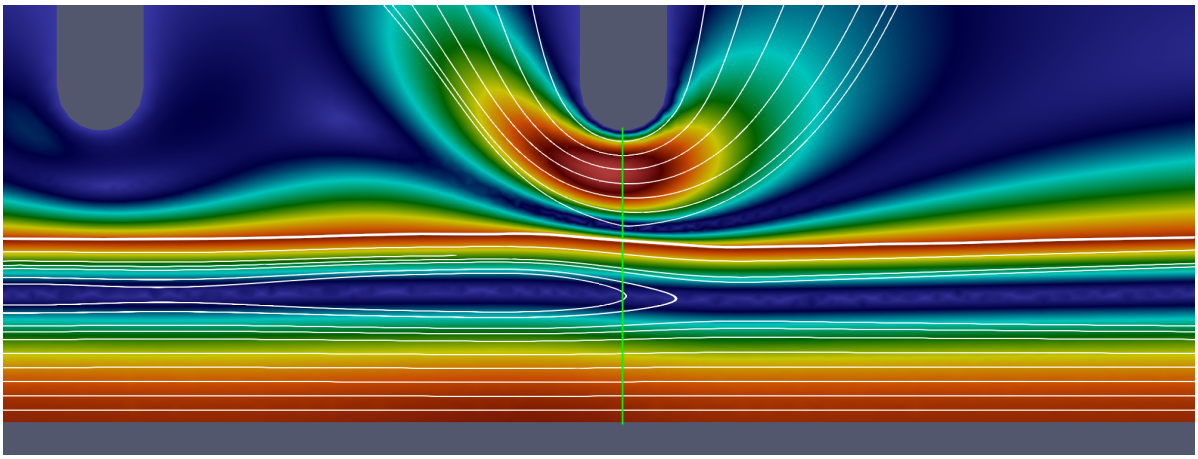

Figure 5.5 Velocity field around the baffle. Red colours show high velocity while blue colours show low velocity. The high velocity around the baffle from the gas valve combined with the high velocity extraction of the aerogel creates a high shear region at the third baffle (green line). The position of the aerogel is shown with the thick white line.

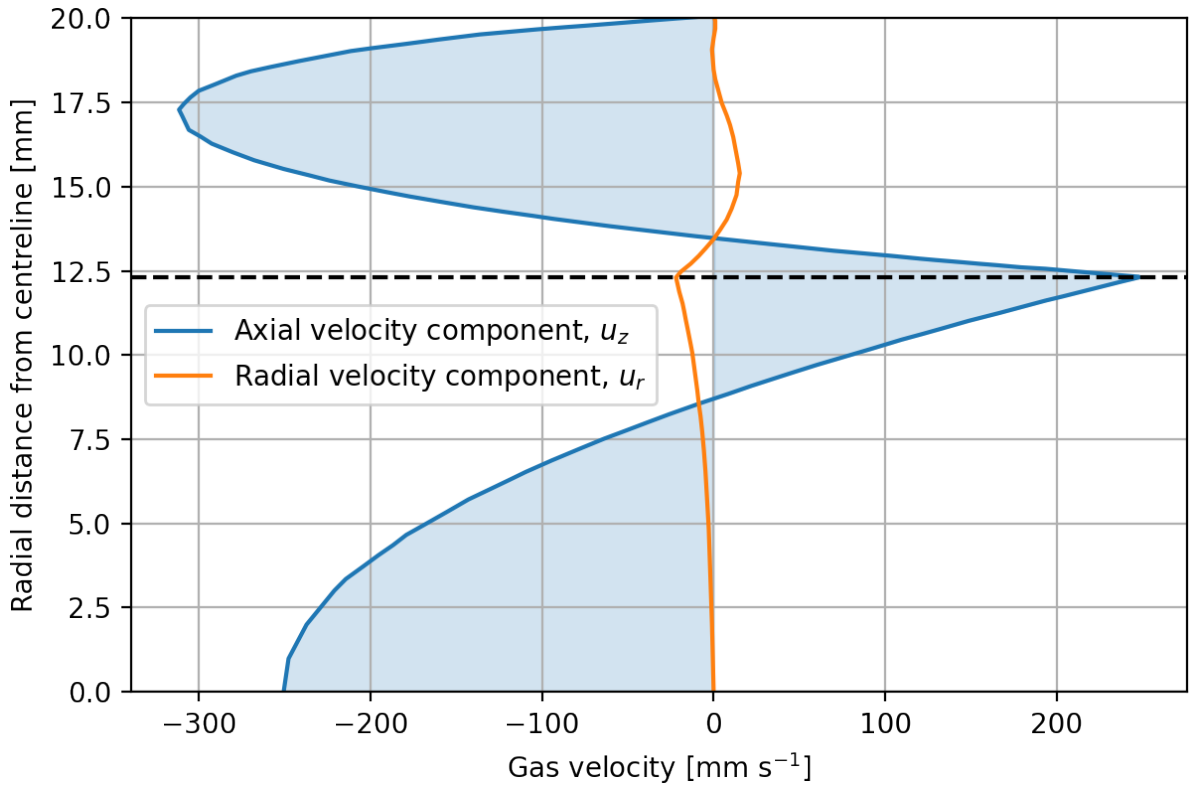


Figure 5.6 Axial ($u_z$, blue line) and radial ($u_r$, orange line) velocity over a radial slice at the third baffle. The vertical axis shows the distance from the centreline in mm, the horizontal axis shows the velocity in mm s$^{-1}$. Positive velocity is moving in the downstream direction (towards the right in Figure 5.5). The dotted line shows the position of the aerogel interface.

## 5.4 Flow stability

During collection of the aerogel through the gas valve there have been reports of the aerogel precessing and occasionally attaching to the gas valve walls and baffles. This interrupts the production process as the reactor needs to be shut down, and the gas valve cleaned before production can resume. We wish to ascertain whether an instability in the flow can explain the observed precession, or if it is predominantly caused by the swirling flow that exists in the laboratory gas valve.

### 5.4.1 Introduction to global stability analysis

We perform a global stability analysis on the flow in our gas valve model, with the aerogel included. A global stability analysis (GSA) solves an eigenvalue problem of a steady-state flow to find the eigenmodes of a flow that have a positive eigenvalue. A positive eigenvalue indicates that the corresponding eigenmode will grow over time and produce a time-varying instability developing on top of the steady-state solution. We present a brief introduction to the subject below. A more detailed introduction to global stability analysis can be found in Brewster (2019).

To perform global stability analysis we start with a solution $\boldsymbol{u}$ that satisfies our governing equations $\boldsymbol{G}$,

$$\boldsymbol{G}(\boldsymbol{u}) = \boldsymbol{0}. \tag{5.7}$$

Our solution, $\boldsymbol{u}$, can vary both in space, $\boldsymbol{x}$, and time, $t$, so we split it into two components, one large component that is constant, $\bar{\boldsymbol{u}}$, and one small component that varies in time, $\boldsymbol{u}'$. We perform a modal decomposition in time of the small, time-varying, component. To look at instabilities that break axial symmetry we also perform a modal decomposition in the azimuthal ($x_\phi$) direction, decomposing the flow into different azimuthal wave numbers $m$:

$$\boldsymbol{u}(\boldsymbol{x}, t) = \bar{\boldsymbol{u}}(\boldsymbol{x}) + \boldsymbol{u}'(x_z, x_r)\mathrm{e}^{st}\mathrm{e}^{\mathrm{i}m\pi x_\phi}, \tag{5.8}$$

$$s = \sigma - \mathrm{i}\omega. \tag{5.9}$$

We can now expand our governing equation into the constant and time-varying parts, ignoring higher-order terms,

$$\boldsymbol{G}(\boldsymbol{u}) = \boldsymbol{G}(\bar{\boldsymbol{u}} + \boldsymbol{u}') = \bar{\boldsymbol{G}}(\bar{\boldsymbol{u}}) + \boldsymbol{G}'(\boldsymbol{u}') + O(\boldsymbol{u}'^2) = \boldsymbol{0}. \tag{5.10}$$

The steady-state solution already satisfies the steady-state governing equation, $\boldsymbol{G}(\bar{\boldsymbol{u}}) = \boldsymbol{0}$, leaving the unsteady governing equation, $\boldsymbol{G}'(\boldsymbol{u}')$. We use the eigenvalue solver SLEPc (Hernandez et al., 2005) to find the eigenmodes, $\boldsymbol{u}'(\boldsymbol{x})$ and eigenvalues, $s = \sigma - \mathrm{i}\omega$, for several different azimuthal wave numbers, $m$. We find solutions where the real part of the eigenvalue $\sigma$ is positive, indicating an instability.

### 5.4.2 Results and discussion

For the global stability analysis, we look at two different boundary conditions on the aerogel, first when the aerogel is treated as a fixed no-slip boundary and second when the aerogel is treated as a flexible boundary that can move. The base case in the stability analysis is the 4-section configuration, with the baffle hole radii all at 30 mm, and $3.0\,\mathrm{L\,min^{-1}}$ flowrate through the second pair of radial inlet and outlet. The extraction velocity of the aerogel is $15\,\mathrm{m\,min^{-1}}$.

The global stability analysis calculates the eigenmodes the flow supports and their corresponding eigenvalues ($s = \sigma - \mathrm{i}\omega$). Each eigenvalue has a real valued growth rate, $\sigma$, and an imaginary valued angular frequency, $\mathrm{i}\omega$. If at least one eigenvalue has a positive real part the flow is unstable. In this axisymmetric flow we also look at the stability of different azimuthal wave numbers, $m$. We use these stability modes to investigate non-axisymmetric modes $m \neq 0$, in addition to the axisymmetric mode $m = 0$. The zeroth mode, $m = 0$, is axisymmetric; the higher-order modes, $m = 1$ and above, correspond to helical disturbances, such as precession. The low order azimuthal modes, $m = 0$ and $m = 1$, are more unstable for flows with low swirl (Loiseleux et al., 1998), therefore we consider only the first 3 modes, $m = 0, 1, 2$.

Figure 5.7 plots the eigenvalues for the different eigenmodes found in the reactor. Figures 5.7(a)-(c) plots the eigenvalues when the aerogel is assumed to be a static, no-slip boundary, while Figures 5.7(d)-(f) plots the eigenvalues when the aerogel is allowed to be a flexible boundary. The eigenvalues are plotted for the three different modes we investigated, $m = 0$, $m = 1$, and $m = 2$. All six stability calculations did not show any unstable modes, which would have positive growth rates (the grey area on the figures).

The first mode of the flexible aerogel has one eigenvalue with a growth rate of $\sigma = -0.59$ that could become unstable at higher flow velocities in the reactor.

Because we found no unstable modes in our stability analysis we conclude that the precession of the aerogel observed in the laboratory is caused only by the swirling flow in the gas valve. The swirling flow is caused by the angling of the gas valve inlets and outlets, and would be avoided if the inlets and outlets were instead radial.

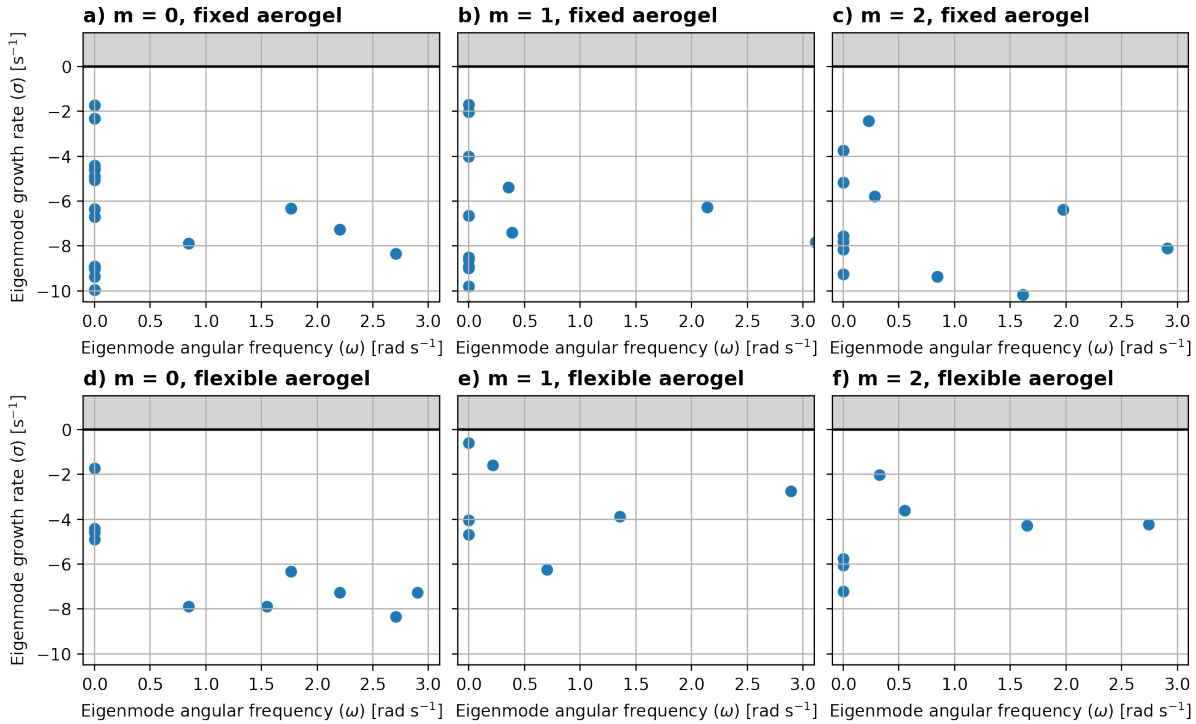


Figure 5.7 The vertical axis shows the growth rate, and and the horizontal axis shows the angular frequency of each eigenmode found in the gas valve with the aerogel present. The upper three figures use the assumption that the aerogel is a fixed boundary, while the lower three figures shows the eigenvalues when the aerogel is flexible. The grey zone above 0 growth rate shows the region where the flow is unstable.

# Part III

# Chemistry and Precursors

# 6 Modelling the precursor behaviour: thiophene and ferrocene

In the Cambridge Process, the reactor is fed with precursors to provide the required iron, sulphur, and carbon for the production of carbon nanotubes. In Li et al. (2004) the precursors were ferrocene, thiophene, and ethanol to provide iron, sulphur and carbon respectively. Kaniyoor et al. (2019) performed several experiments using ferrocene as the iron source, benzyl alcohol as the carbon source, and a varying sulphur source from thiophene, carbon disulphide, or elemental sulphur. Bulmer et al. (2020) further compared the use of toluene with that of benzyl alcohol as a carbon source, using ferrocene and thiophene as the iron and sulphur source. Many studies Hoecker et al. (2016); Hou et al. (2016); Lee et al. (2015) use ferrocene and thiophene as the precursors for iron and sulphur. The review by Weller et al. (2019) also finds that ferrocene and thiophene are the predominant choices. For the CUED and MML reactors the main precursor combination in use is ferrocene ($C_{10}H_{10}Fe$) as the iron source, thiophene ($C_4H_4S$) as the sulphur source, and methane ($CH_4$) as the carbon source.

Understanding precisely the decomposition of the precursors is important because the order in which iron and sulphur are released in the reactor significantly affects the properties of the carbon nanotubes. Earlier release of sulphur produces more single walled carbon nanotubes, while later release of sulphur produces more multi-wall carbon nanotubes (Lee et al., 2015). Thiophene and ferrocene decompose at different temperatures and rates. Therefore the temperature profile in the reactor and the flowrate affects at what point in the reactor iron and sulphur is made available.

The decomposition of ferrocene and thiophene in a hydrogen atmosphere is well studied in inert atmospheres, such as argon or nitrogen, but not in hydrogen. We use the values of ferrocene decomposition from Conroy et al. (2010); Kuwana and Saito (2005) to model the decomposition of ferrocene. We find that the position of decomposition in the model agree with the observed bands of sooty deposition found on the quartz reactor used by Hoecker et al. (2016). For the decomposition of thiophene we instead infer the decomposition parameters from experimental data from Hoecker et al. (2016). We use

an adjoint-driven gradient-based optimisation method to find the best-fit decomposition parameters that explain the experimental data.

## 6.1 Modelling thiophene

We model thiophene and ferrocene as species convecting with and diffusing in the flow. We assume that the species do not affect the flow. This is a reasonable assumption since the mass fraction of thiophene (0.5 mass%) and ferrocene (3.0 mass%) is low (Hoecker et al., 2016). We use the low Mach-number flow model to solve the base flow of the fluid. On top of this model, the mass conservation of the species obeys,

$$\frac{\partial \rho c}{\partial t} + \boldsymbol{\nabla} \cdot (\rho \boldsymbol{u} c) = \boldsymbol{\nabla} \cdot (\rho D_c \boldsymbol{\nabla} c) - \rho c k, \tag{6.1}$$

where $c$ is the concentration of the species (thiophene or ferrocene), $\rho$ and $\boldsymbol{u}$ are the fluid density and velocity as described in Section 3.4, $D_c$ is the diffusivity of the species, and $k$ is the decomposition rate of the species.

We assume the decomposition rate of thiophene and ferrocene can be modelled using Arrhenius equations. Using this assumption $k$ is modelled by,

$$k = A \exp\left(-\frac{E_a}{RT}\right), \tag{6.2}$$

where $A$ is the rate constant, $E_a$ is the activation temperatures of the reaction, $T$ is the temperature of the fluid, and $R$ is the universal gas constant.

We re-arrange this expression into a form that is easier to implement,

$$k = \exp\left(\ln A - \frac{E_a}{RT}\right) = \exp(\beta - T_a/T), \tag{6.3}$$

where $\beta \equiv \ln A$ is the natural logarithm of the rate constant, which we label the rate exponent, and $T_a \equiv E_a/R$ is the activation temperature of the reaction.

## 6.2 Estimating the decomposition parameters

Hoecker et al. (2016) measured the concentration of the thiophene at the outlet of the reactor, at a low flowrate of $0.5\,\mathrm{L\,min^{-1}}$ and at several temperatures. Figure 6.1

presents the experimental observations of Hoecker et al. (2016). They were measured at four different reactor temperatures; 750, 850, 950, and 1050 °C. We also assume that no thiophene decomposes if the reactor is run at room temperature, giving us five data points.

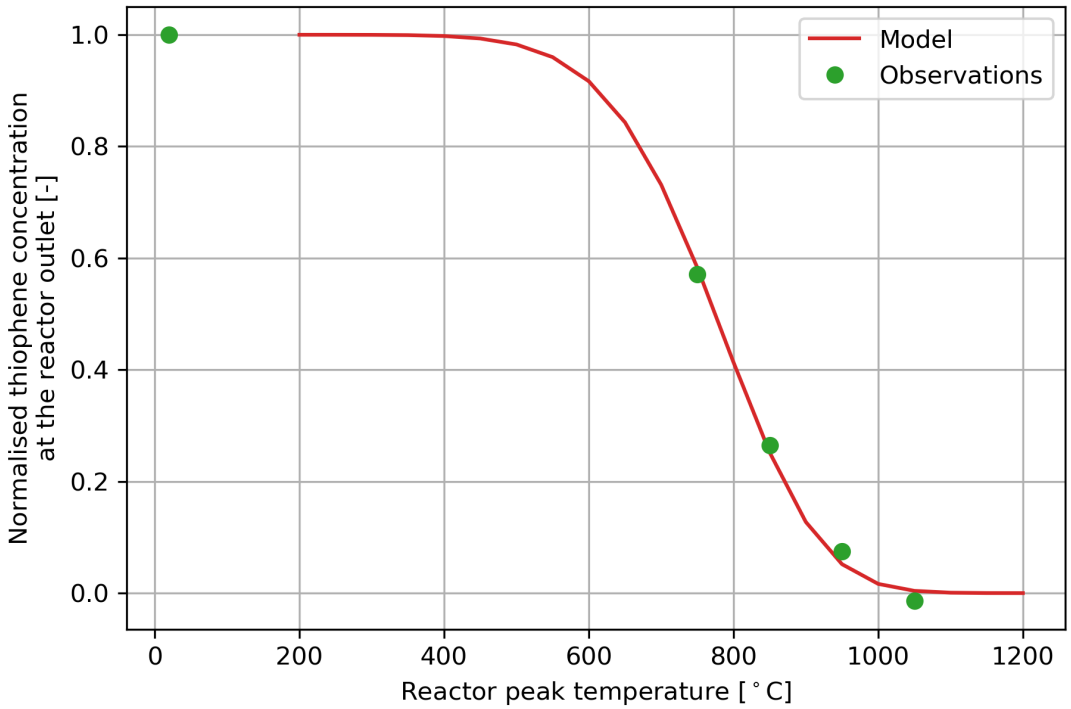


Figure 6.1 Comparison of the thiophene decomposition model (red) with experimental observations (green) from Hoecker et al. (2016). We use the experimental observations to guide a gradient-based optimisation process to find the decomposition parameters that best model the observed decomposition curve of thiophene in the reactor.

We use an adjoint method to calculate the gradients needed for our optimisation. We use the approach described in chapter 2. The adjoint method is suitable for a problem that can be presented as a control problem, with a functional that should be minimised, and constraints that should be maintained. It is particularly useful for the Bayesian inference as it allows us to quickly calculate the gradient of of the objective functional with respect to the parameters.

### 6.2.1 Constructing the objective function

We use the negative log of the posterior probability of the model's parameters as the objective function. The negative log posterior has three main parts: the negative log of the prior, the negative log of the parameter likelihood, and normalisation terms that

are independent of the parameters and the data. Ignoring the normalisation terms, we have a two part objective function:

$$J(\boldsymbol{\theta}, \boldsymbol{x}) = \tfrac{1}{2}(\boldsymbol{\theta} - \boldsymbol{\mu_\theta})^\top \boldsymbol{\Sigma}_{\boldsymbol{\theta}}^{-1}(\boldsymbol{\theta} - \boldsymbol{\mu_\theta}) + \tfrac{1}{2}\left(\boldsymbol{q} - \boldsymbol{x}\right)^\top \boldsymbol{\Sigma}_{\boldsymbol{x}}^{-1}(\boldsymbol{q} - \boldsymbol{x}). \tag{6.4}$$

The first term is the negative log of the prior, where $\boldsymbol{\mu_\theta}$ and $\boldsymbol{\Sigma_\theta}$ are the prior expected value and the prior uncertainty of the parameters, respectively. The second part is the negative log of the parameter likelihood, where $\boldsymbol{x}$ are the experimental observations, and $\boldsymbol{q}$ are the model predictions. The model predictions are the normalised surface averaged thiophene concentrations, $c$, at the reactor outlet, for the different reactor operating conditions:

$$q(c_i) \equiv \frac{1}{c_0}\frac{1}{A}\int_{\text{outlet}} c_i \,\mathrm{d}A, \tag{6.5}$$

where $A = \pi R^2$ is the area of the reactor outlet, and $c_0$ is the concentration of thiophene at the reactor inlet. The thiophene concentration is calculated using the model's parameters $\boldsymbol{\theta}$. To minimise the objective function we use a gradient-based optimisation process. The gradients with respect to the parameters are obtained with the adjoint equation explained in the next section.

### 6.2.2 The first order adjoint

We first construct the Lagrangian of the objective function, by including the constraint on the thiophene concentration $c$,

$$L = J + \langle \lambda, G(c, \boldsymbol{\theta}) \rangle \,, \tag{6.6}$$

where $\lambda$ is the adjoint variable corresponding to the modelling variable $c$, $\langle \cdot, \cdot \rangle$ represents a suitable inner product, in this case a volume integral over the modelling domain, and $G$ is the governing equation for $c$, (6.1). We assume the experimental observations are made in the steady-state. In the steady-state the time-derivative is zero, leaving the governing equation as:

$$G(c, \boldsymbol{\theta}) \equiv \boldsymbol{\nabla} \cdot (\rho \boldsymbol{u} c) - \boldsymbol{\nabla} \cdot (\rho D_c \boldsymbol{\nabla} c) + \rho c k = 0, \tag{6.7}$$

$$k = k(\boldsymbol{\theta}) \equiv \exp\left(\beta - T_a/T\right). \tag{6.8}$$

To use a gradient-based optimisation process to find the best-fit parameters we derive an expression for $\partial L/\partial \boldsymbol{\theta}$. We begin by taking small variations of the Lagrangian,

$$\delta L = \delta J + \langle \lambda, \delta G(c, \boldsymbol{\theta}) \rangle \,, \tag{6.9}$$

$$= \delta J + \left\langle \lambda, \frac{\partial G}{\partial c} \delta c \right\rangle + \left\langle \lambda, \frac{\partial G}{\partial \boldsymbol{\theta}} \delta \boldsymbol{\theta} \right\rangle . \tag{6.10}$$

The variation of the objective function has two terms, one from the variations of the model observation $q$, and one from the variations of the parameters, $\boldsymbol{\theta}$,

$$\delta J = (q - x)\sigma_x^{-1} \frac{\partial q}{\partial c} \delta c + (\boldsymbol{\theta} - \boldsymbol{\mu}_{\boldsymbol{\theta}})^\top \boldsymbol{\Sigma}_{\boldsymbol{\theta}}^{-1} \delta \boldsymbol{\theta}, \tag{6.11}$$

Similarly, the variation of the governing equation has two terms, one from the variations of the concentration $c$, and one from the variations of the parameters, $\boldsymbol{\theta}$,

$$\delta G = \boldsymbol{\nabla} \cdot (\rho \boldsymbol{u} \delta c) - \boldsymbol{\nabla} \cdot (\rho D_c \boldsymbol{\nabla} \delta c) + \rho \delta c k + \rho c \frac{\partial k}{\partial \boldsymbol{\theta}} \delta \boldsymbol{\theta} \tag{6.12}$$

$$= \delta G_c \delta c + \delta G_{\boldsymbol{\theta}} \delta \boldsymbol{\theta}, \tag{6.13}$$

$$\frac{\partial G}{\partial c} \delta c = \boldsymbol{\nabla} \cdot (\rho \boldsymbol{u} \delta c) - \boldsymbol{\nabla} \cdot (\rho D_c \boldsymbol{\nabla} \delta c) + \rho \delta c k, \tag{6.14}$$

$$\frac{\partial G}{\partial \boldsymbol{\theta}} \delta \boldsymbol{\theta} = \rho c \frac{\partial k}{\partial \boldsymbol{\theta}} \delta \boldsymbol{\theta} = \rho c [k \delta \beta - (k/T) \delta T_a]. \tag{6.15}$$

Next we perform integration by parts to shift the derivatives from the variations of the concentration to the adjoint variable $\lambda$,

$$\left\langle \lambda, \frac{\partial G}{\partial c} \delta c \right\rangle = \left\langle G^\dagger \lambda, \delta c \right\rangle , \tag{6.16}$$

$$G^\dagger \lambda \equiv -\rho \boldsymbol{u} \cdot \boldsymbol{\nabla} \lambda - \boldsymbol{\nabla} \cdot (\rho D_c \boldsymbol{\nabla} \lambda) + \rho \lambda k + \text{boundary conditions}, \tag{6.17}$$

where the boundary conditions are presented in appendix A.

After integration-by-parts, the expression of the variations of the Lagrangian is,

$$\begin{aligned}\delta L &= (q-x)\sigma_x^{-1}\frac{\partial q}{\partial c}\delta c + (\boldsymbol{\theta}-\boldsymbol{\mu_\theta})^\top \boldsymbol{\Sigma}_{\boldsymbol{\theta}}^{-1}\delta\boldsymbol{\theta} \\ &\quad + \left\langle G^\dagger\lambda, \delta c\right\rangle + \frac{\partial G}{\partial \boldsymbol{\theta}}\delta\boldsymbol{\theta}, \qquad (6.18)\\ &= (\boldsymbol{\theta}-\boldsymbol{\mu_\theta})^\top \Sigma_{\boldsymbol{\theta}}^{-1}\delta\boldsymbol{\theta} + \frac{\partial G}{\partial \boldsymbol{\theta}}\delta\boldsymbol{\theta} \\ &\quad + (q-x)\sigma_x^{-1}\frac{\partial q}{\partial c}\delta c + \left\langle G^\dagger\lambda, \delta c\right\rangle. \qquad (6.19)\end{aligned}$$

We now choose to define $\lambda$ as the value that eliminates the terms including $\delta c$. The variation in the model observation $\delta\phi(c)$ is evaluated at the outlet boundary. This term is removed by our choice of boundary conditions, making the governing equation for $\lambda$,

$$-\rho\boldsymbol{u}\cdot\boldsymbol{\nabla}\lambda - \boldsymbol{\nabla}\cdot(\rho D_c\boldsymbol{\nabla}\lambda) + \rho\lambda k = 0, \qquad (6.20)$$

$$(q-x)\sigma_x^{-1}\frac{\partial q}{\partial c}\delta c + \text{boundary conditions} = 0. \qquad (6.21)$$

Using this value of the adjoint variable leaves the variations of the Lagrangian as,

$$\delta L = (\boldsymbol{\theta}-\boldsymbol{\mu_\theta})^\top \boldsymbol{\Sigma}_{\boldsymbol{\theta}}^{-1}\delta\boldsymbol{\theta} + \left\langle \lambda, \frac{\partial G}{\partial \boldsymbol{\theta}}\delta\boldsymbol{\theta}\right\rangle, \qquad (6.22)$$

$$\frac{\delta L}{\delta \boldsymbol{\theta}} = (\boldsymbol{\theta}-\boldsymbol{\mu_\theta})^\top \boldsymbol{\Sigma}_{\boldsymbol{\theta}}^{-1} + \left\langle \lambda, \frac{\partial G}{\partial \boldsymbol{\theta}}\right\rangle, \qquad (6.23)$$

$$\left\langle \lambda, \frac{\partial G}{\partial \boldsymbol{\theta}}\right\rangle \equiv \int_V \rho c\lambda \begin{pmatrix} k \\ -k/T\end{pmatrix} \mathrm{d}V. \qquad (6.24)$$

The gradient of the Lagrangian can be calculated by first solving for the adjoint variable, $\lambda$, using the governing equation and boundary conditions in (6.20) and (6.21), and then integrating (6.24).

The power of the adjoint technique is clear when the number of parameters is great, as the adjoint variable only needs to be solved once, and it is only the term $\partial G/\partial\boldsymbol{\theta}$ that scales with the number of parameters. The governing equation of the adjoint is also based on the linearised governing equation, meaning the adjoint governing equation is linear, and less computationally intensive to solve than the direct governing equation in most cases. This means the computational effort needed to perform adjoint-based gra-

dient calculations is lower than for a finite difference approach, for which the governing equation needs to be solved once per parameter.

### 6.2.3 The second order adjoint

We also calculate the second order gradients of the objective function, using the adjoint-adjoint approach of Papadimitriou and Giannakoglou (2008). That paper uses second order adjoints for aerodynamic shape optimisation, but the theoretical approach is equally valid for our case of decomposition modelling. With second order information it is possible to use a Newton method for optimisation, significantly speeding up the optimisation process. Additionally, the second order information allows us to approximate the uncertainty of the posterior probability distribution.

To derive an expression for the second order gradient of the objective function with respect to the model parameters, we take small variations of the first order gradient expression:

$$\frac{\delta L}{\delta \boldsymbol{\theta}} = (\boldsymbol{\theta} - \boldsymbol{\mu}_{\boldsymbol{\theta}})^\top \boldsymbol{\Sigma}_{\boldsymbol{\theta}}^{-1} + \left\langle \lambda, \frac{\partial G}{\partial \boldsymbol{\theta}} \right\rangle, \tag{6.25}$$

$$\delta\left(\frac{\delta L}{\delta \boldsymbol{\theta}}\right) = \boldsymbol{\Sigma}_{\boldsymbol{\theta}}^{-1}\delta\boldsymbol{\theta} + \left\langle \delta\lambda, \frac{\partial G}{\partial \boldsymbol{\theta}} \right\rangle + \left\langle \lambda, \frac{\partial^2 G}{\partial \boldsymbol{\theta}^2}\delta\boldsymbol{\theta} \right\rangle + \left\langle \lambda, \frac{\partial^2 G}{\partial \boldsymbol{\theta}\partial c}\delta c \right\rangle, \tag{6.26}$$

$$\frac{\partial^2 G}{\partial \boldsymbol{\theta}^2}\delta\boldsymbol{\theta} \equiv \rho c \frac{\partial^2 k}{\partial \boldsymbol{\theta}^2}\delta\boldsymbol{\theta} = \rho c \begin{pmatrix} k & -k/T \\ -k/T & k/T^2 \end{pmatrix} \delta\boldsymbol{\theta}, \tag{6.27}$$

$$\frac{\partial^2 G}{\partial \boldsymbol{\theta}\partial c}\delta c \equiv \rho \delta c \frac{\partial k}{\partial \boldsymbol{\theta}} = \rho \begin{pmatrix} k \\ -k/T \end{pmatrix} \delta c. \tag{6.28}$$

We derive the governing equation of $\delta\lambda$ from the governing equation of $\lambda$ (6.20):

$$H(\lambda, \boldsymbol{\theta}) \equiv -\rho \boldsymbol{u} \cdot \boldsymbol{\nabla}\lambda - \boldsymbol{\nabla} \cdot (\rho D_c \boldsymbol{\nabla}\lambda) + \rho\lambda k = 0, \tag{6.29}$$

$$\delta H \equiv \underbrace{-\rho \boldsymbol{u} \cdot \boldsymbol{\nabla}\delta\lambda - \boldsymbol{\nabla} \cdot (\rho D_c \boldsymbol{\nabla}\delta\lambda) + \rho k \delta\lambda}_{\partial H/\partial\lambda\delta\lambda} + \underbrace{\rho\lambda \frac{\partial k}{\partial \boldsymbol{\theta}}\delta\boldsymbol{\theta}}_{\partial H/\partial\boldsymbol{\theta}\delta\boldsymbol{\theta}} = 0 \tag{6.30}$$

We now create a secondary Lagrangian by adding the governing equations of $\delta\lambda$ and $\delta c$ to (6.26), and introduce two new adjoint variables, $\boldsymbol{\phi}$ and $\boldsymbol{\psi}$:

$$\delta\left(\frac{\delta L}{\delta\boldsymbol{\theta}}\right) = \boldsymbol{\Sigma}_{\boldsymbol{\theta}}^{-1}\delta\boldsymbol{\theta} + \left\langle \delta\lambda, \frac{\partial G}{\partial\boldsymbol{\theta}}\right\rangle + \left\langle \lambda, \frac{\partial^2 G}{\partial\boldsymbol{\theta}^2}\delta\boldsymbol{\theta}\right\rangle + \left\langle \lambda, \frac{\partial^2 G}{\partial\boldsymbol{\theta}\partial c}\delta c\right\rangle + \left\langle \boldsymbol{\phi}, \frac{\partial H}{\partial\lambda}\delta\lambda + \frac{\partial H}{\partial\boldsymbol{\theta}}\delta\boldsymbol{\theta}\right\rangle + \left\langle \boldsymbol{\psi}, \frac{\partial G}{\partial c}\delta c + \frac{\partial G}{\partial\boldsymbol{\theta}}\delta\boldsymbol{\theta}\right\rangle \tag{6.31}$$

The first order adjoint variable $\lambda$ has the same dimensionality as the modelling variable $c$, in our case a scalar. The newly introduced adjoint variables, $\boldsymbol{\phi}, \boldsymbol{\psi}$ have the same dimensionality as the outer product of the modelling variable, $c$, and the parameter vector, $\boldsymbol{\theta}$, in this case a vector. If the modelling variable is a vector, however, the new adjoint variables is a two-dimensional tensors.

We perform the adjoint transform:

$$\begin{aligned}\delta\left(\frac{\delta L}{\delta\boldsymbol{\theta}}\right) &= \boldsymbol{\Sigma}_{\boldsymbol{\theta}}^{-1}\delta\boldsymbol{\theta} + \left\langle \frac{\partial G}{\partial\boldsymbol{\theta}}, \delta\lambda\right\rangle + \left\langle \frac{\partial^2 G}{\partial\boldsymbol{\theta}^2}\lambda, \delta\boldsymbol{\theta}\right\rangle + \left\langle \frac{\partial^2 G}{\partial\boldsymbol{\theta}\partial c}\lambda, \delta c\right\rangle \\ &\quad + \left\langle H_\lambda^\dagger\boldsymbol{\phi}, \delta\lambda\right\rangle + \left\langle \frac{\partial H}{\partial\boldsymbol{\theta}}\boldsymbol{\phi}, \delta\boldsymbol{\theta}\right\rangle + \langle G_c^\dagger\boldsymbol{\psi}, \delta c\rangle + \left\langle \frac{\partial G}{\partial\boldsymbol{\theta}}\boldsymbol{\psi}, \delta\boldsymbol{\theta}\right\rangle, \qquad (6.32)\\ &= \boldsymbol{\Sigma}_{\boldsymbol{\theta}}^{-1}\delta\boldsymbol{\theta} + \left\langle \frac{\partial^2 G}{\partial\boldsymbol{\theta}^2}\lambda, \delta\boldsymbol{\theta}\right\rangle + \left\langle \frac{\partial H}{\partial\boldsymbol{\theta}}\boldsymbol{\phi}, \delta\boldsymbol{\theta}\right\rangle + \left\langle \frac{\partial G}{\partial\boldsymbol{\theta}}\boldsymbol{\psi}, \delta\boldsymbol{\theta}\right\rangle \\ &\quad + \left\langle H_\lambda^\dagger\boldsymbol{\phi} + \frac{\partial G}{\partial\boldsymbol{\theta}}, \delta\lambda\right\rangle + \left\langle G_c^\dagger\boldsymbol{\psi} + \frac{\partial^2 G}{\partial\boldsymbol{\theta}\partial c}\lambda, \delta c\right\rangle \\ &\quad + \text{boundary conditions}, \qquad (6.33)\end{aligned}$$

where we make use of the fact that several terms are free from derivatives and therefore are self adjoint, such as $\langle\lambda, \delta G_{\boldsymbol{\theta}c}\delta c\rangle = \langle\delta G_{\boldsymbol{\theta}c}\lambda, \delta c\rangle$. As for the first order adjoint variable, the boundary conditions are very important for a correct model, and are derived in Appendix A.

As for the first order adjoint, we now choose our second order adjoint variables such that the terms involving $\delta\lambda$ and $\delta c$ are eliminated,

$$\left\langle H_\lambda^\dagger\boldsymbol{\phi} + \frac{\partial G}{\partial\boldsymbol{\theta}}, \delta\lambda\right\rangle + \text{boundary conditions} = 0, \tag{6.34}$$

$$\left\langle G_c^\dagger\boldsymbol{\psi} + \frac{\partial^2 G}{\partial\boldsymbol{\theta}\partial c}\lambda, \delta c\right\rangle + \text{boundary conditions} = 0. \tag{6.35}$$

The volume integral terms are,

$$H_\lambda^\dagger \boldsymbol{\phi} + \frac{\partial G}{\partial \boldsymbol{\theta}} = \boldsymbol{\nabla} \cdot (\rho \boldsymbol{u} \boldsymbol{\phi}) - \boldsymbol{\nabla} \cdot (\rho D \boldsymbol{\nabla} \boldsymbol{\phi}) + \rho \boldsymbol{\phi} k + \rho c \frac{\partial k}{\partial \boldsymbol{\theta}} = 0, \tag{6.36}$$

$$G_c^\dagger \boldsymbol{\psi} + \frac{\partial^2 G}{\partial \boldsymbol{\theta} \partial c} \lambda = -\rho \boldsymbol{u} \cdot \boldsymbol{\nabla} \boldsymbol{\psi} - \boldsymbol{\nabla} \cdot (\rho D_c \boldsymbol{\nabla} \boldsymbol{\psi}) + \rho \boldsymbol{\psi} k + \rho \lambda \frac{\partial k}{\partial \boldsymbol{\theta}} = 0. \tag{6.37}$$

These two equations are coupled, because $\boldsymbol{\psi}$ appears in the boundary condition for $\boldsymbol{\phi}$. The boundary conditions are derived in Appendix A.

Eliminating the expressions containing $\delta\lambda$ and $\delta c$ leaves,

$$\delta \left( \frac{\delta L}{\delta \boldsymbol{\theta}} \right) = \boldsymbol{\Sigma}_{\boldsymbol{\theta}}^{-1} \delta \boldsymbol{\theta} + \left\langle \frac{\partial H}{\partial \boldsymbol{\theta}} \boldsymbol{\phi}, \delta \boldsymbol{\theta} \right\rangle + \left\langle \frac{\partial G}{\partial \boldsymbol{\theta}} \boldsymbol{\psi}, \delta \boldsymbol{\theta} \right\rangle, \tag{6.38}$$

$$\frac{\delta^2 L}{\delta \boldsymbol{\theta}^2} = \boldsymbol{\Sigma}_{\boldsymbol{\theta}}^{-1} + \int_V \frac{\partial H}{\partial \boldsymbol{\theta}} \boldsymbol{\phi} \, \mathrm{d}V + \int_V \frac{\partial G}{\partial \boldsymbol{\theta}} \boldsymbol{\psi} \, \mathrm{d}V, \tag{6.39}$$

$$= \boldsymbol{\Sigma}_{\boldsymbol{\theta}}^{-1} + \int_V \rho \lambda \frac{\partial k}{\partial \boldsymbol{\theta}} \boldsymbol{\phi} \, \mathrm{d}V + \int_V \rho c \frac{\partial k}{\partial \boldsymbol{\theta}} \boldsymbol{\psi} \, \mathrm{d}V \tag{6.40}$$

### 6.2.4 The posterior

We use a Newton method (chapter 2) to find the set of parameters that minimises the objective function. After the optimisation process finds a suitable solution we can construct the posterior probability distribution of our model parameters. The parameters found by the optimisation process are the expected value of the posterior $\boldsymbol{\mu}_p$, while the second order gradient gives the inverse of the covariance matrix of the posterior, $\boldsymbol{\Sigma}_p^{-1}$. From this we construct the posterior probability distribution, which gives the uncertainty of the optimised parameters:

$$P(\boldsymbol{\theta} \mid \boldsymbol{x}, H) = \tfrac{1}{Z} \exp\left( \tfrac{1}{2} (\boldsymbol{\theta} - \boldsymbol{\mu}_p)^\top \boldsymbol{\Sigma}_p^{-1} (\boldsymbol{\theta} - \boldsymbol{\mu}_p) \right). \tag{6.41}$$

## 6.3 Demonstrating the Bayesian inference with synthetic data

To demonstrate how to use adjoints and gradient information for Bayesian information we generate synthetic data for which we know the ground truth parameters. We generate a ground truth solution with a known set of parameters, $T_a = 12\,000\,\mathrm{K}, \beta = 8.57$. We sample the ground truth solution along the reactor length to generate a data set for which

we only need to solve the thiophene model once. To simulate experimental uncertainty we add Gaussian noise to our samples, with a mean of 0 and standard deviation of 0.03, producing our synthetic data set. Figure 6.2 shows the ground truth data (green solid line) and the synthetic data generated from the ground truth (green circles).

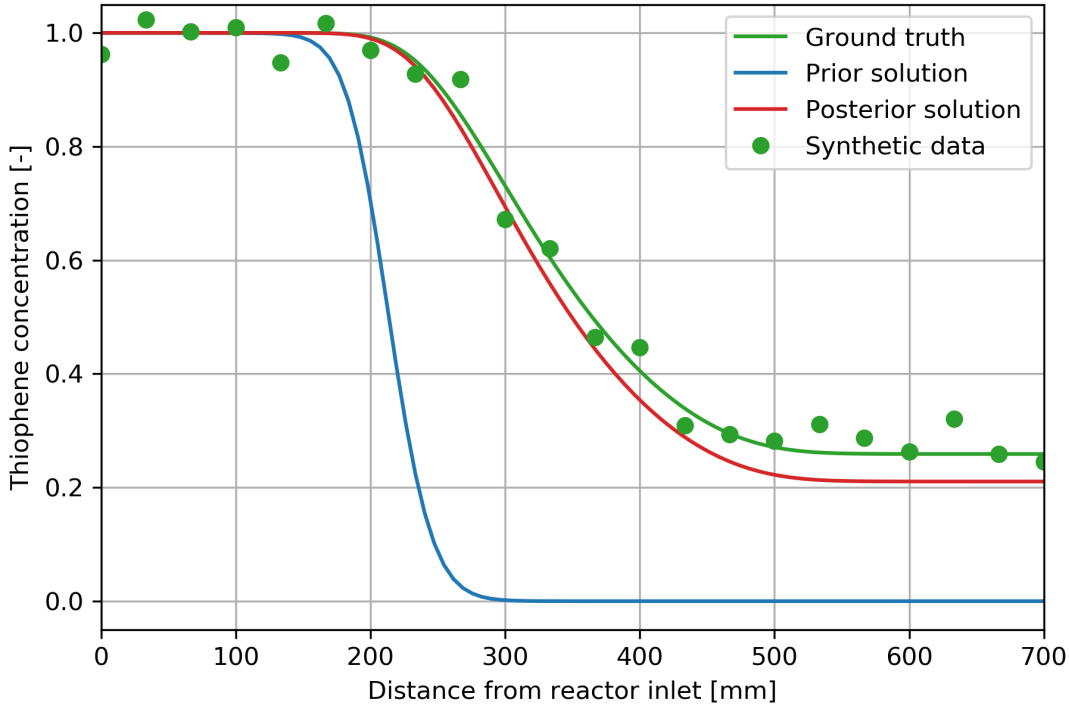


Figure 6.2 Plot of the ground truth solution (green line) generating the synthetic data (green circles), the prior solution (blue) before optimisation, and the posterior solution (red) after optimisation.

For our prior, we intentionally choose model parameters that produce a solution with poor data fit, shown in blue on figure 6.2. After three iterations a solution is found that satisfies the gradient tolerance limit, show in red on figure 6.2.

The optimisation path, the prior mean and uncertainty, and the posterior mean and uncertainty are shown in parameter space on figure 6.3. The blue square shows the prior mean, and the blue ellipses show the $\frac{1}{4}\sigma$ and $\frac{1}{8}\sigma$ confidence bounds on the prior. The red circle shows the posterior mean, and the red ellipses show the $\frac{1}{4}\sigma$ and $\frac{1}{8}\sigma$ confidence bounds on the posterior. The black cross shows the ground truth parameter used to generate the noisy synthetic data. The dotted black line shows the path the optimisation process takes from prior to posterior. The background colours shows the objective value of the data only (discounting the objective penalty from the prior), the yellow end of the scale shows regions of poor fit with the synthetic data, while the blue

end of the scale shows regions with good fit with the synthetic data. The ground truth marker deviates from the location of minimum negative log likelihood because we added noise to the synthetic data.

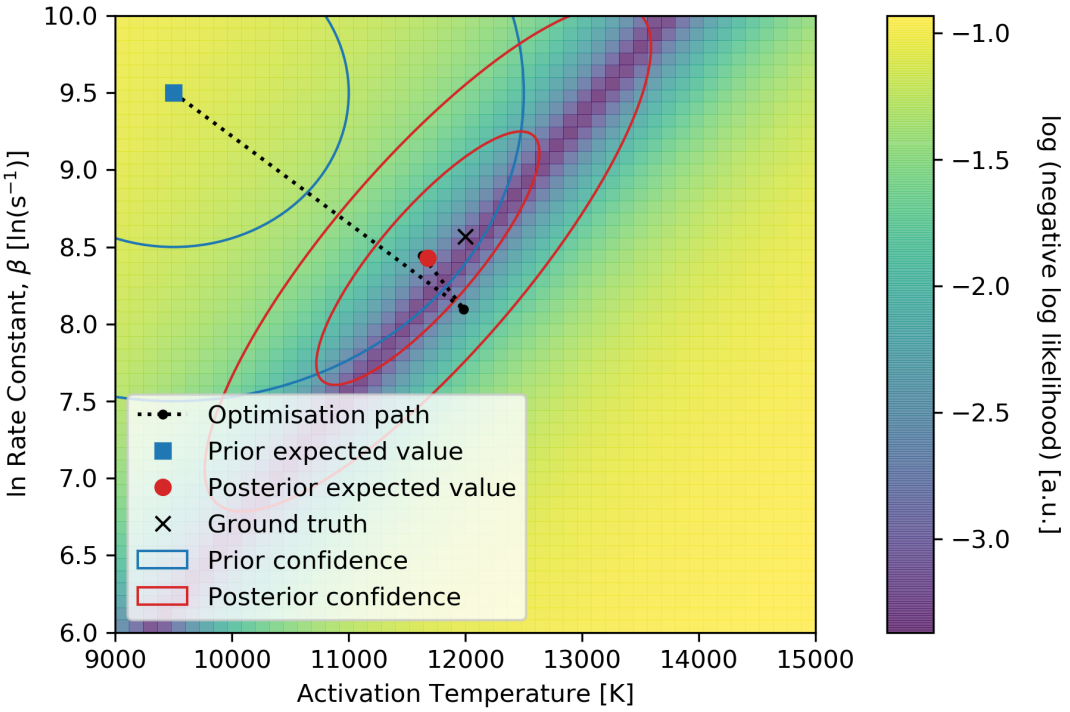


Figure 6.3 Confidence interval plots of the prior (blue) and posterior (red). The inner and outer ellipses show the one eighth and one quarter standard deviation confidence intervals respectively. The background colour shows the log of the negative log likelihood of the parameters given the data. The black dotted line shows the path of the optimisation, starting from the prior. The cross marks the ground truth parameters that generated the noisy data.

The numerical values of the prior, posterior and ground truth are listed here,

$$\text{prior} : \boldsymbol{\mu}_f = \begin{bmatrix} 9500 \\ 9.50 \end{bmatrix}, \Sigma_f = \begin{bmatrix} 12000 & 0 \\ 0 & 8.00 \end{bmatrix}, \tag{6.42}$$

$$\text{posterior} : \boldsymbol{\mu}_p = \begin{bmatrix} 11678 \\ 8.43 \end{bmatrix}, \Sigma_p = \begin{bmatrix} 7650 & 205 \\ 205 & 6.57 \end{bmatrix}, \tag{6.43}$$

$$\text{ground truth} : \boldsymbol{\mu}_t = \begin{bmatrix} 12000 \\ 8.57 \end{bmatrix}. \tag{6.44}$$

The posterior is within 2.7 % and 1.6 % of the ground truth for the activation temperature $T_a$ and the rate exponent $\beta$, respectively. This shows that the optimisation process

works, and that the adjoint method of producing the first and second order gradients is valid.

## 6.4 Applying Bayesian inference to the experimental observations.

To apply Bayesian inference to the experimental observations of Hoecker et al. (2016) we first need to select a prior distribution on the decomposition parameters.

We have one reference point against which we can compare our prior distribution. Ur Rahman Memon et al. (2003) studied the decomposition of thiophene in argon, using a shock tube experiment. Their estimated decomposition parameters are listed in equation (6.45) below. The conditions of their environment deviate significantly from the conditions in our reactor. In the reactor the environment is mainly hydrogen gas. The high temperature hydrogen gas found in the reactor contains a significant concentration of free hydrogen radicals. We do not know how the free radicals affect the decomposition of thiophene, so we account for this uncertainty with a very large prior covariance,

$$\text{prior} : \boldsymbol{\mu}_f = \begin{bmatrix} 32\,473 \\ 26.12 \end{bmatrix}, \Sigma_f = \begin{bmatrix} 200\,000 & 0 \\ 0 & 100.00 \end{bmatrix}. \tag{6.45}$$

To improve the convergence of the optimisation process we select a starting point that differs from the estimated value of the prior, with a value of $T_a = 12000$ and $\beta = 8.0$.

Figure 6.4 shows the decomposition trend predicted by the expected values of the prior (in blue), and the posterior (in red), compared against the observations (in green). After the optimisation process using Bayesian inference, the posterior predicts the observations very accurately, within 0.03 units of normalised thiophene concentration. The numerical value of the posterior is,

$$\text{posterior} : \boldsymbol{\mu}_p = \begin{bmatrix} 12851 \\ 9.35 \end{bmatrix}, \Sigma_p = \begin{bmatrix} 23786 & 724 \\ 724 & 2.09 \end{bmatrix}. \tag{6.46}$$

The optimisation path is shown in figure 6.5. The background colour shows the logarithm of the objective function, which is the negative log likelihood of the parameters given the

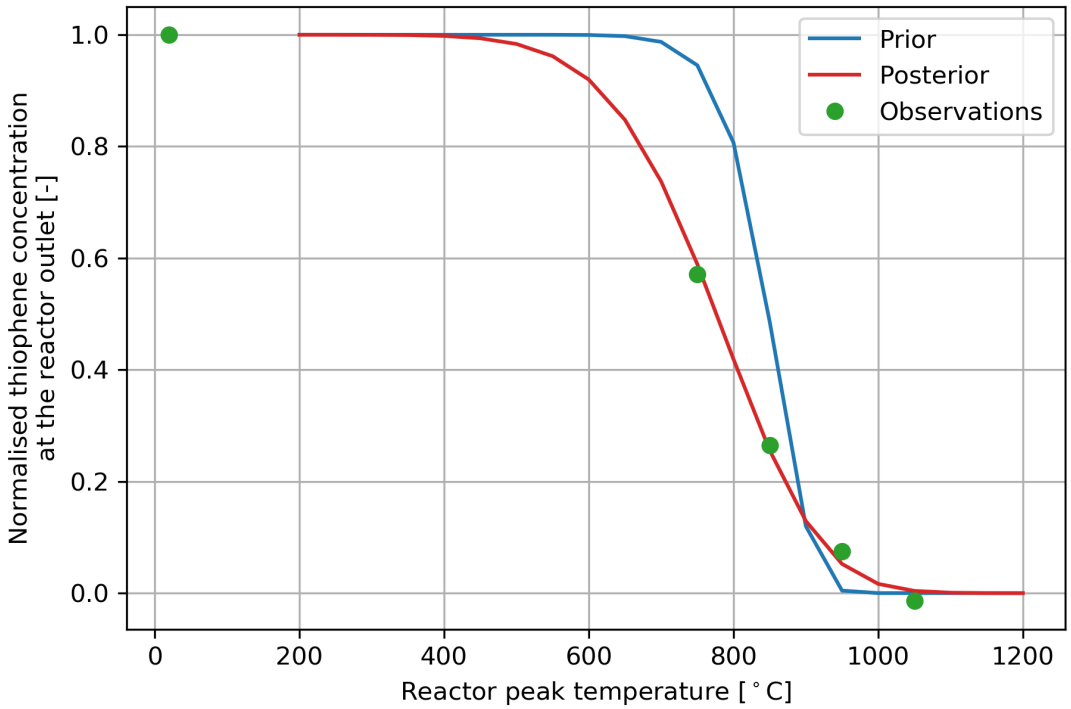


Figure 6.4 Plot of the prior solution (blue) before optimisation, and the posterior solution (red) after optimisation. The experimental observations are marked with the green circles.

data. The valley that can be seen stretching diagonally across the figure demonstrates that a range of pairs of decomposition parameters will generate similar decomposition curves, which all fit the experimental observations well. To reduce the ambiguity of the parameters, more observations at different flowrates are needed, in addition to the observations at different peak reactor temperatures.

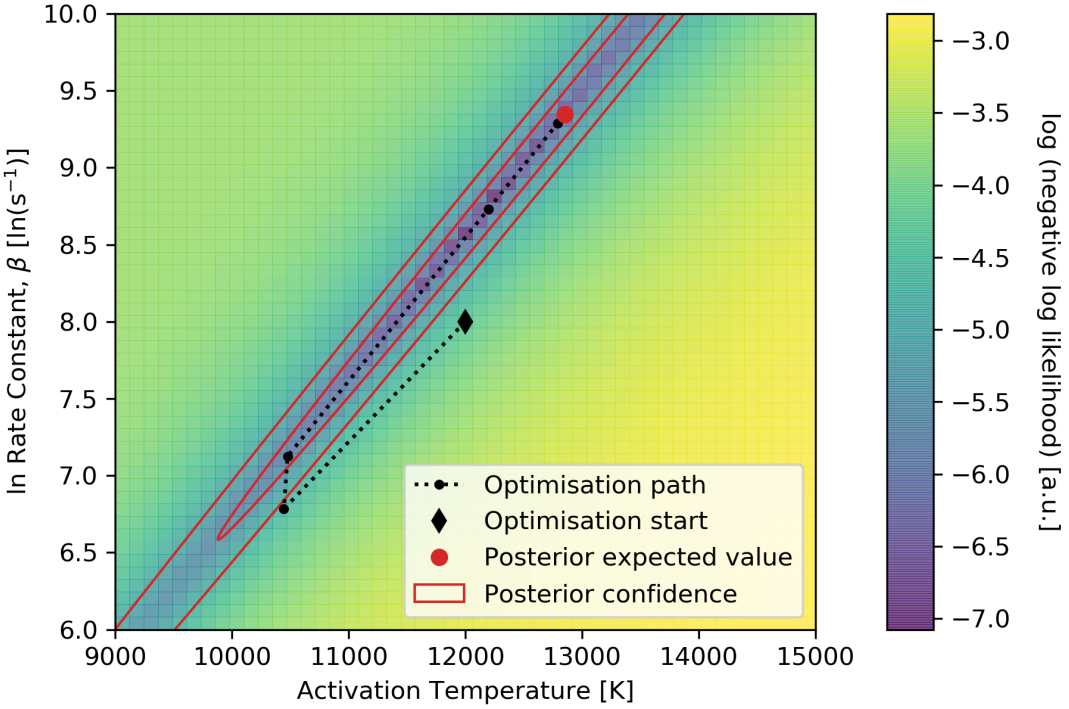


Figure 6.5 Confidence plots of the posterior. The inner and outer ellipses show the one eighth and one quarter standard deviation confidence intervals respectively. The background colour shows the log of the negative log likelihood of the parameters given the data. The black dotted line shows the path of the optimisation, starting from the diamond.

The posterior produced using our method and the sparse experimental observations we have access to is only usable for modelling the particular reactor condition used in the Cambridge process. In order to produce a predictive model more experimental data on the decomposition of thiophene in different temperatures and flowrates is needed. The next studies described in this thesis all use the optimised decomposition parameters to model the decomposition of thiophene in the reactor.

# 7 Reactor inlet conditions and the precursor decomposition

In the reactor studied in the previous chapters (Hoecker et al., 2016), the upstream inlet is a diffuser injector, which allows the flow to develop fully to a parabolic flow a very short distance downstream. By contrast, the reactor used in the Macromolecular Materials Laboratory (Kaniyoor et al., 2019) uses a jetting inlet. The jetting inlet produces a jet that reaches far downstream in the reactor before the streamlines hit the walls. After the streamlines hit the walls the flow becomes parabolic (Revuelta et al., 2002). Because the distance taken for flow with the diffuser inlet to fully develop to a parabolic flow is very short, our model approximates the diffuser inlet by prescribing a parabolic flow at the model inlet.

Figure 7.1 shows the temperature fields and streamlines in the reactor, contrasting the effect of the two inlets. The top half shows the streamlines and temperature for a jetting inlet, which agrees well with the analytical model by Revuelta et al. (2002), and the previous simulation of the flow in the reactor by Conroy et al. (2010). The bottom half shows the streamlines and temperature for a parabolic inlet, which agrees with the simulation performed by Hoecker et al. (2016). The parabolic inlet begins at the top of the reactor, while the jetting inlet exits at the end of a nozzle 0.13 m into the reactor. In the model reactor we add a wall at the jetting inlet entry point to simplify the modelling. In the physical reactor there is no blockage at the nozzle entry point, and the recirculation would extend to the upstream wall at 0 m. With the jetting inlet, the cold inlet flow penetrates quickly into the heated region of the reactor. Beyond the jet length the temperature field becomes nearly identical for both inlet conditions. The velocity of the fluid in the jet is significantly higher than the velocity in the parabolic flow, and therefore the precursors reach the hot zone faster in the jet inlet compared to the diffuser inlet.

In the jetting flow, thiophene and ferrocene decompose further downstream in the reactor. Figure 7.2 shows the decomposition profiles of the thiophene and ferrocene, for the two different inlet conditions. The profiles show fraction of the precursor that remains,

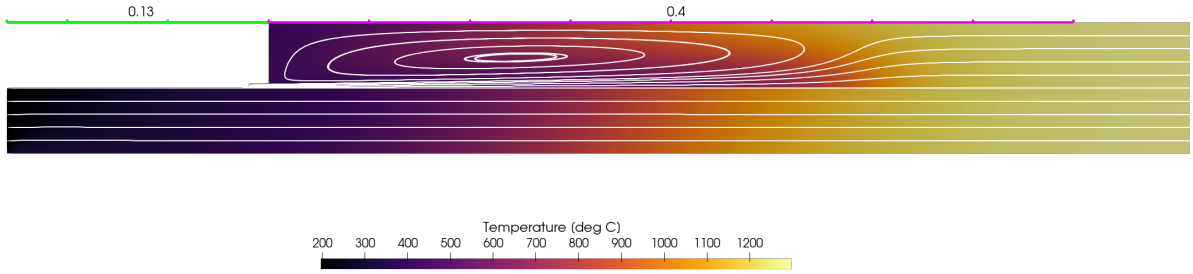


Figure 7.1 Comparison of the temperature field for a jetting inlet (top half) and a parabolic inlet (bottom half). Both flows have the same temperature profile at the walls, and have an inlet flowrate of $5\,\mathrm{L\,min^{-1}}$. The background colour corresponds to the temperature of the flow. The white lines show streamlines of the flow. The first measurement line shows the length of the injector, 0.13 m into the reactor. The jetting model domain does not include the region of the reactor above the jet inlet. The second line marks the length of the jet, 0.40 m downstream, which shows the region where the jetting strongly affects the flow, and the temperature, in the reactor.

as a function of distance from the inlet along the horizontal axis. The profiles are measured from the centreline of the model. The solid lines show the profiles for the jetting inlet, while the dashed lines show the profiles for the parabolic inlet. The red lines show the profiles for the ferrocene decomposition, while the blue lines show the profiles for the thiophene decomposition. Each subfigure corresponds to a specific flow rate, as listed on the left of each figure. At flow rates below $2\,\mathrm{L\,min^{-1}}$ the decomposition profiles for both inlets are very similar. As the flowrate increases, all species decomposes further downstream. For the case of parabolic flow (dashed lines) the increase in downstream distance is small for both thiophene and ferrocene. For the case of the jetting flow (solid lines) the increase in downstream distance is small for thiophene but large for ferrocene. This increase in the downstream distance is due to the reduced temperature in the flow at the higher flowrates. As the flowrate increases the residence time decreases and the temperature is reduced upstream of the heated region. This reduction in temperature reduces the rate at which thiophene and ferrocene breaks down. For thiophene, where the decomposition is slower but starts at a lower temperature, this reduction in temperature means the decomposition occurs over a larger range of downstream distances. For ferrocene, the decomposition is much faster but requires a critical temperature to be reached. The reduction in temperature means the decomposition begins further downstream in the reactor, but does not take a significantly longer time to complete.

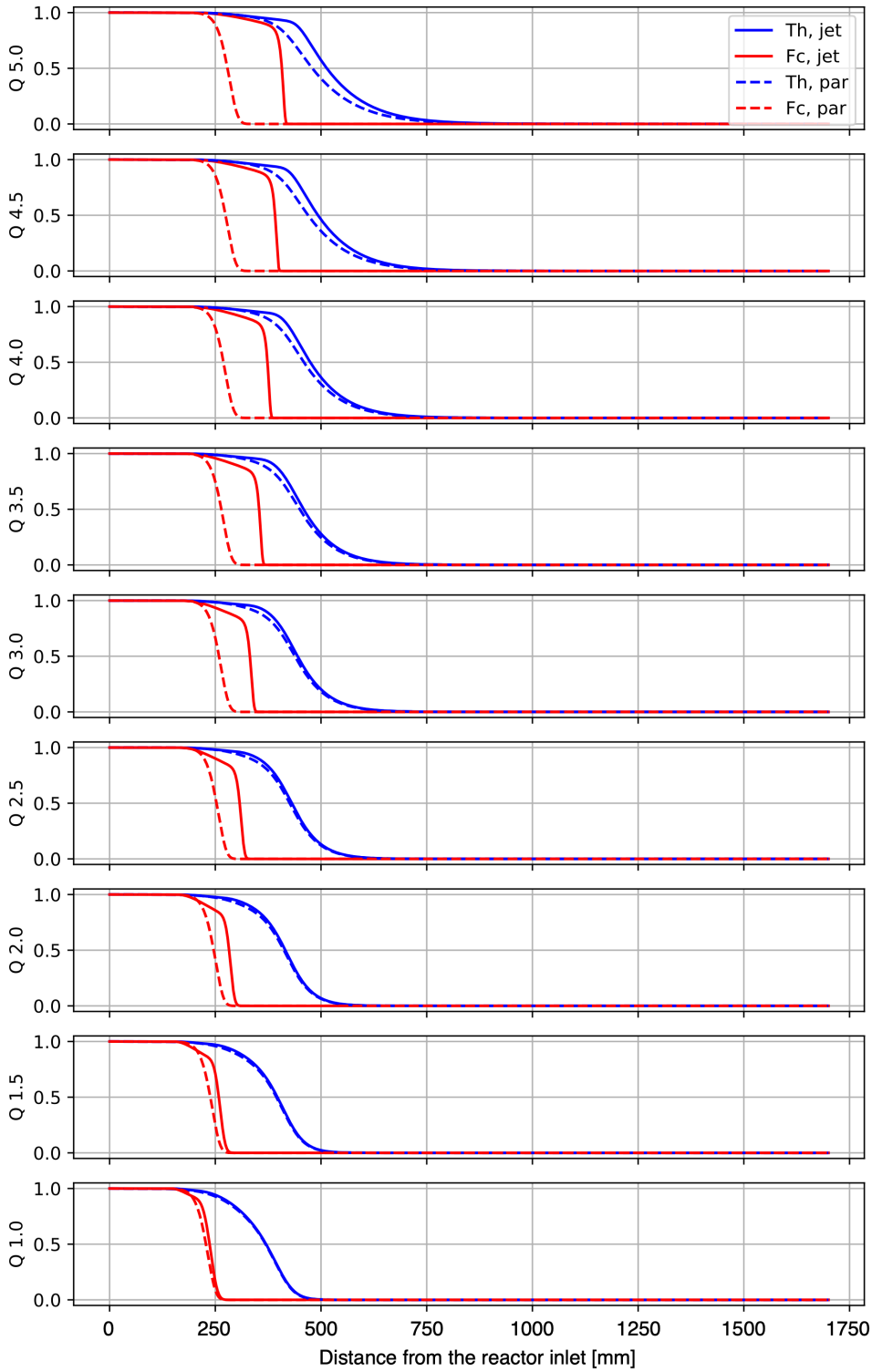


Figure 7.2 Comparison of decomposition profiles for the jetting inlet (solid lines) and parabolic inlet (dashed lines). The red lines show the profile for ferrocene, labelled "Fc", the blue lines the profile for thiophene, labelled "Th". The horizontal axis shows the distance from the reactor inlet, in millimetres.

The data from Figure 7.2 can be seen more succinctly in Figure 7.3. Here, the decomposition range, from 5% to 95% completed decomposition of the precursor is plotted as a field, with the flowrate ($Q$) on the horizontal axis, and distance from the inlet on the vertical axis. The red colour shows the extent of the ferrocene decomposition region, from the 5% bound on the bottom to the 95% bound on the top of the coloured region. The blue regions shows the same region for thiophene. The solid lines in the figure on the left, and the dashed lines in the figure on the right, show the midpoint of the decomposition, where 50% of the precursor has decomposed. The black dash-dotted line in both figures shows the point where the temperature reaches 1100 °C. At this point we suspect the methane becomes activated, and is able to produce carbon nanotubes.

In the low flow rate regime, where the flow rate is less than $2\,\mathrm{L\,min^{-1}}$, both the jet inlet and the parabolic inlet produce similar decomposition fields, as also seen in Figure 7.2. As the flow rate increases, the thiophene decomposes further downstream in the reactor for both inlets. For the parabolic inlet the ferrocene decomposition stays in a narrow range upstream of the thiophene decomposition, as seen in the left plot on Figure 7.3. For the jetting inlet, however, the ferrocene decomposition region is pushed further downstream as the flow rate increases. At high flow rates, $3.5\,\mathrm{L\,min^{-1}}$ and higher, the bulk of the ferrocene decomposition, the last 50% of the decomposition, overlaps with the start of the thiophene decomposition.

This overlap in the decomposition of the ferrocene and thiophene at high flow rates is even more evident if the decomposition regions are plotted as a function of reactor temperature, as shown in Figure 7.4, or as a function of reactor residence time, as shown in Figure 7.5 and Figure 7.6. Figure 7.5 shows the decomposition of the precursor plotted against the reactor residence time of the precursor, as a logarithmic scale on the vertical axis. As the flow rate increases, the residence time decreases, because the fluid velocity increases and the precursor spends less time in the reactor before it reaches decomposition temperatures and begins to decompose. In this figure it is noticeable that the parabolic inlet (figure on the right) has a significantly higher residence time than the jetting inlet. The jet achieves higher velocities in the core of the jet and pushes the precursor to the decomposition region is a very short time, less than 1 s for the ferrocene in the jetting flow, compared to 3 s to 10 s for the ferrocene in the parabolic flow.

Figure 7.6 shows the travel time in the reactor of the precursor until decomposition for the jetting inlet, on a linear time scale on the vertical axis. The left plot shows the full decomposition region, while the right plot shows a zoomed-in region from 0 s to 1 s. The

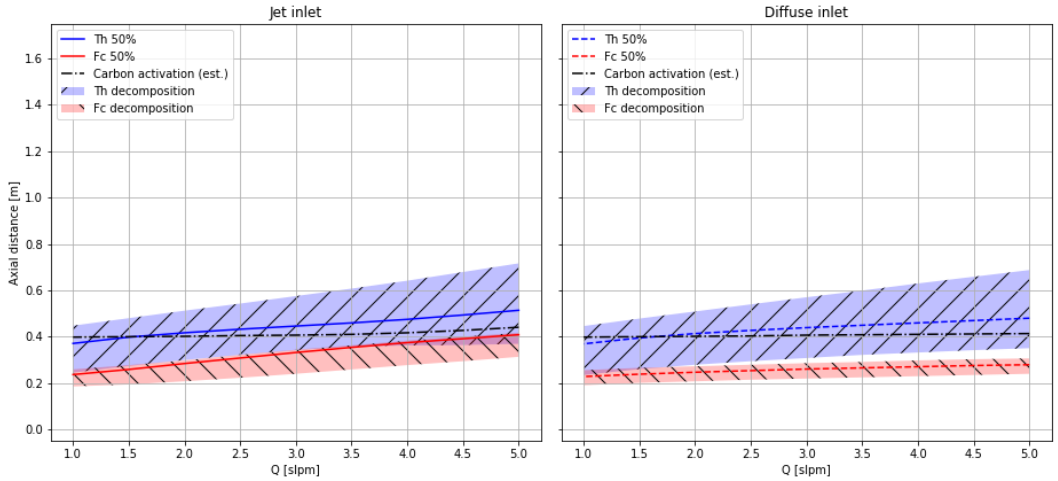


Figure 7.3 Comparison of the boundaries of 5% (decomposition just started) and 95% (decomposition nearly finished) thresholds of decomposition progress of both ferrocene (red, labelled "Fc") and thiophene (blue, labelled "Th") for a jetting inlet (left) and a parabolic inlet (right). The red and blue solid lines show the point of 50% decomposition, for ferrocene and thiophene respectively. The vertical axis shows the distance from the inlet where the decomposition starts (lower boundary) and ends (upper boundary). The horizontal axis shows the flowrates through the reactor. The black dash-dotted line shows the estimated point where the carbon source becomes active in producing carbon nanotubes.

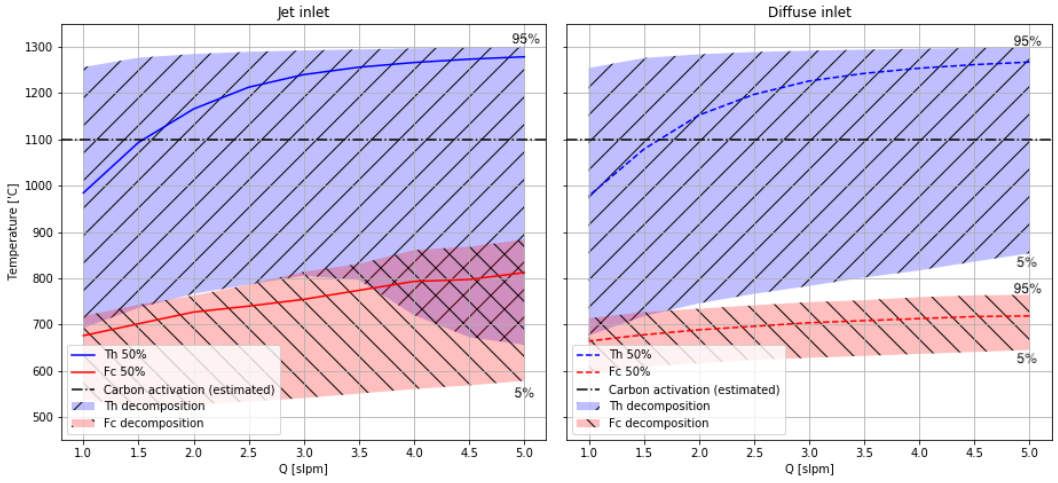


Figure 7.4 Comparison of the boundaries of 5% (decomposition just started) and 95% (decomposition nearly finished) thresholds of decomposition progress of both ferrocene (red, labelled "Fc") and thiophene (blue, labelled "Th") for a jetting inlet (left) and a parabolic inlet (right). The solid lines show the point of 50% decomposition. The dash-dotted line at 1100 °C shows the estimated temperature where the carbon source activates and start to produce carbon nanotubes.

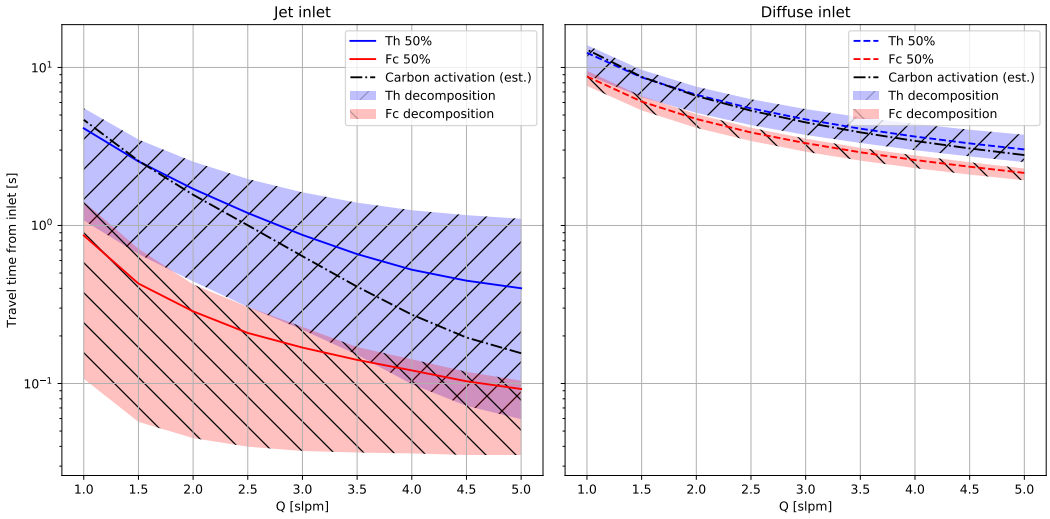


Figure 7.5 As for Figure 7.4 but with the vertical axis showing the time take for a unit of fluid to travel from the inlet to the particular point where precursor is decomposing. The travel time is also shown on a logarithmic scale to more easily see the effects of high flowrate in the jetting inlet. The jetting inlet shows on the left and the parabolic inlet is shown on the right.

zoomed-in view shows that as the flow rate increases above $3\,\mathrm{L\,min^{-1}}$ the decomposition overlap grows to around 50 ms. 50 ms is sufficient time for particles to nucleate, so at the high flow rates some particles are expected to have nucleated in a sulphur-rich environment, compared to the sulphur-poor environment for lower flow rates in the jet inlet, or any flow rates for the parabolic inlet.

## 7.1 Nucleation in a sulphur-rich environment

Kaniyoor et al. (2019) find that the number of walls in the individual carbon nanotubes changes as the flowrate in the reactor increases. Lower flowrates, below $2.5\,\mathrm{L\,min^{-1}}$, produce predominantly mutli-walled carbon nanotubes, while higher flowrates, above $2.5\,\mathrm{L\,min^{-1}}$, produce predominantly single-walled carbon nanotubes. Kaniyoor et al. use a jetting inlet in their reactor. This jetting flow at the inlet of the reactor reduces the residence time of the precursors in the reactor before they decompose, and also decreases the residence time of released iron before thiophene begins to decompose and release sulphur. This phenomenon is shown in figure 7.5. For the parabolic inlet in the right figure, the ferrocene decomposes fully before the thiophene starts to decompose. The released iron has a residence time of the order of a second before sulphur starts to be

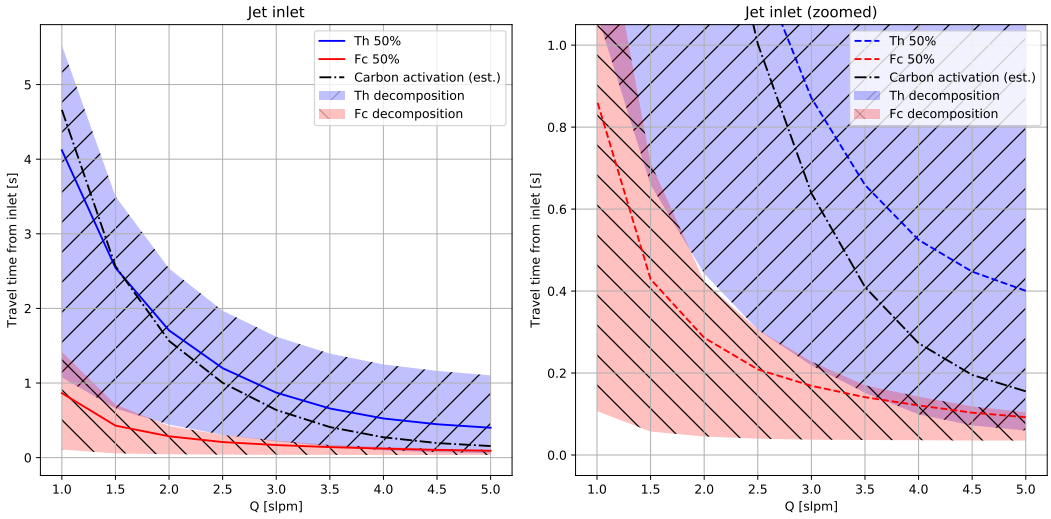


Figure 7.6 As for Figure 7.5 but at a linear scale on the vertical axis. The left figure shows the full plot from 0 s to 5 s travel time. The right figure shows a details plot of the region 0 s to 1 s travel time.

released. By contrast, for the high velocity jetting flow (left figure, above 3.0 L $\text{min}^{-1}$) thiophene begins to decompose and release sulphur before the ferrocene decomposes fully. Additionally, the iron that is released before the sulphur has a much shorter residence time until the sulphur is released (less than 0.1 s). This shorter residence time means that the particles produced do not grow as large as they would in a reactor with a parabolic inlet. The smaller particles produce single-walled nanoparticles, while large particles produce multi-walled nanoparticles. This explanation also agrees with the results of Lee et al. (2015), who found that earlier release of sulphur produces more single-walled carbon nanotubes.

# Part IV

# Particles

# 8 The particle model

To improve the Cambridge process of floating catalyst carbon nanotube production, we wish to know how the carbon nanotube aerogel is formed. To understand the aerogel formation we need to know how the particles in the reactor are created and grow. After developing a model of the precursors in the previous chapter, we now develop a particle model to simulate the particle creation and growth in the reactor.

We use the General Dynamic Equation (GDE) from Friedlander (2000, Chapter 11), (8.2), to simulate the evolution of the particles size distribution, $n = n(d_p, \boldsymbol{x}, t)$, inside the reactor. The particle size distribution is a function that describes the number of particles, of diameter $d_p$, that exist per unit volume, at location $\boldsymbol{x}$ at time $t$, and is defined as:

$$\frac{\partial n}{\partial t} + \boldsymbol{\nabla} \cdot (n\boldsymbol{u}) - \boldsymbol{\nabla} \cdot D\boldsymbol{\nabla} n = \left[\frac{\partial n}{\partial t}\right]_{\text{growth}} + \left[\frac{\partial n}{\partial t}\right]_{\text{coag}}, \tag{8.1}$$

$$= \left[\frac{\partial n}{\partial t}\right]_{\text{growth}} + \underbrace{\tfrac{1}{2}\int_0^{d_p} \beta(d'_p, d_p - d'_p) n(d'_p) n(d_p - d'_p)\, \mathrm{d}\left(d'_p\right)}_{\text{smaller particles coagulating to size } d_p}$$

$$- \underbrace{\int_0^{\infty} \beta(d_p, d'_p) n(d_p) n(d'_p)\, \mathrm{d}\left(d'_p\right)}_{\text{loss due to coagulation with other particles}}, \tag{8.2}$$

where $\boldsymbol{u}$ is the velocity of the carrier gas, $D$ is the particle diffusivity, which can be a function of the particle diameter $d_p$. The derivative $\frac{\partial I}{\partial d_p}$ is the rate at which particles grow in size. The first integral is the rate at which smaller particles, of sizes $(d_p - d'_p)$ and $d'_p$ collide and form a new particle of size $d_p$, while the second integral is the rate at which particles of size $d_p$ collide with other particles. $\beta(d_p, d'_p)$ is the collision rate between two particles of sizes $d_p$ and $d'_p$. In this expression we discount the term for the relative particle velocity due to an external field, $-\boldsymbol{\nabla} \cdot (\boldsymbol{c}n)$, because we have no external fields, the particles are small enough to neglect the effect of sedimentation due to gravity, and the motion due to thermophoresis is several orders of magnitude lower than the motion due to convection.

The particle growth rate term has contributions both from the nucleation of new particles, and from the condensation and evaporation of existing particles. Both the collision rate and the condensation-evaporation rate depend on the particle diameter. In particular, there are two size regimes that affect how the rates scale with particle diameter. For particle diameters smaller than the mean free path of the carrier gas the particles are said to be in the free-molecular regime, while for particle diameters larger than the mean free path of the carrier gas the particles are in the continuum regime.

The mean free path can be calculated by (Panda and Pratsinis, 1995):

$$\lambda = \frac{\mu}{\rho}\sqrt{\frac{\pi M_m}{2RT}}, \tag{8.3}$$

where $\rho$ is the density of the hydrogen carrier gas, $M_m$ is the molar mass of hydrogen, $\mu$ is the viscosity of hydrogen, $R$ is the universal gas constant, and $T$ is the temperature of the hydrogen gas. The mean free path of hydrogen in the reactor is shown in figure 8.1. The wall temperature of the reactor is included in the figure for comparison purposes.

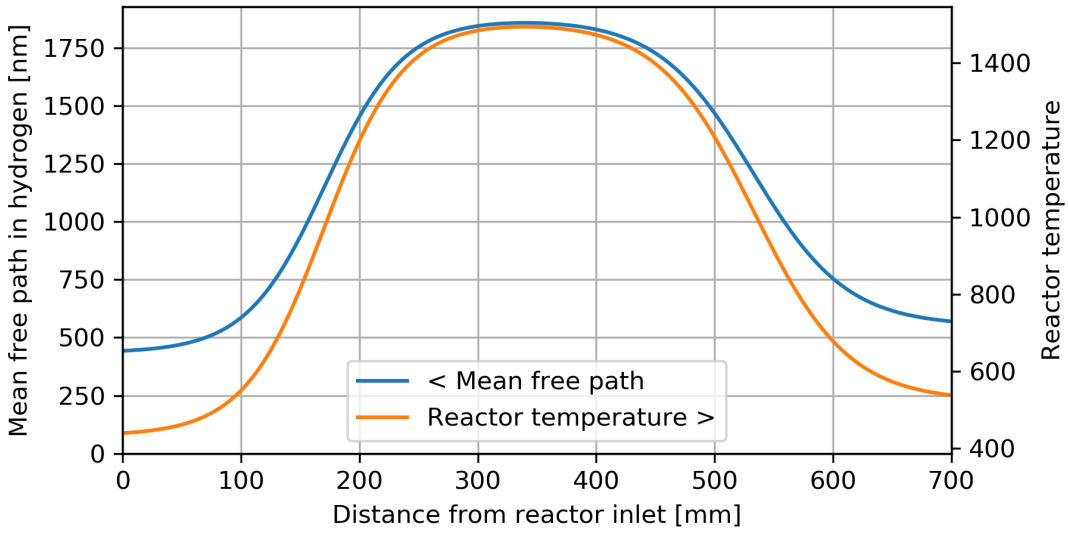


Figure 8.1 The mean free path of the hydrogen gas in the reactor. The orange line shows the wall temperature.

In the reactor the mean free path is always larger than 400 nm, which is an order of magnitude larger than the expected particle size in the reactor. The diameters of the vast majority of the measured particles in the reactor are smaller than the mean free path of the carrier gas, and therefore we assume that the model particles are always

in the free-molecular regime. This assumption simplifies the expressions for particle diffusion and coagulation.

## 8.1 Approximating a particle size distribution

It is not possible to work with a continuous particle size distribution computationally, instead we look at three different approaches of approximating the particle size distribution. Whitby and McMurry (1997, Table 1) provides a brief overview of the main approaches and their strengths and limitations. Based on that table we have looked at the three main approaches listed below.

### 8.1.1 Discrete particle size distributions

A discrete particle size distribution model approximates the shape of the particle size function. The approximating function may be piecewise constant (Gelbard et al., 1980), in which case the model is known as a *sectional* model. If the approximating function is piecewise linear the model is known as a *nodal* model (Mukherjee et al., 2006; Prakash et al., 2003). All discrete approaches require that a large number of variables are tracked, one per degree of freedom of the approximating function. This is computationally viable for a 1-dimensional model, where only $n$ degrees of freedom have to be computed and stored per iteration, where $n$ is the degrees of freedom of the approximating function. For a 2- or 3-dimensional the computational and memory requirements increase significantly, as $n$ degrees of freedom have to be computed and stored per grid point in the modelling domain. The computational cost of a discrete model is too great for our purposes, so we instead look at models that are less computationally expensive.

### 8.1.2 Method of Moments

To reduce the number of variables needed to track the particle size distribution, a method of moment approach can be employed (Phanse and Pratsinis, 1989; Pratsinis and Kim, 1989). The particle size distribution is approximated by taking several moments, typically 3, of the particle size distribution,

$$M_k = \int_0^\infty (d_p)^k n \, \mathrm{d}(d_p), \tag{8.4}$$

where $n$ is the particle size distribution; $M_k$ is the $k^{\text{th}}$ moment of the particle size distribution; and $d_p$ is the diameter of the particle. At least three moments need to be tracked to have a closed solution of the General Dynamic Equation (Pratsinis and Kim, 1989). This approach is used by Brown et al. (2008) to track the evolution of iron nanoparticles in their carbon nanotube reactor.

A method of moment approach is well suited to problems where there is a single peak in the particle size distribution, and the effects of condensation and evaporation are more influential than the particle growth dynamics. In these circumstances a set of closed-form equations can be easily derived. A set of closed-form equations is more difficult to derive when the effects of coagulation are significant. Including coagulation in the method of moments approach defies the main benefit – the mathematical simplicity of the model. This difficulty in modelling the coagulation of particles makes developing the adjoint equations very mathematically challenging. Therefore we choose to not use a method of moments, and instead use the simplest particle model.

### 8.1.3 Monodisperse particle distribution

The simplest approach of the three is to use a monodisperse particle distribution, where all particles at a point in space are assumed to be identical (Panda and Pratsinis, 1995). This model is used by Conroy et al. (2010) for their work on modelling the iron nanoparticles in the Cambridge Process, and by Kuwana and Saito (2005) in their work on a similar process used to produce carbon nanotubes.

In the monodisperse model, we assume that at any particular point, all the particles have the same size. To model the particle size we only require two variables: the number of particles per unit volume $N$, and the total volume of particles per unit volume $V$. From these values the monodisperse particle diameter can be calculated,

$$d_p = \left(\frac{6V}{\pi N}\right)^{1/3}. \tag{8.5}$$

This approach significantly simplifies the expressions for coagulation and diffusion, because only one particle size needs to be considered. This also simplifies the derivation of the adjoint equations.

## 8.2 Modelling the particles in the reactor

For our particle model, we extend the standard monodisperse particle model used by Kuwana and Saito (2005) and Panda and Pratsinis (1995). This standard model only simulates the particle coagulation process, and assumes that the decomposition of a ferrocene molecule creates an iron particle the size of one iron atom. It does not include the effects of nucleation, condensation, or evaporation. The temperature in the reactor increases in the middle, so we expect evaporation of particles to play a significant role. After the middle of the reactor the temperature drops again, and condensation has an impact on the particle sizes. Therefore we include the mass transfer between particles and the carrier gas due to evaporation and condensation.

The monodisperse particle model has two particle variables; the particle number density $M$, and the particle mass fraction $Y$; and one gas phase variable, the iron gas number density $g$. The particle number density $M$ represents the number of particles per unit mass of reactor gas. The particle mass fraction $Y$ represents the mass fraction of solid particles in the reactor gas, and the iron gas number density $g$ represents the number of gaseous iron atoms per unit mass of reactor gas.

In the particle modelling literature, the variables are typically expressed per unit volume. We express the variables per unit mass because this simplifies the governing equations when the convection and diffusion forces are included. The particle model variables can be easily converted to volume-based units by multiplying them by the reactor gas density $\rho$: $n = \rho g$, $N = \rho M$, $V = \rho Y/\rho_p$. The conversion from particle mass fraction $Y$ to particle volume fraction $V$ also divides the mass fraction by the particle density $\rho_p$.

The governing equations of the particles in the reactor are:

$$\rho\frac{\partial g}{\partial t} + \rho\boldsymbol{u}\cdot\boldsymbol{\nabla}g - \boldsymbol{\nabla}\cdot(\rho D\boldsymbol{\nabla}g) = \rho S - \rho(g^*I + E) \tag{8.6}$$

$$\rho\frac{\partial M}{\partial t} + \rho\boldsymbol{u}\cdot\boldsymbol{\nabla}M - \boldsymbol{\nabla}\cdot(\rho D_p\boldsymbol{\nabla}M) = \rho(I - C) \tag{8.7}$$

$$\rho\frac{\partial Y}{\partial t} + \rho\boldsymbol{u}\cdot\boldsymbol{\nabla}Y - \boldsymbol{\nabla}\cdot(\rho D_p\boldsymbol{\nabla}Y) = \rho m_1(g^*I + E) \tag{8.8}$$

where $\rho$ and $\boldsymbol{u}$ are the density and velocity of the carrier gas, $m_1$ is the mass of a single iron atom, $D$ is the gas diffusivity of iron atoms, $D_p$ is the diffusivity of the iron particles, $S$ is the iron gas source term, $I$ is the particle nucleation nucleation rate, $E$ is the mass

transfer from gas to particles due to condensation and evaporation, $C$ is the particle coagulation rate, and $g^*$ is the number of atoms of nucleated particles. We assume mass is conserved during particle coagulation, therefore the coagulation rate only affects the particle number density $M$. All terms are typically in units per volume in the literature, so we multiply all terms by $\rho$ to turn them into units per mass.

The iron gas source term $S$ is modelled as:

$$S \equiv ck = c \exp(\beta - T_a/T), \tag{8.9}$$

$$\rho \frac{\partial c}{\partial t} + \rho \boldsymbol{u} \cdot \boldsymbol{\nabla} c - \boldsymbol{\nabla} \cdot (\rho D_c \boldsymbol{\nabla} c) = -ck, \tag{8.10}$$

where $c$ is the ferrocene concentration, and $\beta, T_a$ are the decomposition parameters.

### 8.2.1 The nucleation rate

The particle nucleation rate $I$ is a function of the iron gas concentration $n$, iron gas saturation concentration $n_s = f(T)$, iron gas saturation ratio $S_r = n/n_s$, and nondimensional surface tension $\Theta = \mathrm{sa}_1 \sigma / kT$, where $\mathrm{sa}_1$ is the surface area of one iron atom, $\sigma$ is the surface tension of iron, $k$ is the Boltzmann constant, and $T$ is the temperature. We use the self-consistent kinetic model by Girshick and Chiu (1990),

$$I = n\, n_s \left( \frac{2\sigma}{\pi m_1} \right)^{\frac{1}{2}} \exp\left( \Theta - \frac{4\Theta}{27 \ln^2 S_r} \right). \tag{8.11}$$

The rate $I$ determines the number of new particles formed per second. Each newly formed particle consists of a minimally-stable number of atoms, modelled by the term $g^*$:

$$g^* = \left( \frac{2\Theta}{3 \ln S_r} \right)^3. \tag{8.12}$$

This nucleation size, $g^*$, depends on the saturation ratio $S_r$, which in turn depends on the iron gas concentration $n$. This dependency adds significant complexity to the derivation of the adjoint, while the value of $g^*$ does not vary strongly in the regions where the nucleation rate is significant. While testing our model we found that in the regions where nucleation is the dominant source of particles the value of $g^*$ is fairly constant at O(10). Therefore we treat the nucleation size as a uniform parameter for the

adjoint-based optimisation investigation, and avoid the added mathematical complexity of deriving the dependency of the nucleation size on the model variables, which would allow the nucleation size to be a function of reactor position.

### 8.2.2 The coagulation rate

When using the monodisperse particle distribution assumption we calculate the coagulation rate from first principles. Each particle is expected to collide with another particle at a rate of $\beta(d_p, d_p)N$ per unit time, where $N$ is the number of particles per unit volume and $\beta$ is the collision rate of two particles of diameter $d_p$. Summed up across all $N$ particles the coagulation rate per unit volume is:

$$C_{\text{vol}} = \tfrac{1}{2}\beta_{(d_p,d_p)}\ N^2, \tag{8.13}$$

where the factor of $\frac{1}{2}$ accounts for the double-counting of all particles.

The collision rate $\beta$ for the free-molecular regime is:

$$\beta(d_p, d_p) = 4\left(\frac{6kT}{\rho_p}d_p\right)^{1/2}, \tag{8.14}$$

where $\rho_p$ is the particle density.

Substituting in the expression for the collision rate, the coagulation rate is,

$$C_{\text{vol}} = 2\left(\frac{6kT}{\rho_p}d_p\right)^{1/2}\ N^2, \tag{8.15}$$

$$C_{\text{mass}} = 2\left(\frac{6kT}{\rho_p}d_p\right)^{1/2}\ \rho^2 M^2, \tag{8.16}$$

where (8.15) is the rate per unit volume and (8.16) is the rate per unit mass.

### 8.2.3 The condensation-evaporation rate

Once the total particle surface area grows sufficiently large through nucleation, the particle mass gain due to condensation becomes greater than the particle mass gain due to nucleation. In the reactor, this occurs upstream of the region of peak temperature. As the temperature in the reactor reaches the peak temperature, the particle mass loss

due to evaporation becomes becomes influential, and particle mass is lost as the particles evaporate.

The condensation-evaporation rate in the free-molecular regime depends on the collision rate between iron gas atoms and particles, and the oversaturation of the iron gas,

$$E = \beta(d_1, d_p)N(n - Kn_s), \tag{8.17}$$

where $\beta(d_1, d_p)$ is the collision rate between a particle of diameter $d_p$ and a iron gas atom, $N$ is the number of particles per unit volume, and $n - Kn_s$ is the oversaturation of the iron gas. $K$ is the Kelvin constant that further increases the effective iron gas saturation concentration $n_s$ due to the curvature of the particle. In practice this explains why smaller particles are more likely to evaporate than larger particles.

The collision rate between a particle and a gas atom $\beta(d_1, d_p)$ obeys:

$$\beta(d_1, d_p) = \left(\frac{RT}{2\pi M_m}\right)^{\frac{1}{2}} (\pi d_p^2), \tag{8.18}$$

where $R$ is the universal gas constant and $M_m$ is the molar mass of gaseous iron.

Substituting this expression for the collision rate into (8.17) gives:

$$E = \left(\frac{RT}{2\pi M_m}\right)^{\frac{1}{2}} \pi d_p^2 N(n - Kn_s), \tag{8.19}$$

where $\pi d_p^2 N$ is the total surface area of all particles. This can be rewritten as a volume term:

$$E = \left(\frac{RT}{2\pi M_m}\right)^{\frac{1}{2}} \frac{6V}{d_p}(n - Kn_s). \tag{8.20}$$

The calculated particle diameter $d_p$ is ill-defined at the points where both the particle volume fraction and number is 0. This occurs at the wall due to the boundary conditions, as well as in some regions of the flow due to the evaporation of the particles. We can avoid the numerical problems of an ill-defined $d_p$ by instead using a representative particle size $d_{p,0}$. The representative particle size is constant over the whole modelling domain, and ensures that the evaporation term remains bounded when the particle diameter $d_p = (6V/\pi N)^{1/3}$ decreases to a very small number.

Because the evaporation term only affects the particle volume $V$, and not the particle number $N$ we choose to use the volume-based expression (8.20) instead of the particle number-based expression. This makes the governing equation implicit rather than explicit and improves the numerical stability. This forces us to use the representative particle size $d_{p,0}$ to avoid further numerical issues as the volume decreases.

We further rewrite the expression for the condensation-evaporation rate to use the units per mass instead of units per volume:

$$E = \left(\frac{RT}{2\pi M_m}\right)^{\frac{1}{2}} \frac{6\rho Y}{\rho_p d_p}(\rho g - K n_s). \tag{8.21}$$

The representative particle size is passed to the model as a parameter and its value is assimilated from the experimental data during the optimisation process.

The Kelvin effect $K$ in (8.20) is modelled as:

$$K = \exp\left(\frac{4\sigma M_m}{d_p \rho_p RT}\right), \tag{8.22}$$

where $\sigma$ is the surface tension of iron, and the other variables are as stated above.

The value of $K$ is very sensitive to changes in $d_p$, and the value of $d_p$ in the model is very sensitive to changes in $K$. To avoid the numerical instabilities this tight co-dependency creates we choose a constant and uniform value of $K$ for the model, to approximate the effect of evaporation in the hot zone. The value of $K$ is a variable in the optimisation and is assimilated from the data.

### 8.2.4 The particle diffusivity

The diffusivity of particles depends on the size regime. For the free-molecular regime the particle diffusivity is modelled by (Panda and Pratsinis, 1995),

$$D_p = \frac{kT}{3\pi\mu}\left(\frac{1}{d_p} + \frac{3.314\ \lambda}{d_p^2}\right), \tag{8.23}$$

where $\mu$ is the kinematic viscosity of the carrier gas, and $\lambda$ is the mean free path of hydrogen.

The diffusivity varies inversely with the particle size. At very small particle sizes the diffusivity is high, while at large particle size the diffusivity is low. At low diffusivities, the finite element method experiences numerical problems, and particle mass is no longer conserved. To avoid this problem we do not use the theoretical calculation in (8.23), but instead prescribe the diffusivity over the modelling domain. For the prescribed diffusivity field we have a region of high diffusivity close to the inlet, where we expect particles to be small. Further downstream the prescribed field has a region of low diffusivity, as the particles increase in size, down to a minimum value for the diffusivity to ensure the numerical computation still conserves mass. We define the prescribed diffusivity $\hat{D}_p$ as,

$$\hat{D}_p = \chi \hat{D}_1 + (1-\chi)\hat{D}_0 \left(\frac{T}{T_0}\right)^{1.6}, \tag{8.24}$$

$$\chi \equiv \frac{1}{1+\exp\left(\frac{z-z_0}{0.01L}\right)}, \tag{8.25}$$

where $z_0 = (0.2 + 0.05\ Q)/1.5$ is the approximate location of the small to large particle transition point, $\hat{D}_1 = 4 \times 10^{-4}$ is the large particle diffusivity, $\hat{D}_0 = 4 \times 10^{-7}$ is the small particle diffusivity which is affected by the reactor temperature, $T_0$ is the reactor reference temperature at 800 °C, used to scale the diffusivity with reactor temperature, and $L$ is the length of the reactor, 700 mm.

Figure 8.2 shows how the prescribed particle diffusivity, $\hat{D}_p$ (orange line), compares with the theoretical particle diffusivity from (8.23), $D_p$ (blue line). In the small-particle regime, before particle growth becomes significant at a distance of 200 mm from the reactor inlet, the theoretical and prescribed diffusivity agree well. The curves diverge only in the large-particle regime, at a distance of 400 mm from the inlet, which is after the peak temperature zone. At this point the particles grow sufficently large that diffusivity becomes negligible, less than $10 \times 10^{-6}\,\mathrm{m^2\,s^{-1}}$, and the prescribed diffusivity we use is larger, in order to maintain the stability of the computational model.

### 8.2.5 The iron gas saturation concentration

The iron gas saturation concentration $n_s$ is a significant term in the nucleation rate (8.11) and condensation-evaporation rate (8.20). The saturation concentration of iron gas atoms depends on the saturation pressure of iron gas, which varies with gas temperature. The saturation pressure is modelled with an empirical expression from Haynes

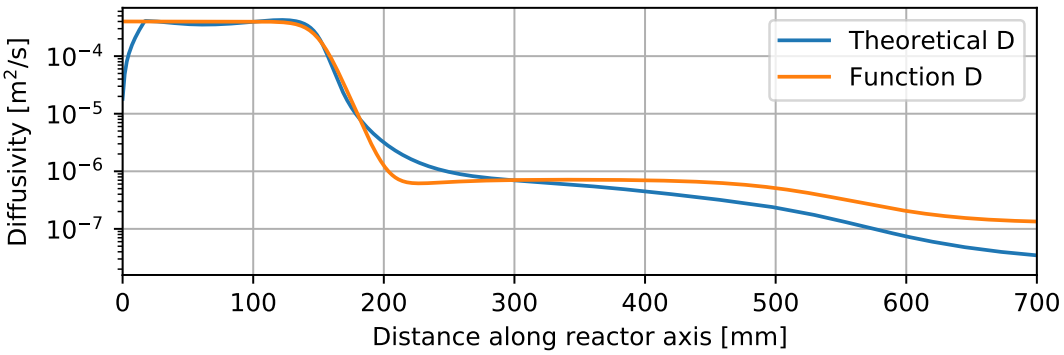


Figure 8.2 The particle diffusivity, theoretical estimate calculated from the model solution in blue, and the approximation function $\hat{D}_p$ in orange.

(2014):

$$\log_{10} P_s = 12.106 - 21\,723/T + 0.4536 \log_{10} T - 0.5896/T^3, \tag{8.26}$$

where $T$ is the temperature in K, $P_s$ is the saturation pressure in Pa. Figure 8.3 shows the saturation pressure of iron in the reactor as a function of distance from the reactor inlet. The saturation pressure is then converted to saturation concentration using the ideal gas law,

$$n_s = P_s N_A / RT, \tag{8.27}$$

where $N_A$ is Avogadro's constant.

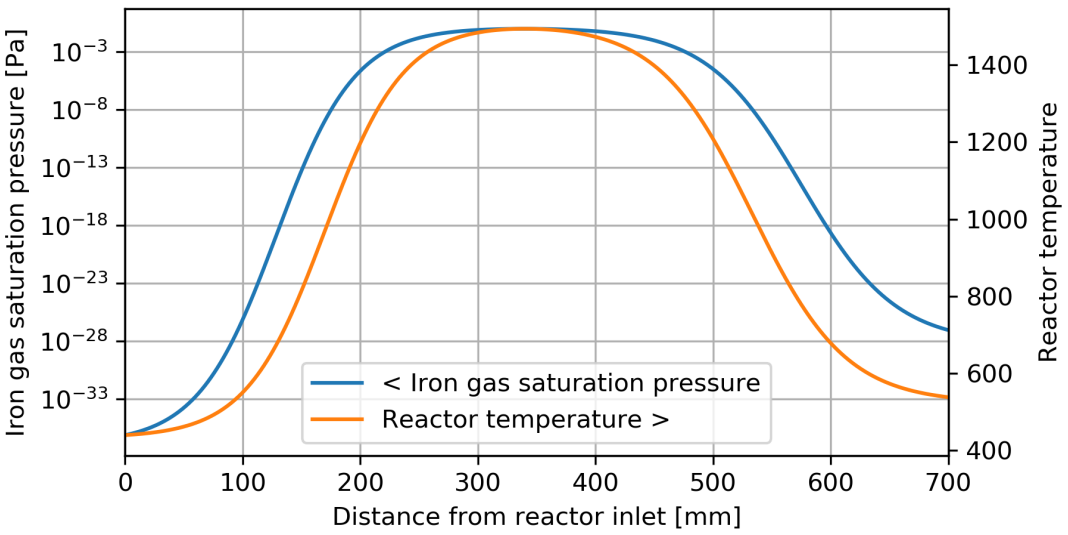


Figure 8.3 The saturation pressure of iron in the reactor. The orange line shows the wall temperature.

# 9 Modelling the nanoparticles in the reactor

This work first appeared in *Gökstorp, F. K. A. and Juniper, M. P. (2020). Flow Simulations Including Iron Nanoparticle Nucleation, Growth and Evaporation for Floating Catalyst CNT Production.* Catalysts*, 10(12):1383.*

We use our particle model described in chapter 8 to investigate the effect of flowrate, temperature, and ferrocene mass fraction on the production of catalyst nanoparticles. This work does not include optimisation, and we instead manually vary the input parameters. We use a fixed particle model and vary the reactor flowrate and the ferrocene mass fraction. We set the particle model parameters to $d_{p,0} = 10\,\text{nm}$ which is of the order of the expected particle sizes, $K = 2$ to model the evaporation found in the middle of the reactor, but not higher to avoid numerical problems as all the particle mass evaporates. The nucleation size $g^*$ was calculated at each point in the modelling domain, based on the local temperature and saturation ratio according to equation (8.12). The ferrocene decomposition rate was set at the best fit values found in chapter 6. These values give good agreement with the experimental data for a reactor peak temperature of 1250 °C.

We perform three sets of simulations. In each set, only one input parameter is varied. In the first set, we vary the flowrate from $0.5\,\text{L}\,\text{min}^{-1}$ to $2.0\,\text{L}\,\text{min}^{-1}$ with a peak temperature of 1250 °C and 0.5 mass% ferrocene mass fraction (Hoecker et al., 2016). For the second set, we keep the flowrate at $1.0\,\text{L}\,\text{min}^{-1}$ and vary the peak temperature from 1150 °C to 1300 °C, also with a ferrocene mass fraction of 0.5 mass%. For the third set we keep the flowrate fixed at $1.0\,\text{L}\,\text{min}^{-1}$, and the peak temperature fixed at 1250 °C, while we vary the ferrocene mass fraction from 0.5 mass% to 2.0 mass%.

For each simulation we generate the base flow velocity ($\boldsymbol{u}$), temperature ($T$), and density ($\rho$); as well as the iron vapour mass fraction ($g$), iron particle mass fraction ($Y$) and iron particle number density ($M$). We also calculate the particle diameter ($d_p$) from $Y$ and $M$. The particle number density depends heavily on the specific nucleation expression

used, and has a significantly higher uncertainty than the particle mass fraction result. Therefore we use the particle mass fraction to compare with experimental results.

## 9.1 Model comparison

We compare our numerical results with the experimental results from Hoecker et al. (2016). In their study, Hoecker *et al.* measure the particle mass concentration as a function of distance from the reactor inlet, with the reactor peak temperature at the same values as ours (1150 °C to 1300 °C), and a flowrate of 0.5 L min$^{-1}$. The temperature profile used is the profile shown in figure 1.3 scaled to the appropriate peak temperature. Figure 9.1 shows our numerical results (solid lines) compared with the experimental results (red dots) for different peak temperatures. For 1250 °C peak temperature, our model results match the experimental results well. The 1300 °C case also matches the experimental results well, with a slight overprediction of the peak mass fraction. The lower temperature cases, 1150 °C and 1200 °C, are only qualitatively correct.

## 9.2 Results

In all our simulations, the ferrocene decomposes and releases iron vapour about 200 mm downstream from the reactor inlet. Figure 9.2 shows how this distance varies with flowrate and peak temperature. Figure 9.3 ($a$) plots the resulting rapid increase of the saturation ratio to very high orders of magnitude as iron vapour is released by the ferrocene decomposition. The extremely high saturation ratio, of the order of $10^{15}$, drives rapid nucleation and particle growth. Figure 9.3($b$) shows the difference between the mass fraction of iron vapour, and the saturation amount. The difference peaks at 200 mm, after which there is enough particle surface area for condensation to dominate further iron release from the decomposition of ferrocene.

The peak in the particle mass fraction appears at a distance of 250 mm from the reactor inlet, increasing slightly for higher flowrates. The particle nucleation and growth appears first close to the wall, where the convection velocity is lower, and therefore the residence time is higher. The increased residence time gives particles a longer time to grow before they enter the hot zone, situated from 300 mm to 400 mm downstream from the inlet. In the hot zone, the high temperature increases the saturation pressure of the carrier gas, and the particles start to evaporate. Some of the evaporated iron vapour condenses

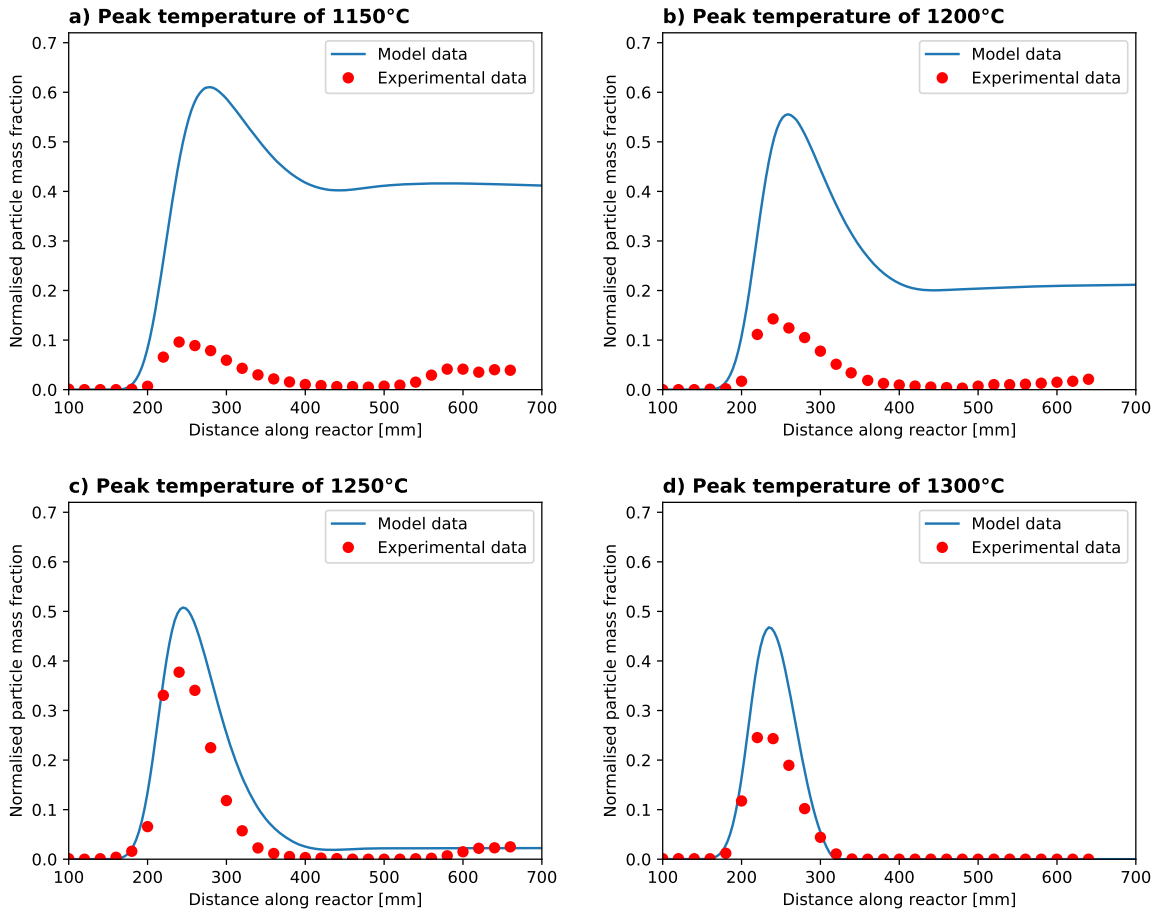


Figure 9.1 Model data (blue line) compared to experimental measurements by Hoecker et al. (2016) (red circles). The model and experiments use a flowrate of 0.5 L min$^{-1}$ and ferrocene mass fraction of 0.5 mass%. The flow in (*a*) has a peak temperature of 1150 °C, in (*b*) has a peak temperature of 1200 °C, in (*c*) has a peak temperature of 1250 °C, and in (*d*) has a peak temperature of 1300 °C.

on the reactor walls, decreasing the overall mass of iron in the reactor. Lower flowrates lead to a longer residence time in the hot zone and therefore lead to more iron vapour condensing on the reactor wall. Figure 9.4 plots the particle mass fraction and particle number within the reactor. At $0.5\,\mathrm{L\,min^{-1}}$, particle mass is rapidly lost to the wall once the flow enters the hot zone at 300 mm. Beyond 400 mm the temperature drops, the particles stop evaporating, and the particle mass fraction stabilises. The particles continue to grow slightly as the flow cools and iron vapour condenses onto the particles. At these conditions, roughly 400 mm to 500 mm downstream of the inlet, the carbon nanotubes grow, align, and bundle, and form an aerogel.

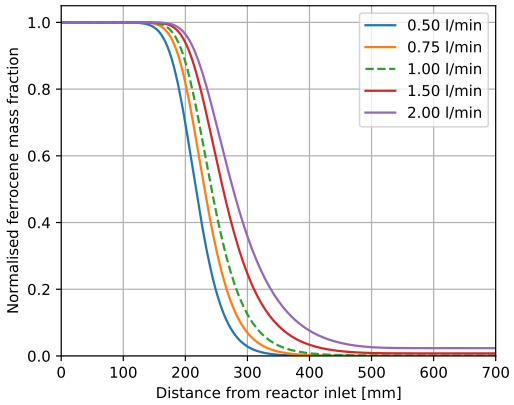


Figure 9.2 Plot of the decomposition of ferrocene as a function of distance from the inlet, normalised by the ferrocene mass fraction at the inlet. Each line corresponds to a different flowrate.

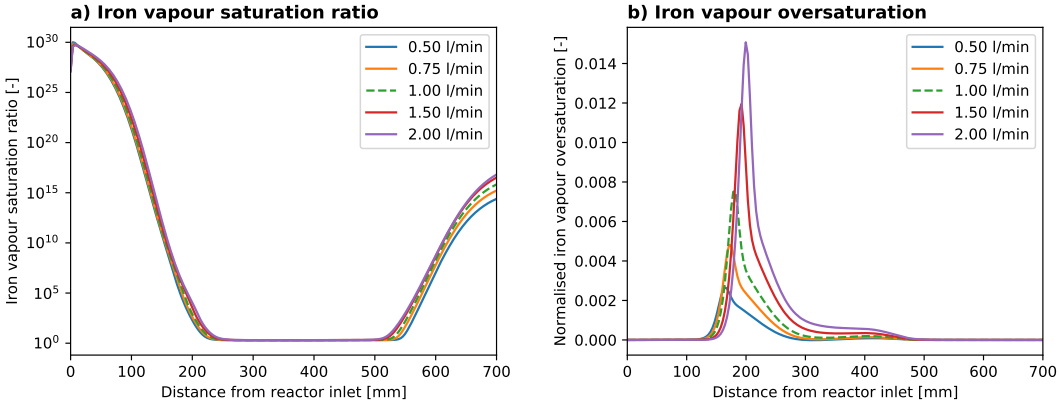


Figure 9.3 Plots of the $(a)$ iron vapour saturation ratio $S = g/g_s^*$ and $(b)$ iron vapour oversaturation $\Delta g = g - g_s^*$, as a function of distance from the reactor inlet, for different flowrates.

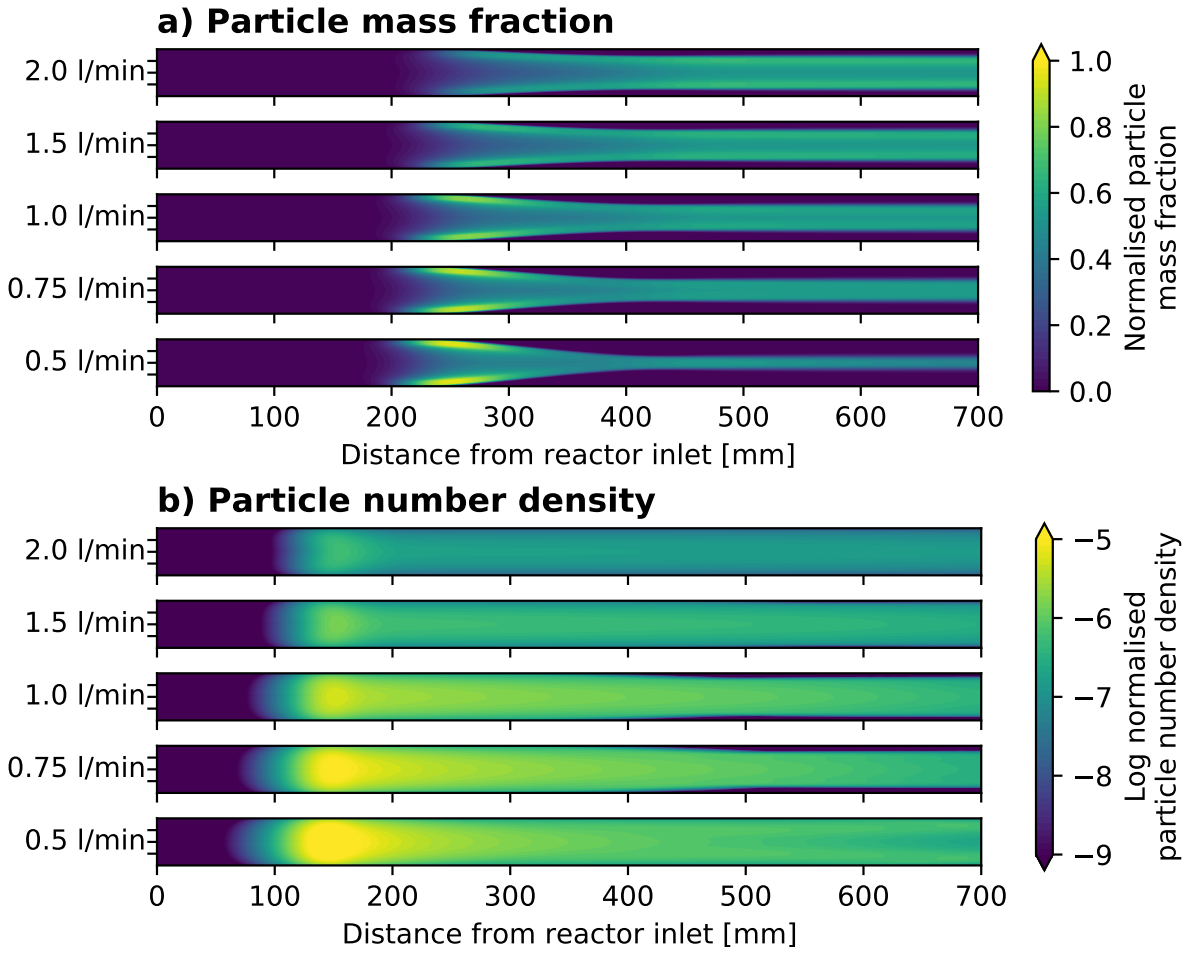


Figure 9.4 Plots of (*a*) normalised particle mass fraction and (*b*) normalised particle number density, for different inlet flowrates, at a peak temperature of 1250 °C and a ferrocene mass fraction of 0.5 mass%. Nucleation starts at about 200 mm from the inlet, and the main evaporation zone is between 300 mm to 400 mm.

Figure 9.5 (*a*) and (*b*) shows the radial profile of particle mass fraction and how it varies as a function of the input parameters. The dashed green line shows the common reference case of $1\,\mathrm{L\,min^{-1}}$, 1250 °C, and 0.5 mass% ferrocene. At low flowrates ($0.5\,\mathrm{L\,min^{-1}}$) or low ferrocene mass fractions (0.25 mass%) most of the particle mass is found very close the the centreline. Additionally, at low flowrates the iron particles have a longer residence time in the hot zone, and more iron vapour is able to evaporate and diffuse to the wall. Therefore, only the particles that are furthest from the wall survive the hot zone, and the particle mass is concentrated on the centreline. At low ferrocene mass fraction there is less particle mass, so a shorter residence time in the hot zone is required for the same evaporation, therefore the mass is also concentrated at the centreline for low ferrocene mass fractions, even at normal flowrates ($1\,\mathrm{L\,min^{-1}}$). At higher flowrates and higher ferrocene mass fractions, the peak particle mass is found some distance away from the centreline. The distance of the peak from the centreline increases with increasing flowrates and increasing ferrocene mass fraction. As the particles closer to the wall evaporate first in the hot zone, reducing the residence time leads to reduced mass loss from the particles close to the wall, and therefore the particle mass fraction peak shifts towards the wall. The same effect is seen as the ferrocene mass fraction increases. As particles have larger mass, it takes a longer time for them to evaporate and therefore more particles close to the wall survive the hot zone, moving the mass fraction peak towards the wall.

Figure 9.5 (*c*) and (*d*) shows the axial profile of the radially-averaged particle mass fraction and how it varies as a function of the input parameters. Increased ferrocene mass fraction uniformly increases the particle mass fraction profile, while increasing flowrate reduces the mass particle fraction before the hot zone and increases it after the hot zone. This suggests that at higher flowrates the particle nucleation and growth is stretched out over a longer region, therefore leading to a lower peak.

The effect of the process parameters on the particle diameter is similar to that on the particle mass fraction. Figure 9.6 (*a*) and (*b*) plots the radial profiles of particle diameter, at 500 mm from the reactor inlet. At low flowrates ($0.5\,\mathrm{L\,min^{-1}}$) or low ferrocene mass fractions (0.25 mass%), the peak of the particle diameter is located at the centreline. As flowrate and ferrocene mass fraction increase, however, the peak of the particle diameter moves away from the centreline. Increasing the flowrate significantly increases the particle diameter. This is because higher flowrates reduce the time the iron vapour spends in conditions favourable to nucleation, so fewer particles are formed. Instead,

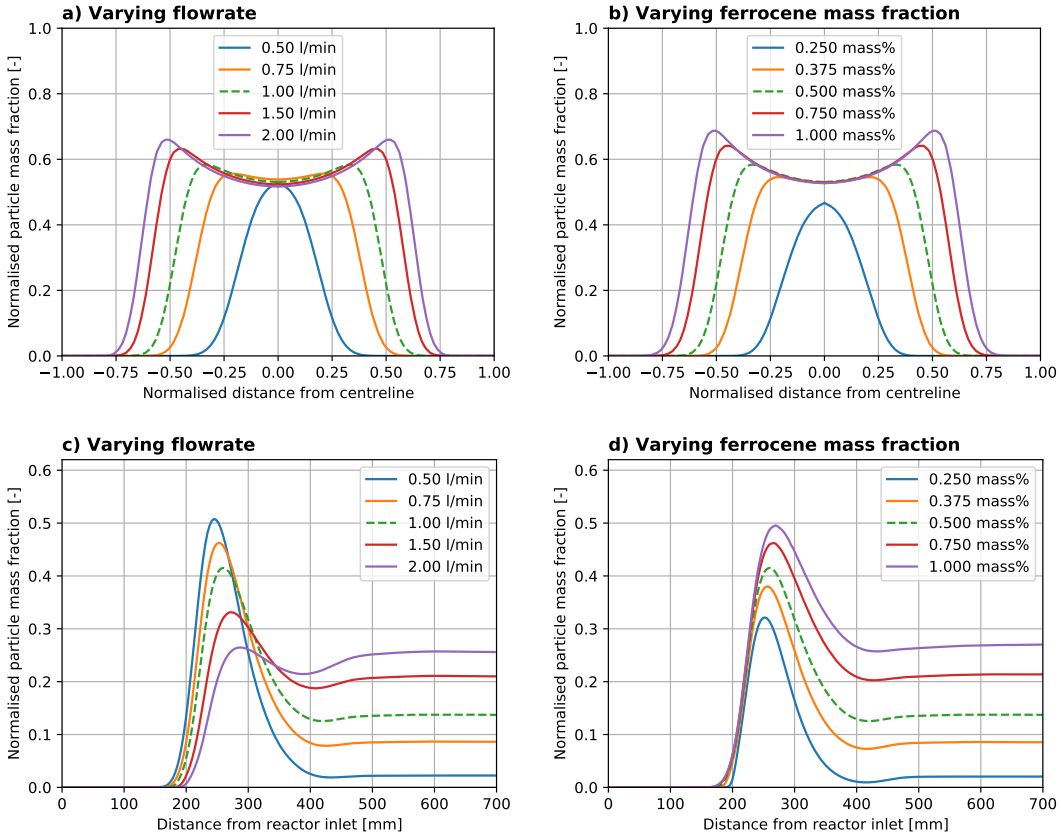


Figure 9.5 Plots of the normalised particle mass fraction. (*a*) and (*b*) plot the radial profile of the particle mass fraction, 500 mm downstream from the inlet. (*c*) and (*d*) plot the axial profile of the particle mass fraction, averaged over the reactor radius. (*a*) and (*c*) show the variations with flow rate (at 1250 °C peak temperature and 0.5 mass% ferrocene mass fraction). (*b*) and (*d*) show the variations with input iron mass (at 1 L min$^{-1}$ and 1250 °C peak temperature).

the iron vapour condenses on the existing particles, increasing the particle diameter. Increasing the flowrate also reduces the time spent in the hot evaporation zone, therefore reducing the mass evaporated from the particles and subsequently lost to the wall, and leaving larger particles. Increasing the ferrocene mass fraction also increases particle diameter, because there is more iron mass in the system to form particles, and therefore the particles coagulate faster, to larger sizes, during their residence in the reactor.

Figure 9.6 (*c*) and (*d*) shows the axial profile of the radially-averaged particle diameter. The particle diameter peaks at 250 mm just at the start of the hot zone, decreases during the hot zone until 400 mm at which point it starts growing again. After 400 mm the particle growth is mainly due to coagulation, as particle mass fraction is constant. Increasing the flowrate has only a small effect on the particle diameter as flowrate is increased from $0.5\,\mathrm{L\,min^{-1}}$ to $1.0\,\mathrm{L\,min^{-1}}$. At higher flowrates ($1.5\,\mathrm{L\,min^{-1}}$ and $2.0\,\mathrm{L\,min^{-1}}$), the particle diameter is much larger despite the reduced time for particles to coagulate. This happens because fewer particles nucleate and therefore the released iron vapour condenses onto fewer particles, making the average particle larger. Increasing the ferrocene mass fraction instead reduces the particle diameter peak before the hot zone, again because fewer particles are nucleated and instead the existing particles grow due to condensation. The particle diameter after the hot zone increases with increasing ferrocene mass fraction, as more mass remains in the reactor after the hot zone and therefore particles can grow larger. More ferrocene also produces more particles through nucleation, therefore there is more rapid size growth due to coagulation after the hot zone.

Figure 9.7 (*a*) and (*b*) plots the total particle surface area (sum of the surface area of all the particles in the reactor, per kg of carrier gas) as a function of radius, at 500 mm from the reactor inlet. At low flowrates or low ferrocene mass fractions ($0.5\,\mathrm{L\,min^{-1}}$ and 0.25 mass% respectively) the total surface area is concentrated around the centreline. At higher flowrates or higher ferrocene mass fractions, the radial profile forms a plateau instead of a distinct peak away from the centreline. Figure 9.7 (*c*) and (*d*) plots the radially-averaged total particle surface area over the reactor length. Increasing ferrocene mass fractions increases the total surface area in the reactor, both at the peak before the hot zone, and in the CNT growth region after the hot zone. Increasing the flowrate reduces the total surface area before the hot zone, and increases it slightly after the hot zone. At very high flowrates ($2\,\mathrm{L\,min^{-1}}$) the total surface area after the hot zone is lower

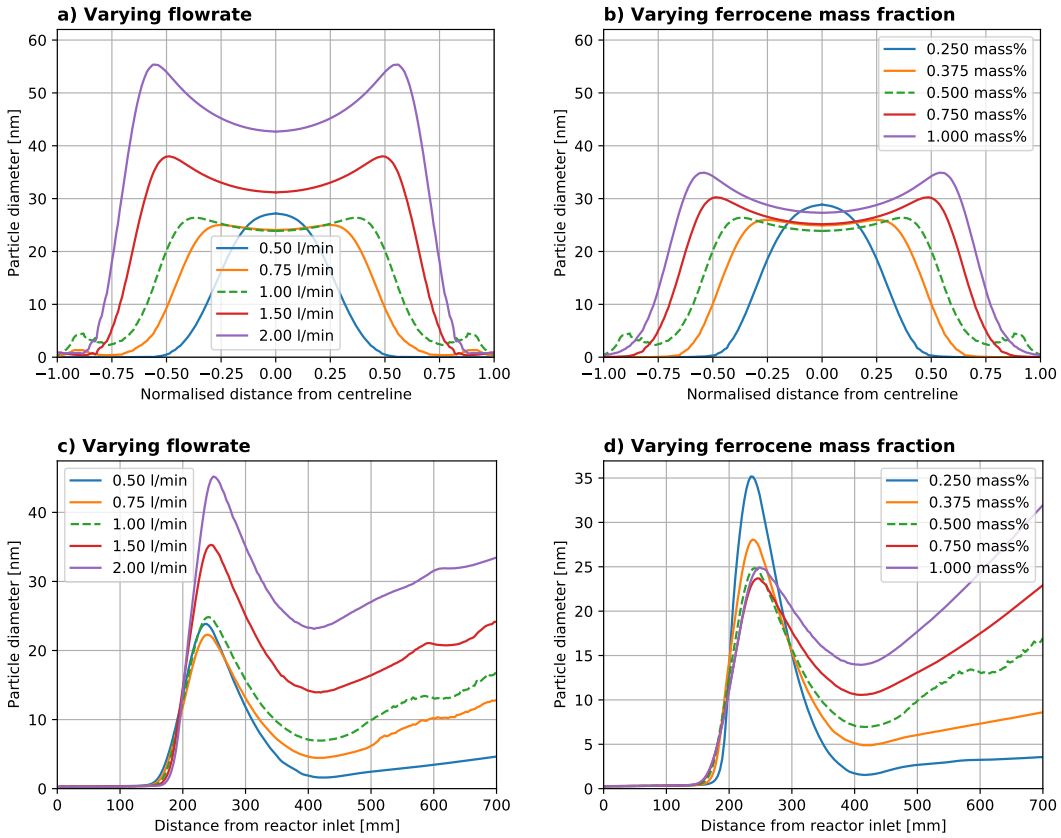


Figure 9.6 Average particle diameter in the reactor. (*a*) and (*b*) plot the radial particle diameter profile, 500 mm downstream from the inlet. (*c*) and (*d*) plot the axial profile, averaged over the reactor radius. (*a*) and (*c*) plot the variations with flowrate (at 1250 °C peak temperature and 0.5 mass% ferrocene). (*b*) and (*d*) plot the variations with input iron mass (at 1 L min$^{-1}$ and 1250 °C peak temperature).

than for the other cases. This is because fewer particles are formed, and therefore the total surface area is lower, despite the particle mass fraction being higher.

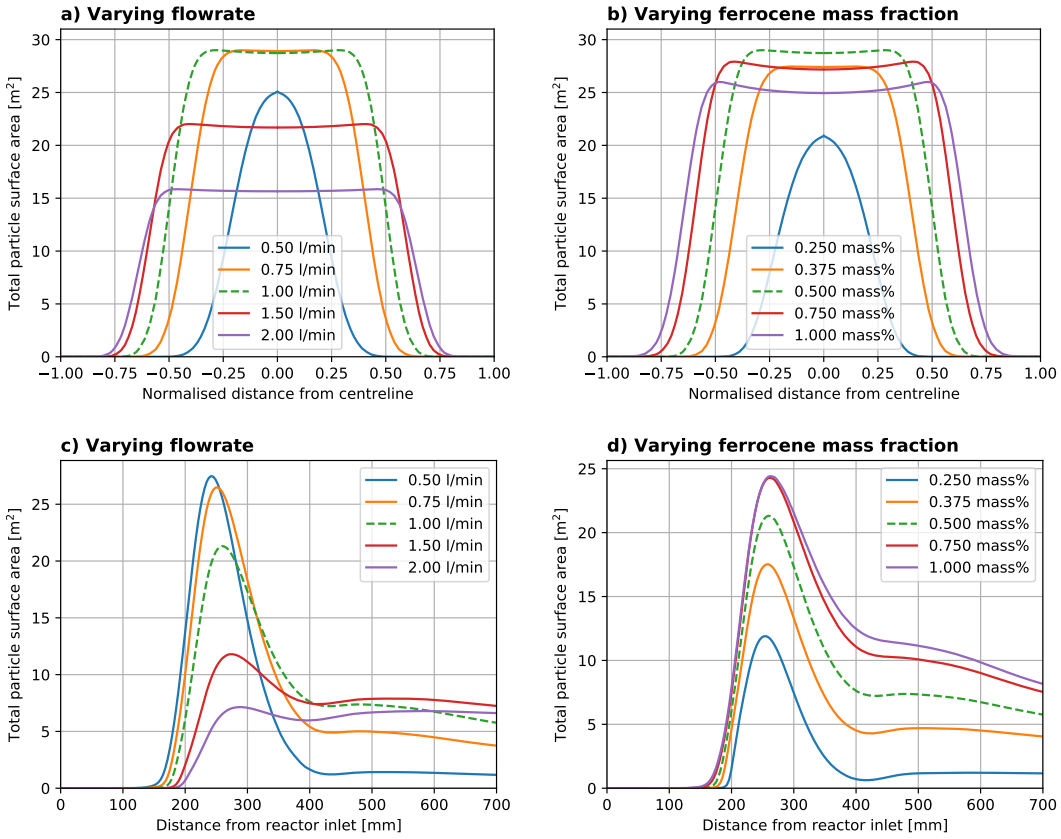


Figure 9.7 Total particle surface area in the reactor, assuming a monodisperse size distribution. (*a*) and (*b*) plot the radial profile, 500 mm downstream from the inlet. (*c*) and (*d*) plot the axial profile, averaged over the radius. (*a*) and (*c*) shows the variations with flowrate (at 1250 °C peak temperature and 0.5 mass% ferrocene mass fraction). (*b*) and (*d*) shows the variations with input iron mass (at 1 L min$^{-1}$ and 1250 °C peak temperature).

## 9.3 The tendency of the aerogel to form a sock

As reported by many different sources, Conroy et al. (2010); Hoecker et al. (2016); Li et al. (2004); Motta et al. (2007a), the CNTs aggregate into a hollow and flexible tube (a sock) towards the end of the reactor. Hou et al. (2017) found that increased iron mass is correlated with increased CNT production rate. Except for at low flowrates or low ferrocene mass fractions, the iron particle peaks are found a distance away from the centreline. The fluid velocity is lower closer to the wall, which increases the residence

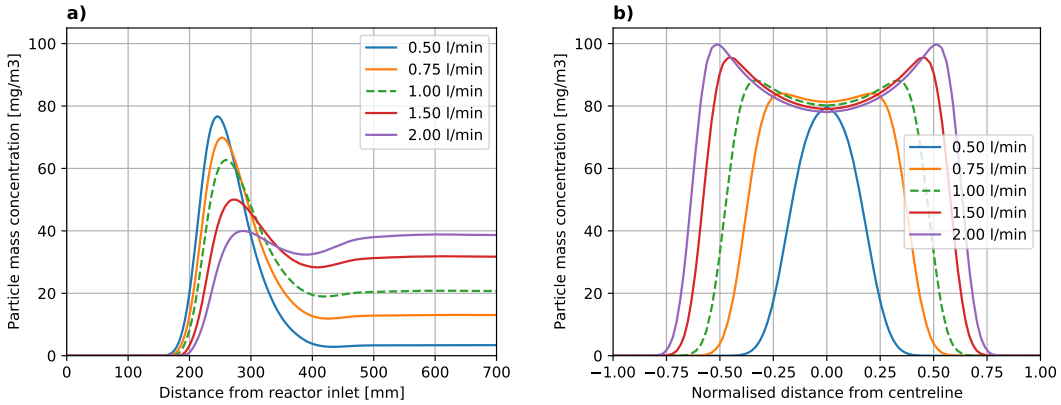


Figure 9.8 Plots of the dimensional mass concentration ($a$) over the length of the reactor and ($b$) as a radial slice 500 mm downstream of the reactor, each line corresponds to a different flowrate.

time. Higher residence times means particles grow larger due to more condensation and coagulation occurring. However, particles also diffuse and if the particles collide with the wall they stick and the mass is lost from the flow. Close to the wall the diffusion dominates and the particle mass fraction is very low. Slightly further away from the wall, the residence time is still high, particles grow larger, and more mass condenses onto the particles. At the centreline there is still significant particle mass, but because the residence time is lower the particle mass fraction is also lower. Therefore, the particle mass fraction peaks are found a distance away from the centreline, and this distance varies with the reactor flowrate.

Hoecker et al. (2017b) found that there is a critical particle mass concentration required for the production of spinnable CNTs of 110 mg m$^{-3}$ to 160 mg m$^{-3}$. Figure 9.8 shows the dimensional mass concentration estimated using the model, ($a$) shows the radially-averaged mass concentration evolution over the length of the reactor, while ($b$) shows the radial profile of mass concentration at 500 mm downstream from the reactor inlet. For all flowrates, the radial averaged values are below the minimum mass concentration, however, for the higher flowrates (1.5 and 2.0 L min$^{-1}$), the mass concentration peak is very close to the minimum mass concentration of 110 mg m$^{-3}$. As the iron particle mass peaks are found a distance away from the centreline, CNTs are more likely to be produced in these regions. At the centreline, the mass concentration is around 80 mg m$^{-3}$, significantly below the minimum particle mass concentration, so no CNTs are produced there.

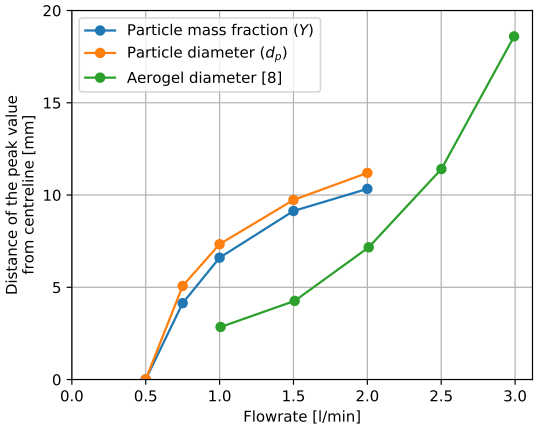


Figure 9.9 Radial location of the peak values of particle mass fraction and particle diameter as a function of flowrate, at a peak temperature of 1250 °C and ferrocene mass fraction of 0.5 mass%. The experimentally measured aerogel diameter from Conroy et al. (2010) are included as the green line. The aerogel measurements are for a reactor with a larger diameter and a process that uses a different ferrocene mass fraction.

As most CNTs are produced in an annulus, the resulting aerogel is hollow as observed in experiments. Figure 9.9 plots the radial location of the peaks of the particle mass fraction and particle diameter as a function of flowrate, along experimental results from Conroy et al. (2010). The shift of the peak of the particle mass fraction towards the wall as flowrate increases agrees qualitatively with the experimental observations. As our model does not include the dynamics of the aerogel itself, or the effect of its winding speed, we do not expect the results to match quantitatively.

## 9.4 Conclusions of the investigation

In this study we develop a model capable of simulating the nucleation, growth, and evaporation of catalyst nanoparticles in a reactor for the production of carbon nanotubes. We looked at three different measurements of the particles: i) particle mass fraction, ii) average particle diameter, and iii) total particle surface area. We found that varying the flowrate or the ferrocene mass fraction entering the reactor has the most significant effect on the measurements in two different regions: the region before the hot zone (150 mm to 300 mm), and the region after the hot zone (400 mm to 700 mm). As the flowrate through the reactor increases, the particle mass fraction found in the region after the hot zone increases, while the particle mass fraction in the region before the hot zone decreases. With increasing ferrocene mass fractions, the particle mass fraction increases

over in both zones. For the particle diameter, increasing flowrate from $0.5\,\mathrm{L\,min^{-1}}$ to $1.0\,\mathrm{L\,min^{-1}}$ increases the diameter only in the region after the hot zone, while increasing the flowrate further from $1.0\,\mathrm{L\,min^{-1}}$ to $2.0\,\mathrm{L\,min^{-1}}$ increases the particle diameter in both regions. The total particle surface area sees an decrease in the region before the hot zone as flowrate increases, while the value in the region after the hot zone is does not change strongly with flowrates above $0.5\,\mathrm{L\,min^{-1}}$. As ferrocene mass fraction increases, the total surface area increases in both zones.

At low flowrate or low ferrocene mass fraction, the particle mass fraction is concentrated at the centreline of the reactor. The profile of particle diameter is also highest at the centreline for those conditions. As flowrate in the reactor increases, the peaks of the particle mass fraction, and the particle diameter, move away from the centreline. The same effect occurs for increasing ferrocene mass fraction. This displacement away from the centreline of the mass fraction peak explains why the CNTs form a hollow sock-like aerogel at the downstream end of the reactor.

With further experimental data, our model can be made more predictive, as we show in chapter 10. The model can also be extended to model the growth of the CNTs. Further numerical studies on different reactor geometries will also help to explore what process parameters are critical for the production of the nanoparticles that produce CNTs. The effects of sulphur on the nucleation process could also be explored by including an additional modelling term. This would help us understand what role the sulphur could have on the nucleation of the nanoparticles, and why sulphur is so critical in the FC-CVD process.

# 10 Fitting the particle model to experimental data

The model used in chapter 9 can qualitatively model the behaviour of particles in the reactor. In order to obtain more quantitative results from the model, we need to fit the model's parameters to a set of experimental observations. Once the parameters are fitted we can try to extrapolate from the results and make more predictions on what will affect the particle growth. Once the particle model is calibrated we can estimate what effect any changes in flow rate, reactor temperature, reactor length, flow characteristics, and even reactor shape, might have on the production of the nanoparticles. Additionally, understanding where the nanoparticles nucleate and grow allows us to further understand under what conditions the carbon nanotubes best grow.

## 10.1 The experimental data

To fit the models we use data from Hoecker et al. (2016). To collect the data, a thin aluminium probe is inserted into the flow from the outlet of the reactor, with the probe inlet at the location where the measurement is to be taken. A sample of the gas is extracted through the probe and enters a scanning mobility particle sizer (SMPS), in order to count and size the particles found in the flow. We integrate the particle number data by the particle size, in order to obtain the total particle volume at the measurement location. We assume that the particles contain a negligible mass of elements other than iron, and we therefore calculate the particle mass by multiplying the particle volume by the density of iron ($7800\,\mathrm{kg\,m^{-3}}$).

Figure 10.1 shows the data collected by Hoecker et al. (2016). The vertical axis shows the particle mass concentration, and the horizontal axis shows distance from the inlet of the measurement. The four different curves show the measurements at four different reactor peak temperatures, from $1150\,^{\circ}\mathrm{C}$ to $1300\,^{\circ}\mathrm{C}$. All four measurement sets were taken with a flow rate of $0.5\,\mathrm{L\,min^{-1}}$.

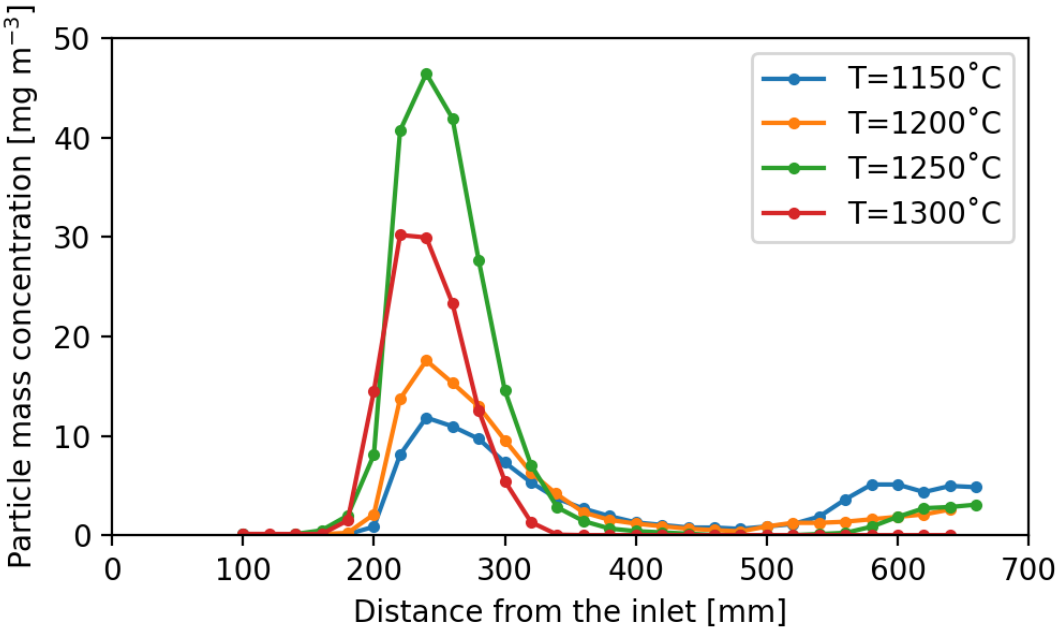


Figure 10.1 The experimental observations of particle mass concentration measured at different distances from the reactor inlet, at four different reactor temperatures, 1150–1300 °C. All measurements are for a flow rate of 0.5 L min$^{-1}$.

To use the data in the simulation and optimisation code we nondimensionalise the mass concentration by the mass of iron that enters the reactor per unit volume in the form of ferrocene. Figure 10.2 shows the experimental data after being scaled by the input iron mass.

## 10.2 Optimising the particle model

We compare the particle model and the experimental observations, in order to construct an objective function which we can use to evaluate the marginal likelihood of the model. We follow the process for optimising the model of the ferrocene decomposition, in chapter 6, and assume that all distributions are Gaussian. We first define the objective function, then we derive the adjoint governing equations that allow us to construct the expression for the gradient of the objective function with respect to the model's parameters.

The objective function is the negative log of the posterior probability of the model parameters. By Bayes' theorem, the negative log posterior is equivalent to the sum of the negative log of the modelling parameter prior distribution and the negative log of

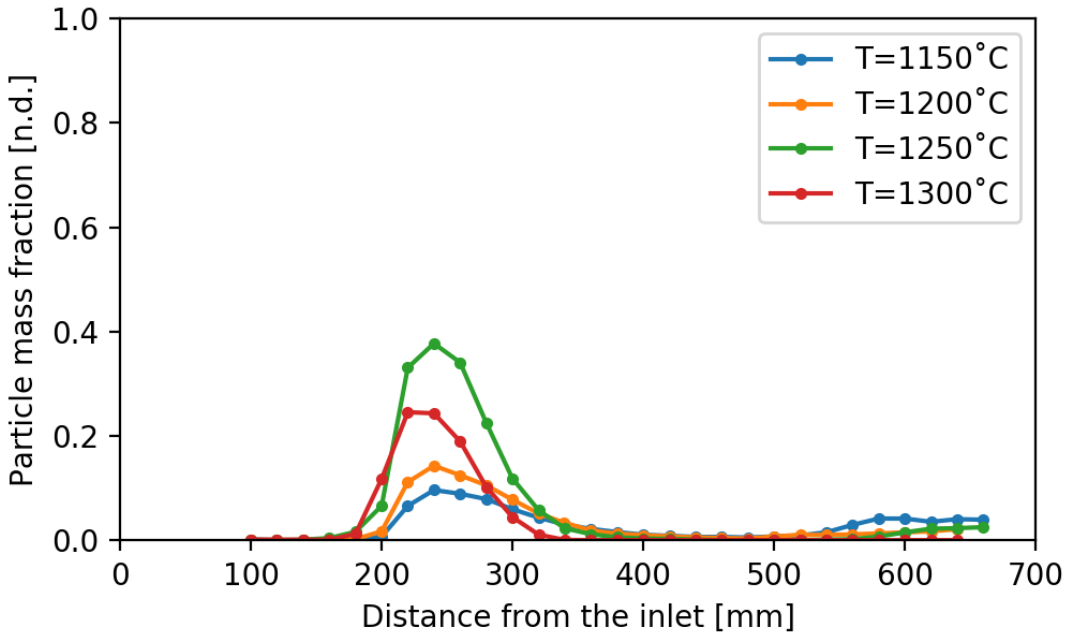


Figure 10.2 The scaled experimental data compatible with the code.

the parameter likelihood:

$$J(\boldsymbol{\theta}, \boldsymbol{x}) = -\log P(\boldsymbol{\theta} \mid \boldsymbol{x}, H) \tag{10.1}$$

$$= \underbrace{\tfrac{1}{2}(\boldsymbol{\theta} - \boldsymbol{\mu}_{\boldsymbol{\theta}})^{\top} \boldsymbol{\Sigma}_{\boldsymbol{\theta}}^{-1} (\boldsymbol{\theta} - \boldsymbol{\mu}_{\boldsymbol{\theta}})}_{-\log P(\boldsymbol{\theta}|H)} + \underbrace{\tfrac{1}{2}\left(\boldsymbol{q}(\boldsymbol{s}) - \boldsymbol{x}\right)^{\top} \boldsymbol{\Sigma}_{\boldsymbol{x}}^{-1} \left(\boldsymbol{q}(\boldsymbol{s}) - \boldsymbol{x}\right)}_{-\log P(\boldsymbol{x}|\boldsymbol{\theta},M)}$$

$$+ \text{constants}, \tag{10.2}$$

where $\boldsymbol{x}$ is the experimental observation vector, $\boldsymbol{q}(\boldsymbol{s})$ is the model prediction vector, $\boldsymbol{\mu}_{\boldsymbol{\theta}}$ is the parameter prior, $\boldsymbol{\Sigma}_{\boldsymbol{\theta}}^{-1}$ is the parameter certainty matrix, $\boldsymbol{\Sigma}_{\boldsymbol{x}}^{-1}$ is the experimental observation certainty matrix, and the constants are the terms that do not depend on $\boldsymbol{x}$, $\boldsymbol{s}$, or $\boldsymbol{\theta}$. The negative log of the parameter likelihood measures the discrepancy between the model predictions and the experimental measurements, while the negative log of the parameter prior measures the discrepancy between the model parameter values and what we expect the model parameter values to be.

The experimental observations are particle mass fraction measurements taken at the centreline of the reactor, at different distances from the reactor inlet. For each experimental observation, $x_i$, we produce a compatible modelling prediction, $q_i(\boldsymbol{s})$, by integrating the particle mass fraction field, $Y$, over a radial slice of area $2\pi R^2$, at the same measurement

depth $z = z_i$:

$$q_i(\boldsymbol{s}) = \frac{1}{2\pi R^2} \int Y|_{z=z_i} \, \mathrm{d}A. \tag{10.3}$$

We use the governing equations of the direct model from chapter 8 to find the model state $\boldsymbol{s} = (g, M, Y, c)$. The measurements were taken once the system reached a steady state, therefore the particle model contains no unsteady terms:

$$\rho \boldsymbol{u} \cdot \boldsymbol{\nabla} g - \boldsymbol{\nabla} \cdot (\rho D \boldsymbol{\nabla} g) - \rho S + \rho(g^* I + E) = 0, \tag{10.4}$$

$$\rho \boldsymbol{u} \cdot \boldsymbol{\nabla} M - \boldsymbol{\nabla} \cdot (\rho D_p \boldsymbol{\nabla} M) - \rho(I - C) = 0, \tag{10.5}$$

$$\rho \boldsymbol{u} \cdot \boldsymbol{\nabla} Y - \boldsymbol{\nabla} \cdot (\rho D_p \boldsymbol{\nabla} Y) - \rho m_1(g^* I + E) = 0. \tag{10.6}$$

We also include the governing equation for a model of the decomposition of ferrocene, which enables us to calculate how the decomposition parameters affects the particle model directly through the iron gas source term $S \equiv ck$:

$$\rho \boldsymbol{u} \cdot \boldsymbol{\nabla} c - \boldsymbol{\nabla} \cdot (\rho D_c \boldsymbol{\nabla} c) + \rho c k = 0. \tag{10.7}$$

The governing equations describe the evolution of the model's four variables: the iron gas mass density, $g$, the particle number density, $M$, the particle mass fraction, $Y$, and the ferrocene molecule number density, $c$. The model contains five parameters, where $\beta$ and $T_a$ determine the decomposition of ferrocene, defined in chapter 6, and $d_{p,0}$, $K$, and $g^*$ determine the particle dynamics, defined in chapter 8. We minimise this objective function, $J$, with a gradient-based optimisation process to find the parameters that best describe the experimental data.

The adjoint governing equations and boundary conditions are derived in appendix B. The expression for the gradient of the objective function is:

$$\frac{\partial J}{\partial \beta} = (\beta - \mu_\beta)\sigma_\beta + \int_V \rho c \left(g^\dagger + c^\dagger\right) k \, \mathrm{d}V, \tag{10.8}$$

$$\frac{\partial J}{\partial T_a} = (T_a - \mu_{T_a})\sigma_{T_a} + \int_V -\rho c \left(g^\dagger + c^\dagger\right) k/T \, \mathrm{d}V, \tag{10.9}$$

$$\frac{\partial J}{\partial g^*} = (g^* - \mu_{g^*})\sigma_{g^*} + \int_V \rho I g^\dagger - \rho I M^\dagger - \rho I Y^\dagger \, \mathrm{d}V, \tag{10.10}$$

$$\frac{\partial J}{\partial K} = (K - \mu_K)\sigma_K + \int_V \rho m_1 E_0 n_s Y^\dagger - \rho E_0 n_s g^\dagger \, \mathrm{d}V, \tag{10.11}$$

$$\begin{aligned}\frac{\partial J}{\partial d_{p,0}} = {} & (d_{p,0} - \mu_{d_{p,0}})\sigma_{d_{p,0}} + \int_V \rho (E_0/d_{p,0})(\rho g - K n_s) \left[m_1 Y^\dagger - g^\dagger\right] \mathrm{d}V \\ & + \int_V -\rho (C_0/2d_{p,0}) M^2 M^\dagger \, \mathrm{d}V,\end{aligned} \tag{10.12}$$

where $\mu$ is the parameter prior mean, $\sigma$ is the parameter prior standard deviation, and all terms with a dagger superscript ($\dagger$) are adjoint variables.

For this problem we only develop the first-order adjoint in order to save time on both the derivation and implementation. However the second-order adjoint could be derived using the same process we used to derive the second-order adjoint for the precursor decomposition in section 6.2.3.

We test and validate the optimisation process and this gradient expression by assimilating test data generated with a known ground truth.

## 10.3 The optimisation process

We test the developed first-order gradients using the same approach we used to test the optimisation process in section 6.3. First we generate a model solution using know parameters, listed in the first column in table 10.1. We add Gaussian noise with a mean of 0 and a standard deviation of 0.03 to this ground truth solution to create the synthetic observations. The results are the blue circles in figure 10.3.

We choose a prior that we know is some distance from the ground truth, shown in figure 10.3 as the green dotted line. The corresponding parameters are listed in table 10.1.

Table 10.1 Comparison of synthetic parameter and fitted model's parameters for optimisation validation. The first parameter is most influential, while p1 and p2 do not greatly affect the output of the model.

| | | **Ground truth** | **Prior** | **Posterior** |
|---|---|---|---|---|
| $p_0$ | $K$ | 3.0 | 1.2 | 2.4 |
| $p_1$ | $d_{p,0}$ | $80.0 \times 10^{-9}$ | $40.0 \times 10^{-9}$ | $44.9 \times 10^{-9}$ |
| $p_2$ | $g^*$ | 80.0 | 40.0 | 39.3 |
| $p_3$ | $\beta$ | 32.236 | 8.087 | 9.858 |
| $p_4$ | $T_a$ | $30 \times 10^3$ | $11 \times 10^3$ | $8.96 \times 10^3$ |

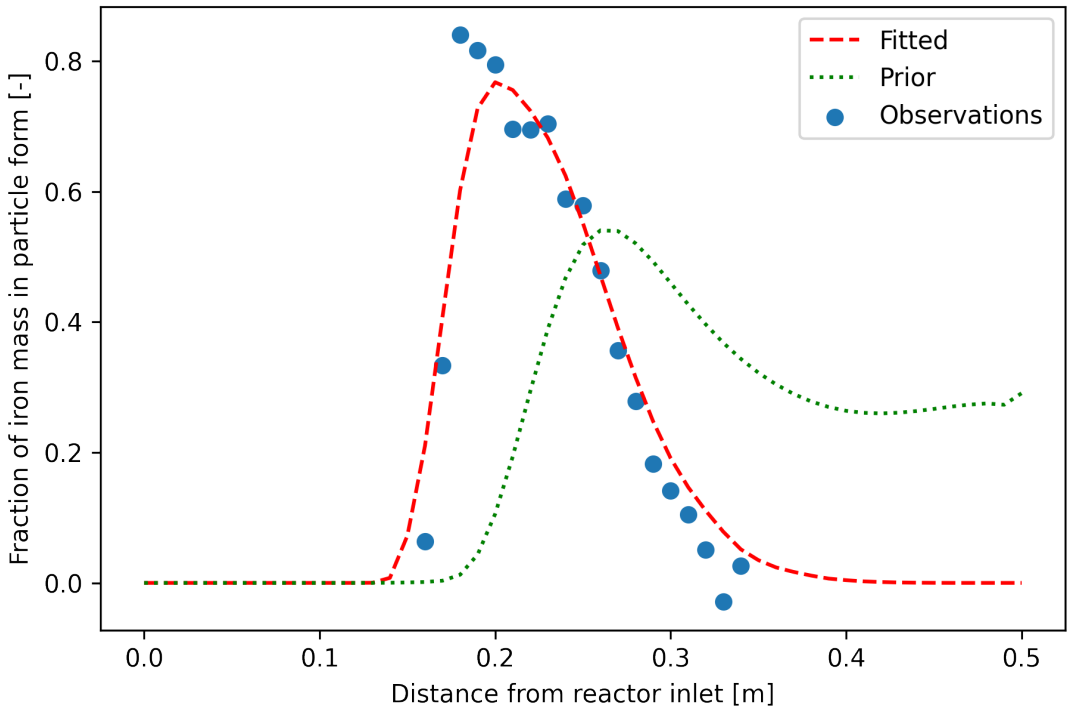


Figure 10.3 We test the optimisation process by fitting the model to noisy synthetic data.

The posterior fit is presented as the red dashed line in figure 10.3, with the parameters also listed in table 10.1. The optimisation process found a posterior parameter set that agrees well with the observation data, even though many parameter values are closer to the prior distribution than the ground truth values. Only the parameter for the Kelvin effect $K$ is closer to the ground truth than the prior value. This term determines how fast the particle mass evaporates in the heated region of the reactor, and therefore governs the loss of particle mass after a distance of about 0.2 m downstream in the reactor. The next term, $d_{p,0}$, affects the particle coagulation rate and also the condensation-evaporation rate. The impact of this term is less than that of $K$, based on the fact that the posterior value has not increased significantly from the prior value. The nucleation size parameter $g^*$ has changed the least of all five parameters, suggesting it has the least impact on the model results and is therefore weakly observable. The nucleation size parameter only affects the nucleation rate, and the effect of a variation of the nucleation size is very small compared to the several orders of magnitude the nucleation rate varies over the length of the reactor. The last two parameters govern the decomposition rate of the ferrocene, and determine when, and how quickly, the iron gas is released. These two parameters are coupled by the temperature of the reactor. They appear in the expression for decomposition rate as $k = \exp(\beta - T_a/T)$. This means that, for the same representative temperature $T$, there are pairs of $(\beta, T_a)$ that produce the same decomposition rate $k$.

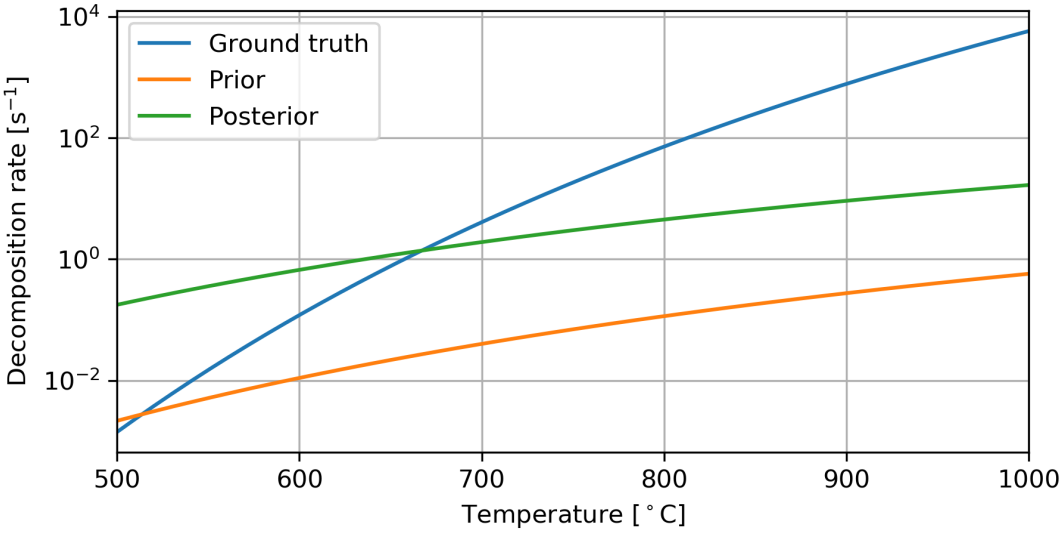


Figure 10.4 Comparison of the decomposition rates for the three different parameters sets in table 10.1.

## 10.4 Results

For the optimisation with experimental data we use a different prior, as shown in table 10.2. We use expected values for the Kelvin constant, representative particle diameter and nucleation size $(K, d_{p,0}, g^*)$ based on the expected size of the nanoparticles. The prior for the ferrocene decomposition was set to the literature value used by Kuwana and Saito (2005). We are unsure whether or not these prior values are close to the true parameters, so we use a large uncertainty in the prior distribution.

Using this prior we perform two separate optimisations: one where the initial parameters are set to the prior values, and one where the initial parameters are set to an alternative initial guess using the thiophene rate of decomposition calculated in chapter 6. This alternative initial guess is also listed in table 10.2. For the second run the same prior is used for the Bayesian penalty term; only the start point of the optimisation is different.

Table 10.2 The parameter prior and the initial guess used for the two optimisation runs using experimental observations.

| | | **Prior** | **Alternative initial guess** |
|---|---|---|---|
| $p_0$ | $K$ | 2.0 | 2.0 |
| $p_1$ | $d_{p,0}$ | $10.0 \times 10^{-9}$ | $10.0 \times 10^{-9}$ |
| $p_2$ | $g^*$ | 40.0 | 40.0 |
| $p_3$ | $\beta$ | 26.12 | 9.35 |
| $p_4$ | $T_a$ | 32 473 | 12 851 |

There are four sets of data, each characterised by the peak reactor temperature. Each set is assimilated independently. This indicates whether the parameters are universal for the different temperatures or whether there is an additional temperature dependence that the model is unable to fully describe.

The results of the optimisation are compared to the experimental observations, and the prediction of the prior in figure 10.5. The expected values of the posterior distribution of the parameters are shown in table 10.3. From all figures it is clear that starting from the prior does not result in good agreement with the observations. The model consistently predicts larger mass fractions peaks at 250 mm from the inlet. This is both an indication that the starting parameters are far from the true values, and also that the optimisation process is stuck a local optimum.

Table 10.3 The optimised parameters starting from the mean of the prior.

| | **Prior** | 1150 °C | 1200 °C | 1250 °C | 1300 °C |
|---|---|---|---|---|---|
| $K$ | 2.00 | 5.00 | 4.10 | 2.73 | 2.00 |
| $d_{p,0}$ | $10.00 \times 10^{-9}$ | $7.60 \times 10^{-9}$ | $6.63 \times 10^{-9}$ | $10.00 \times 10^{-9}$ | $10.00 \times 10^{-9}$ |
| $g^*$ | 40.00 | 39.41 | 39.85 | 39.99 | 40.00 |
| $\beta$ | 26.12 | 25.15 | 26.48 | 26.05 | 26.12 |
| $T_a$ | 32 473 | 31 041 | 32 121 | 32 436 | 32 473 |

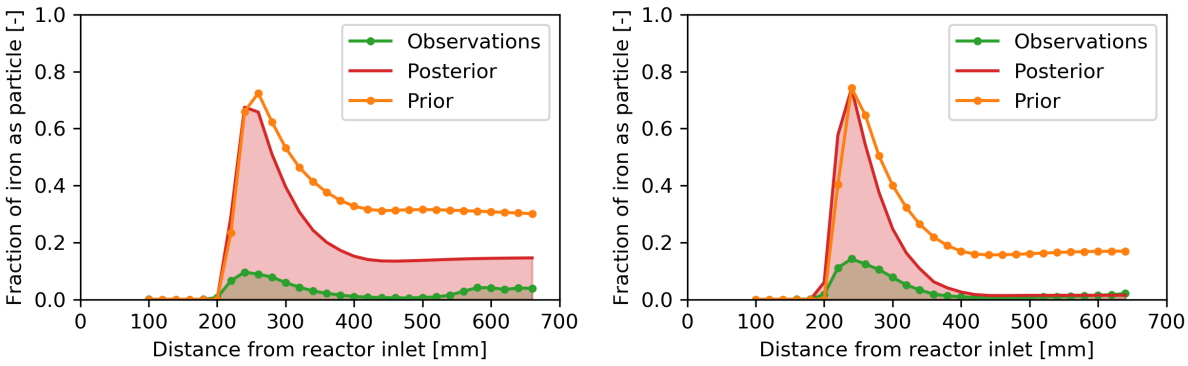


(a) Peak temperature of 1150 °C

(b) Peak temperature of 1200 °C

(c) Peak temperature of 1250 °C

(d) Peak temperature of 1300 °C

Figure 10.5 Plot of the experimental observation of the particle mass (green), the prediction using the prior (orange) and the prediction using the fitted posterior (red), starting from the prior.

Table 10.4 The optimised parameters starting from the alternate start.

| | **Start** | 1150 °C | 1200 °C | 1250 °C | 1300 °C |
|---|---|---|---|---|---|
| $K$ | 2.00 | 3.54 | 3.04 | 2.52 | 2.91 |
| $d_{p,0}$ | $10.00 \times 10^{-9}$ | $9.67 \times 10^{-9}$ | $9.67 \times 10^{-9}$ | $10.00 \times 10^{-9}$ | $10.00 \times 10^{-9}$ |
| $g^*$ | 40.00 | 38.07 | 38.07 | 41.70 | 42.30 |
| $\beta$ | 26.12 | 10.17 | 10.17 | 10.25 | 10.52 |
| $T_a$ | 32 473 | 10 932 | 10 932 | 14 531 | 15 131 |

In contrast, the optimisation run from the alternative initial guess, using the thiophene decomposition parameters instead of the ferrocene parameters, produces a good fit for the high temperature cases of peak reactor temperature of 1250 °C and 1300 °C. The peak of the mass fraction is captured well, and the general shape of the mass fraction curve over the length of the reactor agrees well with the experimental results. For the low temperature cases of 1150 °C and 1200 °C reactor peak temperature, the agreement with experimental results is poor.

The variance in the fitted parameters also indicates which parameters are of high importance to the model. In both the optimisation starting at the mean of the prior, and the alternative initial guess, the nucleation size $g^*$ did not significantly change. Additionally, the representative particle size, $d_{p,0}$, only changed for the low temperature optimisation runs (1150 °C and 1200 °C) starting from the mean of the prior. For the other optimisation runs the representative particle size remained close to the initial value of $10.0 \times 10^{-9}$. This shows that the impact on the model of both the representative particle size, $d_{p,0}$, and the nucleation size, $g^*$, is small compared to the other three parameters. The representative particle size affects the coagulation rate, and the condensation rate. However, the Kelvin factor, $K$, affects the condensation rate more strongly than the representative particle size. The nucleation size affects the nucleation rate linearly. The low variation of this parameter for the different optimisation cases means that the impact of this parameter on the nucleation rate is negligible compared to the other terms. In addition to the nucleation size, $g^*$, the nucleation rate depends nonlinearly on the saturation ratio of the iron gas. Therefore the nucleation size parameter does not strongly influence the modelling results or the results of the optimisation.

In addition to the representative particle size, $d_{p,0}$, the Kelvin factor, $K$, affects the condensation and evaporation rate of the particles. The Kelvin factor changed significantly for all except one optimisation run: it remained at 2.0 for the case with a peak reactor

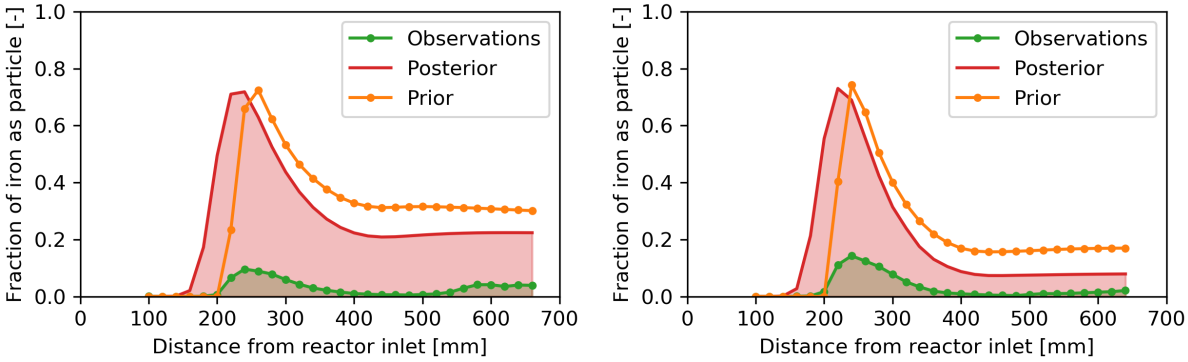


(a) Peak temperature of 1150 °C




(b) Peak temperature of 1200 °C

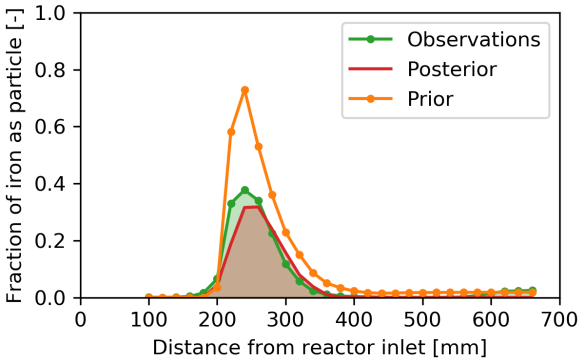


(c) Peak temperature of 1250 °C

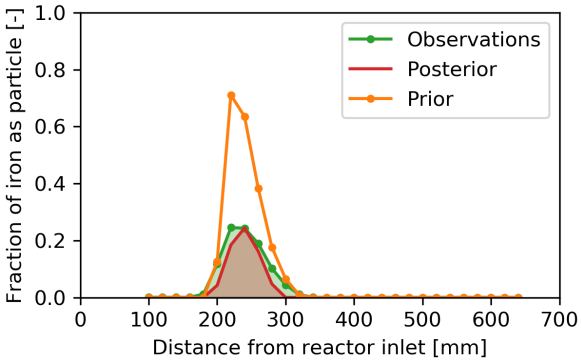


(d) Peak temperature of 1300 °C

Figure 10.6 Plot of the experimental observation of the particle mass (green), the prediction using the prior (orange) and the prediction using the fitted posterior (red), starting from the alternate initial guess.

temperature of 1300 °C that started from the expected value of the prior. A large value of the Kelvin factor promotes evaporation of the particles. The particles evaporate once the reactor temperature reaches the peak temperature, at a distance of about 250 mm downstream from the inlet. The iron gas produced when the particles evaporate condenses onto the wall of the reactor and is removed from the fluid flow, reducing the total iron mass in the flow. This evaporation effect is clearly present in all four experimental observation sets, and the Kelvin factor is the most significant parameter that models the evaporation rate.

The remaining two parameters are the decomposition parameters of the iron precursor. In this model, the formation of the iron particles depends solely on the amount of iron gas released by the modelled precursor. This precursor is either modelled with the decomposition rate of ferrocene, as was done for the optimisations using the mean of the prior as a starting point, or with the decomposition rate of thiophene, as was done for the optimisations using the alternate initial guess as a starting point. In practice, the interplay between iron and sulphur to produce the catalyst nanoparticles is unclear (see chapter 7 for more discussion on this topic). The results of the optimisation shows that using the current model, the decomposition rate of thiophene predicts the experimental observations at higher reactor peak temperatures (1250 °C and 1300 °C) significantly better than the decomposition rate of ferrocene does. Additionally, reactor peak temperatures of 1250 °C to 1300 °C are more commonly used in the Cambridge process (Hoecker et al., 2016; Kaniyoor et al., 2019; Weller et al., 2019), therefore a model that is only predictive at these temperature ranges is still useful.

# Part V

# Conclusions

# 11 Conclusions and future work

In this thesis the dynamics of the Cambridge process (Li et al., 2004) is investigated. Part I explains the Cambridge process for carbon nanotube production and introduces the geometry of the reactor used. Optimisation in a Bayesian framework is described, and the fundamentals of using adjoints to derive the gradient of an objective function is presented.

In part II the Low Mach-number flow model used for the majority of the work is introduced. A simpler, uniform density, Navier–Stokes model is used to simulate the flow of the gas valve attached to the end of the reactor, and three different geometries of the gas valve are investigated with different flow rates and internal baffle sizes. The performance of each gas valve configuration is evaluated with the conflicting aims of maximising the purity of hydrogen recycled, while minimising the concentration of hydrogen at the outflow of the gas valve. With a three-section geometry, where the first two sections extract reactor gas, and the last section injects nitrogen gas, it is possible to ensure a concentration of hydrogen gas at the gas valve outlet below the safe limit of 4 %, while maintaining a high concentration of hydrogen gas at the first extraction sections, above 75 %. This high concentration hydrogen gas can be reused and fed back to the inlet of the reactor, reducing the amount of hydrogen required to run the process. Additionally, the analysis shows that it is possible to ensure safe levels of hydrogen at the outlet of the gas valve with the four-section geometry, while using lower flowrates of the flush gas, nitrogen, compared to the current practice, reducing the flowrate by around $5\,\mathrm{L\,min^{-1}}$. Finally a simple dynamic model of the aerogel product is constructed, and the stability of the flow in the reactor with the aerogel presence is calculated. We find that the extraction of the aerogel does not cause a noticeable flow instability in the gas valve.

Part III first introduces the model of the decomposition of the precursors, ferrocene and thiophene. A gradient-based optimisation is used to find the decomposition rate parameters that best predict the experimental data of the decomposition of thiophene. We find that a decomposition rate of $k = 11\,498\,\mathrm{s^{-1}} \exp(-107\,\mathrm{kJ\,mol^{-1}}/RT)$ best describes the behaviour of thiophene in the reactor. Next the optimised decomposition parameters

are used to study the effect of reactor inlet condition on the decomposition of ferrocene and thiophene, comparing a parabolic inlet condition to a jetting inlet condition, at a range of flowrates. We find that, as the flowrate increases from $2\,\mathrm{L\,min^{-1}}$ to $4\,\mathrm{L\,min^{-1}}$, the spatial and temporal separation of the decomposition of ferrocene and thiophene decreases. This effect is significantly stronger when the reactor inlet is a jet instead of a parabolic flow. At flowrates above $3.5\,\mathrm{L\,min^{-1}}$ there is an overlap in the decomposition of both ferrocene and thiophene, where sulphur from thiophene is being released concurrently with the iron from ferrocene. This coexistence of iron and sulphur produces smaller catalyst nanoparticles which are more likely to grow single-walled carbon nanotubes.

Finally, in part IV a model of the particle evolution over the length of the reactor is constructed. This model is used to first estimate the effect of reactor flowrate and input ferrocene concentration on the growth of the particles in the reactor. Next, the model's parameters are optimised with a gradient-based method to find the set of parameters that best explain four different experimental observations, corresponding to four different peak temperatures in the reactor: 1150, 1200, 1250, and 1300 °C. The model is able to predict the mass fraction evolution over the length of the reactor for the experimental cases with a peak reactor temperature of 1250 and 1300 °C. Three parameters are found to have a significant impact on the evaluation of the model: the Kelvin factor governing the condensation and evaporation rate of the particles, and the two decomposition rate parameters that govern the rate at which the iron gas is released. The optimised values of the decomposition rate parameters are comparable with the decomposition rate of thiophene found in part III. This reinforces that the presence of sulphur is necessary for the formation of the nanoparticles in the process.

## 11.1 Future work

Building upon this thesis, the natural next lines of research are improving and extending upon the particle model, and incorporating more experimental data, in order to achieve a more robust and predictive model. The code developed with this study can easily assimilate more data to improve the models, and also be extended to handle different reactor geometries. The current particle model uses a simple model for the particle size distribution, assuming all particles are of the same size. Extending the model to model a wider distribution of particle sizes could improve the predictive abilities of the model. Further, the second order derivative of the particle model could be derived, to improve

the optimisation process and allow the Newton method to be used to find the parameters that best explain the data.

The next step of modelling, the formation of the carbon nanotubes, could also be explored. We know that the majority of the carbon nanotube mass is produced after the mid-point of the reactor (Hoecker et al., 2017a), so a simple model could be constructed that takes into account both the nanoparticles and the carbon source. This model could then be compared with the experimental observations by Hoecker et al. (2017a).

The analysis of the gas valve in chapter 4 could also be improved by using a three-dimensional model for all three geometry configurations to capture the three dimensional structure of the flow, as well as the effect of buoyancy due to the temperature difference between the reactor fluid and the injected nitrogen. The fluid model could also be improved, by modelling the difference in density in the hydrogen gas from the reactor and the nitrogen being injected into the gas valve.

The model of the aerogel could be further extended and different assumptions could be explored. This would require more background work on the meso- and microscale composition and behaviour of the aerogel structure so any model could be compared with experimental observations.

# References


Abhyankar, S., Brown, J., Constantinescu, E. M., Ghosh, D., Smith, B. F., and Zhang, H. (2018). PETSc/TS: A Modern Scalable ODE/DAE Solver Library. *arXiv:1806.01437 [math]*. arXiv: 1806.01437.

Alben, S., Shelley, M., and Zhang, J. (2004). How flexibility induces streamlining in a two-dimensional flow. *Physics of Fluids*, 16(5):1694–1713.

Alnæs, M. S., Blechta, J., Hake, J., Johansson, A., Kehlet, B., Logg, A., Richardson, C., Ring, J., Rognes, M. E., and Wells, G. N. (2015). The FEniCS Project Version 1.5. *Archive of Numerical Software*, 3(100).

Brewster, J. (2019). *Shape Optimisation for Hydrodynamic Stability and its Application to Cyclone Separators*. PhD thesis, Univeristy of Cambridge.

Brown, D. P., Nasibulin, A. G., and Kauppinen, E. I. (2008). CFD-Aerosol Modeling of the Effects of Wall Composition and Inlet Conditions on Carbon Nanotube Catalyst Particle Activity. *Journal of Nanoscience and Nanotechnology*, 8(8):3803–3819.

Bulmer, J. S., Kaniyoor, A., Gspann, T., Mizen, J., Ryley, J., Kiley, P., Ratering, G., Sparreboom, W., Bauhuis, G., Stehr, T., Oudejans, D., Sparkes, M., O'Neill, B., and Elliott, J. A. (2020). Forecasting continuous carbon nanotube production in the floating catalyst environment. *Chemical Engineering Journal*, 390:124497.

Connell, B. S. H. and Yue, D. K. P. (2007). Flapping dynamics of a flag in a uniform stream. *Journal of Fluid Mechanics*, 581:33–67.

Conroy, D., Moisala, A., Cardoso, S., Windle, A., and Davidson, J. (2010). Carbon nanotube reactor: Ferrocene decomposition, iron particle growth, nanotube aggregation and scale-up. *Chemical Engineering Science*, 65(10):2965–2977.

de Boor, C. (1972). On calculating with B-splines. *Journal of Approximation Theory*, 6(1):50–62.

Donea, J., Huerta, A., Ponthot, J.-P., and Rodríguez-Ferran, A. (2004). Arbitrary Lagrangian–Eulerian Methods. In *Encyclopedia of Computational Mechanics*. John Wiley & Sons, Ltd.

Friedlander, S. K. (2000). *Smoke, dust, and haze: fundamentals of aerosol dynamics*. Topics in chemical engineering. Oxford University Press, New York, 2nd ed edition.

Gelbard, F., Tambour, Y., and Seinfeld, J. H. (1980). Sectional representations for simulating aerosol dynamics. *Journal of Colloid and Interface Science*, 76(2):541–556.

Geuzaine, C. and Remacle, J.-F. (2009). Gmsh: A 3-D finite element mesh generator with built-in pre- and post-processing facilities. *International Journal for Numerical Methods in Engineering*, 79(11):1309–1331.

Girshick, S. L. and Chiu, C. (1990). Kinetic nucleation theory: A new expression for the rate of homogeneous nucleation from an ideal supersaturated vapor. *The Journal of Chemical Physics*, 93(2):1273–1277.

Gspann, T. S., Juckes, S. M., Niven, J. F., Johnson, M. B., Elliott, J. A., White, M. A., and Windle, A. H. (2017). High thermal conductivities of carbon nanotube films and micro-fibres and their dependence on morphology. *Carbon*, 114:160–168.

Haynes, W. M., editor (2014). *CRC Handbook of Chemistry and Physics*. CRC Press, Boca Raton, 95 edition.

Hernandez, V., Roman, J. E., and Vidal, V. (2005). SLEPc: A Scalable and Flexible Toolkit for the Solution of Eigenvalue Problems. *ACM Trans. Math. Softw.*, 31(3):351–362.

Hinch, E. J. (2020). *Think Before You Compute: A Prelude to Computational Fluid Dynamics*. Cambridge Texts in Applied Mathematics. Cambridge University Press, Cambridge.

Hoecker, C., Smail, F., Bajada, M., Pick, M., and Boies, A. (2016). Catalyst nanoparticle growth dynamics and their influence on product morphology in a CVD process for continuous carbon nanotube synthesis. *Carbon*, 96:116–124.

Hoecker, C., Smail, F., Pick, M., and Boies, A. (2017a). The influence of carbon source and catalyst nanoparticles on CVD synthesis of CNT aerogel. *Chemical Engineering Journal*, 314:388–395.

Hoecker, C., Smail, F., Pick, M., Weller, L., and Boies, A. M. (2017b). The Dependence of CNT Aerogel Synthesis on Sulfur-driven Catalyst Nucleation Processes and a Critical Catalyst Particle Mass Concentration. *Scientific Reports*, 7(1):14519.

Hou, G., Ng, V., Song, Y., Zhang, L., Xu, C., Shanov, V., Mast, D., Schulz, M., and Liu, Y. (2017). Numerical and Experimental Investigation of Carbon Nanotube Sock Formation. *MRS Advances*, 2(1):21–26.

Hou, G., Su, R., Wang, A., Ng, V., Li, W., Song, Y., Zhang, L., Sundaram, M., Shanov, V., Mast, D., Lashmore, D., Schulz, M., and Liu, Y. (2016). The effect of a convection vortex on sock formation in the floating catalyst method for carbon nanotube synthesis. *Carbon*, 102:513–519.

Kaniyoor, A., Bulmer, J., Gspann, T., Mizen, J., Ryley, J., Kiley, P., Terrones, J., Miranda-Reyes, C., Divitini, G., Sparkes, M., O'Neill, B., Windle, A., and Elliott, J. A. (2019). High throughput production of single-wall carbon nanotube fibres independent of sulfur-source. *Nanoscale*, 11(39):18483–18495.

Koziol, K., Vilatela, J., Moisala, A., Motta, M., Cunniff, P., Sennett, M., and Windle, A. (2007). High-Performance Carbon Nanotube Fiber. *Science*, 318(5858):1892–1895.

Kuwana, K. and Saito, K. (2005). Modeling CVD synthesis of carbon nanotubes: Nanoparticle formation from ferrocene. *Carbon*, 43(10):2088–2095.

Lee, S.-H., Park, J., Kim, H.-R., Lee, J., and Lee, K.-H. (2015). Synthesis of high-quality carbon nanotube fibers by controlling the effects of sulfur on the catalyst agglomeration during the direct spinning process. *RSC Advances*, 5(52):41894–41900.

Lemke, M., Reiss, J., and Sesterhenn, J. (2014). Adjoint based optimisation of reactive compressible flows. *Combustion and Flame*, 161(10):2552–2564.

Li, Y.-L., Kinloch, I. A., and Windle, A. H. (2004). Direct Spinning of Carbon Nanotube Fibers from Chemical Vapor Deposition Synthesis. *Science*, 304(5668):276–278.

Logg, A., Mardal, K.-A., Wells, G. N., and others (2012). *Automated Solution of Differential Equations by the Finite Element Method*. Springer.

Loiseleux, T., Chomaz, J. M., and Huerre, P. (1998). The effect of swirl on jets and wakes: Linear instability of the Rankine vortex with axial flow. *Physics of Fluids*, 10(5):1120–1134.

MacKay, D. J. C. (2003). *Information Theory, Inference and Learning Algorithms*. Cambridge University Press. Google-Books-ID: qKiqkQEACAAJ.

McMurtry, P. A., Jou, W.-H., Riley, J. J., and Metcalfe, R. W. (1986). Direct numerical simulations of a reacting mixing layer with chemical heat release. *AIAA Journal*, 24(6):962–970.

Mittal, R. and Iaccarino, G. (2005). Immersed Boundary Methods. *Annual Review of Fluid Mechanics*, 37(1):239–261.

Motta, M., Kinloch, I., Moisala, A., Premnath, V., Pick, M., and Windle, A. (2007a). The parameter space for the direct spinning of fibres and films of carbon nanotubes. *Physica E: Low-dimensional Systems and Nanostructures*, 37(1):40–43.

Motta, M., Moisala, A., Kinloch, I. A., and Windle, A. H. (2007b). High Performance Fibres from 'Dog Bone' Carbon Nanotubes. *Advanced Materials*, 19(21):3721–3726.

Mukherjee, D., Prakash, A., and Zachariah, M. (2006). Implementation of a discrete nodal model to probe the effect of size-dependent surface tension on nanoparticle formation and growth. *Journal of Aerosol Science*, 37(10):1388–1399.

Nocedal, J. and Wright, S. J. (1999). *Numerical optimization*. Springer series in operations research. Springer, New York.

Panda, S. and Pratsinis, S. (1995). Modeling the synthesis of aluminum particles by evaporation-condensation in an aerosol flow reactor. *Nanostructured Materials*, 5(7-8):755–767.

Papadimitriou, D. I. and Giannakoglou, K. C. (2008). Aerodynamic Shape Optimization Using First and Second Order Adjoint and Direct Approaches. *Archives of Computational Methods in Engineering*, 15(4):447–488.

Peskin, C. S. (1972). Flow patterns around heart valves: A numerical method. *Journal of Computational Physics*, 10(2):252–271.

Phanse, G. M. and Pratsinis, S. E. (1989). Theory for Aerosol Generation in Laminar Flow Condensers. *Aerosol Science and Technology*, 11(2):100–119.

Prakash, A., Bapat, A. P., and Zachariah, M. R. (2003). A Simple Numerical Algorithm and Software for Solution of Nucleation, Surface Growth, and Coagulation Problems. *Aerosol Science and Technology*, 37(11):892–898.

Pratsinis, S. E. and Kim, K.-S. (1989). Particle coagulation, diffusion and thermophoresis in laminar tube flows. *Journal of Aerosol Science*, 20(1):101–111.

Revuelta, A., Sánchez, A. L., and Liñán, A. (2002). Confined axisymmetric laminar jets with large expansion ratios. *Journal of Fluid Mechanics*, 456:319–352.

Sarrate, J., Huerta, A., and Donea, J. (2001). Arbitrary Lagrangian–Eulerian formulation for fluid–rigid body interaction. *Computer Methods in Applied Mechanics and Engineering*, 190(24):3171–3188.

Schlömer, N., Cervone, A., McBain, G., Gokstorp, F., Bussonnier, M., Chen, S., nilswagner, nate sime, and F., F. (2018). nschloe/pygmsh v4.0.8.

Shelley, M. J. and Zhang, J. (2011). Flapping and Bending Bodies Interacting with Fluid Flows. *Annual Review of Fluid Mechanics*, 43(1):449–465.

Stallard, J., Tan, W., Smail, F., Gspann, T., Boies, A., and Fleck, N. (2018). The mechanical and electrical properties of direct-spun carbon nanotube mats. *Extreme Mechanics Letters*, 21:65–75.

Sundaram, R. M., Koziol, K. K. K., and Windle, A. H. (2011). Continuous Direct Spinning of Fibers of Single-Walled Carbon Nanotubes with Metallic Chirality. *Advanced Materials*, 23(43):5064–5068.

Ur Rahman Memon, H., Williams, A., and Williams, P. T. (2003). Shock tube pyrolysis of thiophene. *International Journal of Energy Research*, 27(3):225–239.

Weller, L., Smail, F. R., Elliott, J. A., Windle, A. H., Boies, A. M., and Hochgreb, S. (2019). Mapping the parameter space for direct-spun carbon nanotube aerogels. *Carbon*, 146:789–812.

Whitby, E. R. and McMurry, P. H. (1997). Modal Aerosol Dynamics Modeling. *Aerosol Science and Technology*, 27(6):673–688.

# A Precursor model boundary conditions

The governing equation of the decomposition of the precursor is, under the steady-state assumption:

$$G(c, \boldsymbol{\theta}) \equiv \boldsymbol{\nabla} \cdot (\rho \boldsymbol{u} c) - \boldsymbol{\nabla} \cdot (\rho D_c \boldsymbol{\nabla} c) + \rho c \exp(\beta - T_a/T) = 0, \tag{A.1}$$

where $\beta$ and $T_a$ are the model parameters.

The amount of precursor, $c$, is known and prescribed at the inlet:

$$c = c_0 \text{ on the inlet boundary.} \tag{A.2}$$

We assume that in the steady-state the reactor walls are saturated with precursor molecules, and therefore there are no losses of the precursor to the walls:

$$\rho c(\boldsymbol{u} \cdot \hat{\boldsymbol{n}}) + \rho D_c \frac{\partial c}{\partial n} = 0 \text{ on the wall boundary.} \tag{A.3}$$

At the outlet we use a standard gradient-free condition:

$$\rho D_c \frac{\partial c}{\partial n} = 0 \text{ on the outlet boundary.} \tag{A.4}$$

For the variations of the precursor, $\delta c$, these boundary conditions are:

$$\delta c = 0 \text{ on the inlet boundary,} \tag{A.5}$$

$$\rho(\boldsymbol{u} \cdot \hat{\boldsymbol{n}})\delta c - \rho D_c \frac{\partial \delta c}{\partial n} = 0 \text{ on the wall boundary,} \tag{A.6}$$

$$\rho D_c \frac{\partial \delta c}{\partial n} = 0 \text{ on the outlet boundary.} \tag{A.7}$$

After using the divergence theorem to shift the derivatives from the variations of the precursor $\delta c$ onto the adjoint variable $\lambda$ the adjoint governing equation becomes:

$$-\rho \boldsymbol{u} \cdot \boldsymbol{\nabla} \lambda - \boldsymbol{\nabla} \cdot (\rho D_c \boldsymbol{\nabla} \lambda) + \rho \lambda k = 0, \tag{A.8}$$

with the boundary conditions such that:

$$\begin{aligned}(q-x)\sigma_x^{-1}\frac{\partial q}{\partial c}\delta c + \oint_\Gamma \rho(\boldsymbol{u}\cdot\hat{\boldsymbol{n}})\lambda\delta c + \rho D_c\frac{\partial\lambda}{\partial n}\delta c - \rho D_c\lambda\frac{\partial\delta c}{\partial n}\,\mathrm{d}\Gamma \\ = \oint_{\text{outlet}} \tfrac{1}{A}(c-x)\sigma_x^{-1}\delta c\,\mathrm{d}\Gamma + \oint_\Gamma \rho(\boldsymbol{u}\cdot\hat{\boldsymbol{n}})\lambda\delta c + \rho D_c\frac{\partial\lambda}{\partial n}\delta c - \rho D_c\lambda\frac{\partial\delta c}{\partial n}\,\mathrm{d}\Gamma \\ = 0,\end{aligned} \tag{A.9}$$

where we have projected the difference between the observations $x$ uniformly onto the outlet area to transform $\partial q/\partial c$ onto the modelling domain.

Substituting in (A.5)–(A.7) into (A.9) leaves:

$$\oint_{\text{inlet}} -[\rho D_c\lambda]\frac{\partial\delta c}{\partial n}\,\mathrm{d}\Gamma = 0 \text{ on the inlet,} \tag{A.10}$$

$$\oint_{\text{wall}} \left[\rho D_c\frac{\partial\lambda}{\partial n}\right]\delta c\,\mathrm{d}\Gamma = 0 \text{ on the wall,} \tag{A.11}$$

$$\oint_{\text{outlet}} \left[\tfrac{1}{A}(c-x)\sigma_x^{-1} + \rho(\boldsymbol{u}\cdot\hat{\boldsymbol{n}})\lambda + \rho D_c\frac{\partial\lambda}{\partial n}\right]\delta c\,\mathrm{d}\Gamma = 0 \text{ on the outlet,} \tag{A.12}$$

which gives us the required boundary conditions on the adjoint variable:

$$\lambda = 0 \text{ on the inlet,} \tag{A.13}$$

$$\frac{\partial\lambda}{\partial n} = 0 \text{ on the wall,} \tag{A.14}$$

$$\tfrac{1}{A}(c-x)\sigma_x^{-1} + \rho(\boldsymbol{u}\cdot\hat{\boldsymbol{n}})\lambda + \rho D_c\frac{\partial\lambda}{\partial n} = 0 \text{ on the outlet.} \tag{A.15}$$

## A.1 The second order adjoint variables

The second order adjoint introduces two more governing equations for the two additional adjoint variables, $\boldsymbol{\phi}$ and $\boldsymbol{\psi}$. The first governing equation is for the variations of the adjoint variables, $\lambda$. The boundary conditions (A.13)–(A.15) become:

$$\delta\lambda = 0 \text{ on the inlet,} \tag{A.16}$$

$$\frac{\partial\delta\lambda}{\partial n} = 0 \text{ on the wall,} \tag{A.17}$$

$$\tfrac{1}{A}\sigma_x^{-1}\delta c + \rho(\boldsymbol{u}\cdot\hat{\boldsymbol{n}})\delta\lambda + \rho D_c\frac{\partial\delta\lambda}{\partial n} = 0 \text{ on the outlet.} \tag{A.18}$$

The construction of the two additional governing equations produces the following boundary integrals, which will indicate the boundary conditions:

$$\oint_{\Gamma} -\rho(\boldsymbol{u}\cdot\hat{\boldsymbol{n}})\boldsymbol{\phi}\delta\lambda + \rho D_c\frac{\partial\boldsymbol{\phi}}{\partial n}\delta\lambda - \rho D_c\boldsymbol{\phi}\frac{\partial\delta\lambda}{\partial n}\,\mathrm{d}\Gamma + \oint_{\Gamma}\rho(\boldsymbol{u}\cdot\hat{\boldsymbol{n}})\boldsymbol{\psi}\delta c + \rho D_c\frac{\partial\boldsymbol{\psi}}{\partial n}\delta c - \rho D_c\boldsymbol{\psi}\frac{\partial\delta c}{\partial n}\,\mathrm{d}\Gamma = 0. \tag{A.19}$$

Substituting (A.16)–(A.18) into (A.19) leaves:

$$\oint_{\text{inlet}}\left[-\rho D_c\boldsymbol{\phi}\right]\frac{\partial\delta\lambda}{\partial n}\,\mathrm{d}\Gamma + \oint_{\text{inlet}}\left[-\rho D_c\boldsymbol{\psi}\right]\frac{\partial\delta c}{\partial n}\,\mathrm{d}\Gamma = 0 \text{ on the inlet,} \tag{A.20}$$

$$\oint_{\text{wall}}\left[-\rho(\boldsymbol{u}\cdot\hat{\boldsymbol{n}})\boldsymbol{\phi} + \rho D_c\frac{\partial\boldsymbol{\phi}}{\partial n}\right]\delta\lambda\,\mathrm{d}\Gamma + \oint_{\text{wall}}\left[\rho D_c\frac{\partial\boldsymbol{\psi}}{\partial n}\right]\delta c\,\mathrm{d}\Gamma = 0 \text{ on the wall,} \tag{A.21}$$

$$\oint_{\text{outlet}}\left[\rho D_c\frac{\partial\boldsymbol{\phi}}{\partial n}\right]\delta\lambda\,\mathrm{d}\Gamma + \oint_{\text{outlet}}\left[\tfrac{1}{A}\sigma_x^{-1}\boldsymbol{\phi} + \rho(\boldsymbol{u}\cdot\hat{\boldsymbol{n}})\boldsymbol{\psi} + \rho D_c\frac{\partial\boldsymbol{\psi}}{\partial n}\right]\delta c\,\mathrm{d}\Gamma = 0 \text{ on the outlet,} \tag{A.22}$$

which gives the boundary conditions imposed on $\boldsymbol{\phi}$:

$$\boldsymbol{\phi} = 0 \text{ on the inlet,} \tag{A.23}$$

$$-\rho(\boldsymbol{u}\cdot\hat{\boldsymbol{n}})\boldsymbol{\phi} + \rho D_c\frac{\partial\boldsymbol{\phi}}{\partial n} = 0 \text{ on the wall,} \tag{A.24}$$

$$\frac{\partial\boldsymbol{\phi}}{\partial n} = 0 \text{ on the outlet,} \tag{A.25}$$

and on $\boldsymbol{\psi}$:

$$\boldsymbol{\psi} = 0 \text{ on the inlet,} \tag{A.26}$$

$$\frac{\partial\boldsymbol{\psi}}{\partial n} = 0 \text{ on the wall,} \tag{A.27}$$

$$\tfrac{1}{A}\sigma_x^{-1}\boldsymbol{\phi} + \rho(\boldsymbol{u}\cdot\hat{\boldsymbol{n}})\boldsymbol{\psi} + \rho D_c\frac{\partial\boldsymbol{\psi}}{\partial n} = 0 \text{ on the outlet.} \tag{A.28}$$

# B The particle model first-order adjoint

To derive the adjoint equations of the particle model we begin with the governing equations of the direct model as listed in section 10.2:

$$G_1 \equiv \rho \boldsymbol{u} \cdot \boldsymbol{\nabla} g - \boldsymbol{\nabla} \cdot (\rho D \boldsymbol{\nabla} g) - \rho c k + \rho (g^* I + E) = 0, \tag{B.1}$$

$$G_2 \equiv \rho \boldsymbol{u} \cdot \boldsymbol{\nabla} M - \boldsymbol{\nabla} \cdot (\rho D_p \boldsymbol{\nabla} M) - \rho (I - C) = 0, \tag{B.2}$$

$$G_3 \equiv \rho \boldsymbol{u} \cdot \boldsymbol{\nabla} Y - \boldsymbol{\nabla} \cdot (\rho D_p \boldsymbol{\nabla} Y) - \rho m_1 (g^* I + E) = 0, \tag{B.3}$$

$$G_4 \equiv \rho \boldsymbol{u} \cdot \boldsymbol{\nabla} c - \boldsymbol{\nabla} \cdot (\rho D_c \boldsymbol{\nabla} c) + \rho c k = 0. \tag{B.4}$$

The governing equations are labelled $G_1$ to $G_4$ such that when all are satisfied:

$$\boldsymbol{G}(\boldsymbol{\theta}, \boldsymbol{s}) = \boldsymbol{0}. \tag{B.5}$$

We first define the objective function. Then we derive the adjoint governing equations that allow us to construct the expression for the gradient of the objective function with respect to the model's parameters.

The objective function as defined in section 10.2 is:

$$J(\boldsymbol{\theta}, \boldsymbol{x}) = -\log P(\boldsymbol{\theta} \mid \boldsymbol{x}, H) \tag{B.6}$$

$$= \underbrace{\tfrac{1}{2} (\boldsymbol{\theta} - \boldsymbol{\mu}_{\boldsymbol{\theta}})^\top \boldsymbol{\Sigma}_{\boldsymbol{\theta}}^{-1} (\boldsymbol{\theta} - \boldsymbol{\mu}_{\boldsymbol{\theta}})}_{-\log P(\boldsymbol{\theta}|H)} + \underbrace{\tfrac{1}{2} \left(\boldsymbol{q}(\boldsymbol{s}) - \boldsymbol{x}\right)^\top \boldsymbol{\Sigma}_{\boldsymbol{x}}^{-1} \left(\boldsymbol{q}(\boldsymbol{s}) - \boldsymbol{x}\right)}_{-\log P(\boldsymbol{x}|\boldsymbol{\theta}, M)}$$

$$+ \text{constants}. \tag{B.7}$$

We minimise this objective function $J$ with a gradient-based optimisation process to find the parameters that best described the experimental data. To this end we need the expression of the variations of the objective function with respect to the model's variables, $\boldsymbol{s}$, and model's parameters, $\boldsymbol{\theta}$,

$$\delta J = \underbrace{(\boldsymbol{\theta} - \boldsymbol{\mu}_{\boldsymbol{\theta}})^\top \boldsymbol{\Sigma}_{\boldsymbol{\theta}}^{-1}}_{\partial J / \partial \boldsymbol{\theta}} \delta \boldsymbol{\theta} + \underbrace{\left(\boldsymbol{q}(\boldsymbol{s}) - \boldsymbol{x}\right)^\top \boldsymbol{\Sigma}_{\boldsymbol{x}}^{-1} \frac{\partial \boldsymbol{q}}{\partial \boldsymbol{s}}}_{\partial J / \partial \boldsymbol{s}} \delta \boldsymbol{s}, \tag{B.8}$$

where we also label the term containing the variations with the model's parameters $\delta\boldsymbol{\theta}$ as $\partial J/\partial\boldsymbol{\theta}$, and the term containing the variations with the model's variables $\delta\boldsymbol{s}$ as $\partial J/\partial\boldsymbol{s}$.

## B.1 The first order adjoint

We construct the Lagrangian of the objective function by adding the governing-equations constraint to the objective function $J$,

$$L = J + \langle \boldsymbol{\lambda}, \boldsymbol{G}(\boldsymbol{\theta}, \boldsymbol{s}) \rangle \,, \tag{B.9}$$

where $\boldsymbol{\lambda}$ is the adjoint vector corresponding to the model's variables vector $\boldsymbol{s}$, and the inner product $\langle \boldsymbol{\lambda}, \boldsymbol{G} \rangle$ is an integration of the dot-product over the modelling volume:

$$\langle \boldsymbol{\lambda}, \boldsymbol{G}(\boldsymbol{\theta}, \boldsymbol{s}) \rangle \equiv \int_V \boldsymbol{\lambda} \cdot \boldsymbol{G}(\boldsymbol{\theta}, \boldsymbol{s}) \, \mathrm{d}V. \tag{B.10}$$

We take variations of the Lagrangian (B.9), which we can split into two parts, one that depends on the variations in the model's variables $\delta\boldsymbol{s}$, and one that depends on the variations in the model's parameters $\delta\boldsymbol{\theta}$:

$$\delta L = \delta J + \langle \boldsymbol{\lambda}, \delta\boldsymbol{G}(\boldsymbol{\theta}, \boldsymbol{s}) \rangle \tag{B.11}$$

$$= \frac{\partial J}{\partial \boldsymbol{s}} \delta\boldsymbol{s} + \frac{\partial J}{\partial \boldsymbol{\theta}} \delta\boldsymbol{\theta} + \left\langle \boldsymbol{\lambda}, \frac{\partial \boldsymbol{G}}{\partial \boldsymbol{s}} \delta\boldsymbol{s} \right\rangle + \left\langle \boldsymbol{\lambda}, \frac{\partial \boldsymbol{G}}{\partial \boldsymbol{\theta}} \delta\boldsymbol{\theta} \right\rangle . \tag{B.12}$$

Next we use the divergence theorem to shift the derivatives from the model's variables, $\delta\boldsymbol{s}$ onto the adjoint variables, $\boldsymbol{\lambda}$. The resulting equations and boundary conditions are grouped into $\boldsymbol{G}_{\boldsymbol{s}}^{\dagger}$ for the terms paired with $\delta\boldsymbol{s}$ and $\boldsymbol{G}_{\boldsymbol{\theta}}^{\dagger}$ for the terms paired with $\delta\boldsymbol{\theta}$:

$$\delta L = \frac{\partial J}{\partial \boldsymbol{s}} \delta\boldsymbol{s} + \left\langle \delta\boldsymbol{s}, \boldsymbol{G}_{\boldsymbol{s}}^{\dagger} \boldsymbol{\lambda} \right\rangle + \frac{\partial J}{\partial \boldsymbol{\theta}} \delta\boldsymbol{\theta} + \left\langle \delta\boldsymbol{\theta}, \boldsymbol{G}_{\boldsymbol{\theta}}^{\dagger} \boldsymbol{\lambda} \right\rangle . \tag{B.13}$$

At optimality this expression must be 0 for arbitrary values of $\delta\boldsymbol{s}$. Therefore optimality requires $\frac{\partial J}{\partial \boldsymbol{s}} + \boldsymbol{G}_{\boldsymbol{s}}^{\dagger} \boldsymbol{\lambda} = 0$. The expression for the gradient of the objective function with

respect to the model's parameters is:

$$\delta L = \frac{\partial J}{\partial \boldsymbol{\theta}} \delta \boldsymbol{\theta} + \left\langle \delta \boldsymbol{\theta}, \boldsymbol{G}_{\boldsymbol{\theta}}^{\dagger} \boldsymbol{\lambda} \right\rangle, \tag{B.14}$$

$$\frac{\delta L}{\delta \boldsymbol{\theta}} = \frac{\partial J}{\partial \boldsymbol{\theta}} + \boldsymbol{G}_{\boldsymbol{\theta}}^{\dagger} \boldsymbol{\lambda}. \tag{B.15}$$

The detailed derivation of (B.13) is shown below.

### B.1.1 Deriving the adjoint equations

We start with the variations of the governing equations $\delta \boldsymbol{G}(\boldsymbol{\theta}, \boldsymbol{s})$. To find the variations of the governing equations we first find the variations of the four particle dynamics terms: the nucleation rate $I$, the condensation-evaporation rate $E$, the coagulation rate $C$, and the ferrocene decomposition rate $ck$.

The variation of the ferrocene decomposition rate $ck$ is:

$$\delta(\rho ck) = \rho k \delta c + \rho c \delta k, \tag{B.16}$$

where $\delta k$ is short-hand for the variations of the ferrocene decomposition rate with respect to the decomposition parameters, $(k\delta\beta - k\delta T_a/T)$.

The variation of the particle nucleation rate $I$ (8.11) is:

$$I = \rho g \; n_s \left(2\sigma/\pi m_1\right)^{\frac{1}{2}} \exp\left(\Theta - 4\Theta/27 \ln^2 S_r\right) = I_0 g, \tag{B.17}$$

$$\delta I = \left(1 + 8\Theta/27 \ln^3 S_r\right) \rho n_s \left(2\sigma/\pi m_1\right)^{\frac{1}{2}} \exp\left(\Theta - 4\Theta/27 \ln^2 S_r\right) \delta g \tag{B.18}$$

$$= \left(1 + 8\Theta/27 \ln^3 S_r\right) I_0 \delta g. \tag{B.19}$$

The variation of the coagulation rate $C$ (8.16) is:

$$C = 2 \left(6kT d_{p,0}/\rho_p\right)^{\frac{1}{2}} \rho^2 M^2 = C_0 M^2 \tag{B.20}$$

$$\delta C = \left(6kT/\rho_p d_{p,0}\right)^{\frac{1}{2}} \rho^2 M^2 \delta d_{p,0} + 4 \left(6kT d_{p,0}/\rho_p\right)^{\frac{1}{2}} \rho^2 M \delta M \tag{B.21}$$

$$= \left(C_0/2d_{p,0}\right) M^2 \delta d_{p,0} + 2C_0 M \delta M. \tag{B.22}$$

The variation of the condensation-evaporation term $E$ (8.20) is:

$$E = (RT/2\pi M_m)^{\frac{1}{2}} (6\rho Y/\rho_p d_{p,0}) (\rho g - K n_s) = E_0(\rho g - K n_s) \tag{B.23}$$

$$\begin{aligned}\delta E = {} & (RT/2\pi M_m)^{\frac{1}{2}} (6\rho Y/\rho_p d_{p,0}) \rho\delta g + (RT/2\pi M_m)^{\frac{1}{2}} (6\rho/\rho_p d_{p,0}) (\rho g - K n_s) \delta Y \\ & - (RT/2\pi M_m)^{\frac{1}{2}} (6\rho Y/\rho_p d_{p,0}) \delta K n_s \\ & - (RT/2\pi M_m)^{\frac{1}{2}} \left(6\rho Y/\rho_p d_{p,0}^2\right) (\rho g - K n_s)\delta d_{p,0} \qquad \text{(B.24)} \\ = {} & E_0\rho\delta g + (E_0/Y)(\rho g - K n_s)\delta Y - E_0 n_s \delta K - (E_0/d_{p,0})(\rho g - K n_s)\delta d_{p,0} \qquad \text{(B.25)}\end{aligned}$$

With these variations we can derive the variations of the governing equations:

$$\begin{aligned}\delta G_1 = {} & \rho \boldsymbol{u} \cdot \boldsymbol{\nabla}\delta g - \boldsymbol{\nabla} \cdot (\rho D \boldsymbol{\nabla}\delta g) - \rho\delta(ck) + \rho(I\delta g^* + g^*\delta I + \delta E) \qquad \text{(B.26)} \\ = {} & \rho \boldsymbol{u} \cdot \boldsymbol{\nabla}\delta g - \boldsymbol{\nabla} \cdot (\rho D \boldsymbol{\nabla}\delta g) - \rho k\delta c - \rho c\delta k + \rho I\delta g^* \\ & + \rho g^* \left(1 + 8\Theta/27 \ln^3 S_r\right) I_0 \delta g \\ & + \rho E_0\rho\delta g + \rho(E_0/Y)(\rho g - K n_s)\delta Y \\ & - \rho E_0 n_s \delta K - \rho(E_0/d_{p,0})(\rho g - K n_s)\delta d_{p,0}. \qquad \text{(B.27)}\end{aligned}$$

We now collect the terms that contain variations of the model's variables $\delta\boldsymbol{s}$ and label the collection $(\partial G_1/\partial \boldsymbol{s})\delta\boldsymbol{s}$. Similarly we collect the terms that contain variations of the model's parameters $\boldsymbol{\theta}$ and label the collection $(\partial G_1/\partial\boldsymbol{\theta})\delta\boldsymbol{\theta}$:

$$\delta G_1 = \frac{\partial G_1}{\partial \boldsymbol{s}}\delta\boldsymbol{s} + \frac{\partial G_1}{\partial \boldsymbol{\theta}}\delta\boldsymbol{\theta} \tag{B.28}$$

$$\begin{aligned}= {} & \underbrace{\rho \boldsymbol{u} \cdot \boldsymbol{\nabla}\delta g - \boldsymbol{\nabla} \cdot (\rho D \boldsymbol{\nabla}\delta g) - \rho k\delta c + \rho g^* \left(1 + 8\Theta/27 \ln^3 S_r\right) I_0 \delta g + \cdots}_{(\partial G_1/\partial \boldsymbol{s})\delta\boldsymbol{s}} \\ & \underbrace{\cdots + \rho E_0\rho\delta g + \rho(E_0/Y)(\rho g - K n_s)\delta Y}_{(\partial G_1/\partial \boldsymbol{s})\delta\boldsymbol{s}} \\ & + \underbrace{-\rho c\delta k + \rho I\delta g^* - \rho E_0 n_s \delta K - \rho(E_0/d_{p,0})(\rho g - K n_s)\delta d_{p,0}}_{(\partial G_1/\partial\boldsymbol{\theta})\delta\boldsymbol{\theta}}. \qquad \text{(B.29)}\end{aligned}$$

We repeat this for the remaining governing equations,

$$\delta G_2 = \rho \boldsymbol{u} \cdot \boldsymbol{\nabla} \delta M - \boldsymbol{\nabla} \cdot (\rho D_p \boldsymbol{\nabla} \delta M) - \rho \delta I - \delta C, \tag{B.30}$$

$$= \underbrace{\rho \boldsymbol{u} \cdot \boldsymbol{\nabla} \delta M - \boldsymbol{\nabla} \cdot (\rho D_p \boldsymbol{\nabla} \delta M) - \rho g^* \left(1 + 8\Theta/27 \ln^3 S_r\right) I_0 \delta g - 2\rho C_0 M \delta M}_{(\partial G_2/\partial \boldsymbol{s})\delta \boldsymbol{s}}$$

$$+ \underbrace{-\rho I \delta g^* - \rho (C_0/2d_{p,0}) M^2 \delta d_{p,0}}_{(\partial G_2/\partial \boldsymbol{\theta})\delta \boldsymbol{\theta}}. \tag{B.31}$$

$$\delta G_3 = \rho \boldsymbol{u} \cdot \boldsymbol{\nabla} Y - \boldsymbol{\nabla} \cdot (\rho D_p \boldsymbol{\nabla} Y) - \rho m_1 (g^* I + E), \tag{B.32}$$

$$= \underbrace{\rho \boldsymbol{u} \cdot \boldsymbol{\nabla} \delta Y - \boldsymbol{\nabla} \cdot (\rho D_p \boldsymbol{\nabla} \delta Y) - \rho m_1 g^* \left(1 + 8\Theta/27 \ln^3 S_r\right) I_0 \delta g + \cdots}_{(\partial G_3/\partial \boldsymbol{s})\delta \boldsymbol{s}}$$

$$\underbrace{\cdots - \rho m_1 E_0 \rho \delta g - \rho m_1 (E_0/Y)(\rho g - K n_s)\delta Y}_{(\partial G_3/\partial \boldsymbol{s})\delta \boldsymbol{s}}$$

$$+ \underbrace{\rho m_1 \left(-I \delta g^* + E_0 n_s \delta K + (E_0/d_{p,0})(\rho g - K n_s)\delta d_{p,0}\right)}_{(\partial G_3/\partial \boldsymbol{\theta})\delta \boldsymbol{\theta}}. \tag{B.33}$$

$$\delta G_4 = \rho \boldsymbol{u} \cdot \boldsymbol{\nabla} c - \boldsymbol{\nabla} \cdot (\rho D_c \boldsymbol{\nabla} c) + \rho \delta (ck), \tag{B.34}$$

$$= \underbrace{\rho \boldsymbol{u} \cdot \boldsymbol{\nabla} \delta c - \boldsymbol{\nabla} \cdot (\rho D_c \boldsymbol{\nabla} \delta c) + \rho k \delta c}_{(\partial G_4/\partial \boldsymbol{s})\delta \boldsymbol{s}} + \underbrace{\rho c \delta k}_{(\partial G_4/\partial \boldsymbol{\theta})\delta \boldsymbol{\theta}}. \tag{B.35}$$

Now we introduce the adjoint variables $\boldsymbol{\lambda} = (g^\dagger, M^\dagger, Y^\dagger, c^\dagger)$ and take the volume integral of the adjoint variables vector dotted with the collection of all governing equations. We can split the expression into two parts: one part with the variations with respect to the model's variables, and one part with variations with respect to the model's parameters.

$$\int_V \boldsymbol{\lambda} \cdot \delta \boldsymbol{G}(\boldsymbol{\theta}, \boldsymbol{s}) \, \mathrm{d}V = \int_V \boldsymbol{\lambda} \cdot \frac{\partial \boldsymbol{G}}{\partial \boldsymbol{s}} \delta \boldsymbol{s} \, \mathrm{d}V + \int_V \boldsymbol{\lambda} \cdot \frac{\partial \boldsymbol{G}}{\partial \boldsymbol{\theta}} \delta \boldsymbol{\theta} \, \mathrm{d}V. \tag{B.36}$$

We use the divergence theorem to shift the derivatives from $\delta\boldsymbol{s}$ to the adjoint variables $\boldsymbol{\lambda}$:

$$\int_V \boldsymbol{\lambda}\cdot\delta\boldsymbol{G}(\boldsymbol{\theta},\boldsymbol{s})\,\mathrm{d}V = \int_V \boldsymbol{\lambda}\cdot\frac{\partial\boldsymbol{G}}{\partial\boldsymbol{s}}(\delta\boldsymbol{s})\,\mathrm{d}V + \int_V \boldsymbol{\lambda}\cdot\frac{\partial\boldsymbol{G}}{\partial\boldsymbol{\theta}}\delta\boldsymbol{\theta}\,\mathrm{d}V, \tag{B.37}$$

$$= \int_V \delta\boldsymbol{s}\cdot\boldsymbol{G}^\dagger(\boldsymbol{\lambda})\,\mathrm{d}V + \oint_\Gamma G_\Gamma(\boldsymbol{\lambda},\delta\boldsymbol{s},\hat{\boldsymbol{n}})\,\mathrm{d}\Gamma + \int_V \boldsymbol{\lambda}\cdot\frac{\partial\boldsymbol{G}}{\partial\boldsymbol{\theta}}\delta\boldsymbol{\theta}\,\mathrm{d}V. \tag{B.38}$$

We work through each $\partial\boldsymbol{G}/\partial\boldsymbol{s}$ term separately. For the first governing equation the shifted expression becomes:

$$\begin{aligned}\int_V g^\dagger\frac{\partial G_1}{\partial\boldsymbol{s}}\delta\boldsymbol{s}\,\mathrm{d}V &= \int_V g^\dagger\left[\rho\boldsymbol{u}\cdot\boldsymbol{\nabla}\delta g - \boldsymbol{\nabla}\cdot(\rho D\boldsymbol{\nabla}\delta g)\right]\mathrm{d}V\\ &\quad+\int_V g^\dagger\left[-\rho k\delta c + \rho g^*\left(1+8\Theta/27\ln^3 S_r\right)I_0\delta g\right]\mathrm{d}V\\ &\quad+\int_V g^\dagger\left[\rho E_0\rho\delta g + \rho(E_0/Y)(\rho g - Kn_s)\delta Y\right]\mathrm{d}V, \qquad \text{(B.39)}\\ &= \int_V\left[-\rho\boldsymbol{u}\cdot\boldsymbol{\nabla}g^\dagger - \boldsymbol{\nabla}\cdot\left(\rho D\boldsymbol{\nabla}g^\dagger\right)\right]\delta g\,\mathrm{d}V\\ &\quad+\oint_\Gamma\left[g^\dagger\rho(\boldsymbol{u}\cdot\hat{\boldsymbol{n}}) - \rho D\frac{\partial g^\dagger}{\partial n}\right]\delta g + \left[\rho D g^\dagger\right]\frac{\partial\delta g}{\partial n}\,\mathrm{d}\Gamma\\ &\quad+\int_V\left[-\rho k g^\dagger\right]\delta c\,\mathrm{d}V\\ &\quad+\int_V\left[\rho g^*\left(1+8\Theta/27\ln^3 S_r\right)I_0 g^\dagger + \rho E_0\rho g^\dagger\right]\delta g\,\mathrm{d}V\\ &\quad+\int_V\left[\rho(E_0/Y)(\rho g - Kn_s)g^\dagger\right]\delta Y\,\mathrm{d}V, \qquad \text{(B.40)}\\ &= \int_V \delta\boldsymbol{s}\cdot\boldsymbol{G}^\dagger_{\boldsymbol{s},1}g^\dagger\,\mathrm{d}V = \left\langle\delta\boldsymbol{s},\boldsymbol{G}^\dagger_{\boldsymbol{s},1}g^\dagger\right\rangle. \qquad \text{(B.41)}\end{aligned}$$

The particle number density equation shifts to:

$$\begin{aligned}\int_V M^\dagger \frac{\partial G_2}{\partial \boldsymbol{s}} \delta \boldsymbol{s}\,\mathrm{d}V &= \int_V M^\dagger \left[\rho \boldsymbol{u}\cdot\boldsymbol{\nabla}\delta M - \boldsymbol{\nabla}\cdot(\rho D_p \boldsymbol{\nabla}\delta M)\right]\mathrm{d}V \\ &\quad + \int_V M^\dagger \left[-\rho\left(1+8\Theta/27\ln^3 S_r\right) I_0 \delta g - 2\rho C_0 M \delta M\right]\mathrm{d}V \quad \text{(B.42)} \\ &= \int_V \left[-\rho \boldsymbol{u}\cdot\boldsymbol{\nabla}M^\dagger - \boldsymbol{\nabla}\cdot\left(\rho D_p \boldsymbol{\nabla}M^\dagger\right)\right]\delta M\,\mathrm{d}V \\ &\quad + \oint_\Gamma \left[M^\dagger \rho(\boldsymbol{u}\cdot\hat{\boldsymbol{n}}) - \rho D_p \frac{\partial M^\dagger}{\partial n}\right]\delta M + \left[\rho D_p M^\dagger\right]\frac{\partial \delta M}{\partial n}\,\mathrm{d}\Gamma \\ &\quad + \int_V \left[-\rho\left(1+8\Theta/27\ln^3 S_r\right) J_0 M^\dagger\right]\delta g\,\mathrm{d}V \\ &\quad + \int_V \left[-2\rho C_0 M M^\dagger\right]\delta M\,\mathrm{d}V. \quad \text{(B.43)}\end{aligned}$$

The particle mass fraction equation shifts to:

$$\begin{aligned}\int_V Y^\dagger \frac{\partial G_3}{\partial \boldsymbol{s}} \delta \boldsymbol{s}\,\mathrm{d}V &= \int_V Y^\dagger \left[\rho \boldsymbol{u}\cdot\boldsymbol{\nabla}\delta Y - \boldsymbol{\nabla}\cdot(\rho D_p \boldsymbol{\nabla}\delta Y)\right]\mathrm{d}V \\ &\quad + \int_V Y^\dagger \left[-\rho m_1 g^*\left(1+8\Theta/27\ln^3 S_r\right) I_0 \delta g\right]\mathrm{d}V \\ &\quad + \int_V Y^\dagger \left[-\rho m_1 E_0 \rho \delta g - \rho m_1 (E_0/Y)(\rho g - K n_s)\delta Y\right]\mathrm{d}V, \quad \text{(B.44)} \\ &= \int_V \left[-\rho \boldsymbol{u}\cdot\boldsymbol{\nabla}Y^\dagger - \boldsymbol{\nabla}\cdot\left(\rho D_p \boldsymbol{\nabla}Y^\dagger\right)\right]\delta Y\,\mathrm{d}V \\ &\quad + \oint_\Gamma \left[Y^\dagger \rho(\boldsymbol{u}\cdot\hat{\boldsymbol{n}}) - \rho D_p \frac{\partial Y^\dagger}{\partial n}\right]\delta Y + \left[\rho D_p Y^\dagger\right]\frac{\partial \delta Y}{\partial n}\,\mathrm{d}\Gamma \\ &\quad + \int_V \left[-\rho m_1 g^*\left(1+8\Theta/27\ln^3 S_r\right) I_0 \rho Y^\dagger - \rho m_1 E_0 Y^\dagger\right]\delta g\,\mathrm{d}V \\ &\quad + \int_V \left[-\rho m_1 (E_0/Y)(\rho g - K n_s) Y^\dagger\right]\delta Y\,\mathrm{d}V. \quad \text{(B.45)}\end{aligned}$$

The ferrocene concentration equation shifts to:

$$\begin{aligned}\int_V c^\dagger \frac{\partial G_4}{\partial \boldsymbol{s}} \delta \boldsymbol{s}\,\mathrm{d}V &= \int_V c^\dagger \left[\rho \boldsymbol{u}\cdot\boldsymbol{\nabla}\delta c - \boldsymbol{\nabla}\cdot(\rho D_c \boldsymbol{\nabla}\delta c)\right]\mathrm{d}V + \int_V c^\dagger \left[\rho k \delta c\right]\mathrm{d}V, \quad \text{(B.46)} \\ &= \int_V \left[-\rho \boldsymbol{u}\cdot\boldsymbol{\nabla}c^\dagger - \boldsymbol{\nabla}\cdot\left(\rho D_c \boldsymbol{\nabla}c^\dagger\right)\right]\delta c\,\mathrm{d}V \\ &\quad + \oint_\Gamma \left[c^\dagger \rho(\boldsymbol{u}\cdot\hat{\boldsymbol{n}}) - \rho D_c \frac{\partial c^\dagger}{\partial n}\right]\delta c + \left[\rho D_c c^\dagger\right]\frac{\partial \delta c}{\partial n}\,\mathrm{d}\Gamma \\ &\quad + \int_V \left[\rho k c^\dagger\right]\delta c\,\mathrm{d}V. \quad \text{(B.47)}\end{aligned}$$

We now sum all integrals and combine the terms that share the same variations of the model's variables. Collecting all terms with $\delta g$ gives:

$$\begin{aligned}\int_V \boldsymbol{\lambda}\cdot\frac{\partial \boldsymbol{G}}{\partial g}\delta g\,\mathrm{d}V = &\int_V \left[-\rho\boldsymbol{u}\cdot\boldsymbol{\nabla}g^\dagger - \boldsymbol{\nabla}\cdot\left(\rho D\boldsymbol{\nabla}g^\dagger\right)\right]\delta g\,\mathrm{d}V\\ &+\int_V \left[\rho g^*\left(1+8\Theta/27\ln^3 S_r\right)I_0 g^\dagger + \rho E_0\rho g^\dagger\right]\delta g\,\mathrm{d}V\\ &+\int_V \left[-\rho\left(1+8\Theta/27\ln^3 S_r\right)I_0 M^\dagger\right]\delta g\,\mathrm{d}V\\ &+\int_V \left[-\rho m_1 g^*\left(1+8\Theta/27\ln^3 S_r\right)I_0 Y^\dagger - \rho m_1 E_0\rho Y^\dagger\right]\delta g\,\mathrm{d}V\\ &+\oint_\Gamma\left[g^\dagger\rho(\boldsymbol{u}\cdot\hat{\boldsymbol{n}}) - \rho D\frac{\partial g^\dagger}{\partial n}\right]\delta g + \left[\rho D g^\dagger\right]\frac{\partial\delta g}{\partial n}\,\mathrm{d}\Gamma. \end{aligned} \tag{B.48}$$

Collecting all terms with $\delta M$ we have,

$$\begin{aligned}\int_V \boldsymbol{\lambda}\cdot\frac{\partial \boldsymbol{G}}{\partial M}\delta M\,\mathrm{d}V = &\int_V \left[-\rho\boldsymbol{u}\cdot\boldsymbol{\nabla}M^\dagger - \boldsymbol{\nabla}\cdot\left(\rho D_p\boldsymbol{\nabla}M^\dagger\right)\right]\delta M\,\mathrm{d}V\\ &+\int_V \left[-2\rho C_0 M M^\dagger\right]\delta M\,\mathrm{d}V\\ &+\oint_\Gamma\left[M^\dagger\rho(\boldsymbol{u}\cdot\hat{\boldsymbol{n}}) - \rho D_p\frac{\partial M^\dagger}{\partial n}\right]\delta M + \left[\rho D_p M^\dagger\right]\frac{\partial\delta M}{\partial n}\,\mathrm{d}\Gamma \end{aligned} \tag{B.49}$$

Collecting all terms with $\delta Y$ we have,

$$\begin{aligned}\int_V \boldsymbol{\lambda}\cdot\frac{\partial \boldsymbol{G}}{\partial Y}\delta Y\,\mathrm{d}V = &\int_V \left[-\rho\boldsymbol{u}\cdot\boldsymbol{\nabla}Y^\dagger - \boldsymbol{\nabla}\cdot\left(\rho D_p\boldsymbol{\nabla}Y^\dagger\right)\right]\delta Y\,\mathrm{d}V\\ &+\int_V \left[\rho(E_0/Y)(\rho g - K n_s)g^\dagger\right]\delta Y\,\mathrm{d}V\\ &+\int_V \left[-\rho m_1(E_0/Y)(\rho g - K n_s)Y^\dagger\right]\delta Y\,\mathrm{d}V\\ &+\oint_\Gamma\left[Y^\dagger\rho(\boldsymbol{u}\cdot\hat{\boldsymbol{n}}) - \rho D_p\frac{\partial Y^\dagger}{\partial n}\right]\delta Y + \left[\rho D_p Y^\dagger\right]\frac{\partial\delta Y}{\partial n}\,\mathrm{d}\Gamma. \end{aligned} \tag{B.50}$$

Collecting all terms with $\delta c$ we have,

$$\begin{aligned}\int_V \boldsymbol{\lambda} \cdot \frac{\partial \boldsymbol{G}}{\partial c} \delta c \, \mathrm{d}V = &\int_V \left[ -\rho \boldsymbol{u} \cdot \boldsymbol{\nabla} c^\dagger - \boldsymbol{\nabla} \cdot \left( \rho D_c \boldsymbol{\nabla} c^\dagger \right) \right] \delta c \, \mathrm{d}V \\ &+ \int_V \left[ -\rho k g^\dagger \right] \delta c \, \mathrm{d}V \\ &+ \int_V \left[ \rho k c^\dagger \right] \delta c \, \mathrm{d}V \\ &+ \oint_\Gamma \left[ c^\dagger \rho (\boldsymbol{u} \cdot \hat{\boldsymbol{n}}) - \rho D_c \frac{\partial c^\dagger}{\partial n} \right] \delta c + \left[ \rho D_c c^\dagger \right] \frac{\partial \delta c}{\partial n} \, \mathrm{d}\Gamma. \end{aligned} \tag{B.51}$$

The last remaining term with a variation of the model's variables $\delta \boldsymbol{s}$ is the variation in the objective function $(\partial J / \partial \boldsymbol{s}) \delta \boldsymbol{s}$:

$$\frac{\partial J}{\partial \boldsymbol{s}} \delta \boldsymbol{s} = \left( \boldsymbol{q}(\boldsymbol{s}) - \boldsymbol{x} \right)^\top \boldsymbol{\Sigma}_{\boldsymbol{x}}^{-1} \frac{\partial \boldsymbol{q}}{\partial \boldsymbol{s}} \delta \boldsymbol{s} \tag{B.52}$$

$$= \left( \boldsymbol{q}(\boldsymbol{s}) - \boldsymbol{x} \right)^\top \boldsymbol{\Sigma}_{\boldsymbol{x}}^{-1} \frac{\partial \boldsymbol{q}}{\partial Y} \delta Y. \tag{B.53}$$

The objective function only depends on the particle mass fraction $Y$, so we add (B.53) to (B.50):

$$\begin{aligned}\int_V \boldsymbol{\lambda} \cdot \frac{\partial \boldsymbol{G}}{\partial Y} \delta Y \, \mathrm{d}V + \frac{\partial J}{\partial \boldsymbol{s}} \delta \boldsymbol{s} = &\int_V \left[ -\rho \boldsymbol{u} \cdot \boldsymbol{\nabla} Y^\dagger - \boldsymbol{\nabla} \cdot \left( \rho D_p \boldsymbol{\nabla} Y^\dagger \right) \right] \delta Y \, \mathrm{d}V \\ &+ \int_V \left[ \rho (E_0 / Y)(\rho g - K n_s) g^\dagger \right] \delta Y \, \mathrm{d}V \\ &+ \int_V \left[ -\rho m_1 (E_0 / Y)(\rho g - K n_s) Y^\dagger \right] \delta Y \, \mathrm{d}V \\ &+ \left[ \left( \boldsymbol{q}(\boldsymbol{s}) - \boldsymbol{x} \right)^\top \boldsymbol{\Sigma}_{\boldsymbol{x}}^{-1} \frac{\partial \boldsymbol{q}}{\partial Y} \right] \delta Y \\ &+ \oint_\Gamma \left[ Y^\dagger \rho (\boldsymbol{u} \cdot \hat{\boldsymbol{n}}) - \rho D_p \frac{\partial Y^\dagger}{\partial n} \right] \delta Y + \left[ \rho D_p Y^\dagger \right] \frac{\partial \delta Y}{\partial n} \, \mathrm{d}\Gamma. \end{aligned} \tag{B.54}$$

We now choose the adjoint variables $\boldsymbol{\lambda}$ in order to ensure all the expressions with the variations of the model's variables (B.48), (B.49), (B.51), and (B.54) are equal to zero.

This gives us the following governing equations for the adjoint variables:

$$\begin{aligned} G_g^\dagger \equiv & -\rho \boldsymbol{u} \cdot \boldsymbol{\nabla} g^\dagger - \boldsymbol{\nabla} \cdot \left(\rho D \boldsymbol{\nabla} g^\dagger\right) + \rho g^* \left(1 + 8\Theta/27 \ln^3 S_r\right) I_0 g^\dagger + \rho E_0 \rho g^\dagger \\ & - \rho \left(1 + 8\Theta/27 \ln^3 S_r\right) I_0 M^\dagger \\ & - \rho m_1 g^* \left(1 + 8\Theta/27 \ln^3 S_r\right) I_0 Y^\dagger - \rho m_1 E_0 \rho Y^\dagger = 0, \end{aligned} \tag{B.55}$$

$$\left[ g^\dagger \rho (\boldsymbol{u} \cdot \hat{\boldsymbol{n}}) - \rho D \frac{\partial g^\dagger}{\partial n} \right] \delta g + \left[\rho D g^\dagger\right] \frac{\partial \delta g}{\partial n} = 0 \text{ on boundaries}, \tag{B.56}$$

$$G_M^\dagger \equiv -\rho \boldsymbol{u} \cdot \boldsymbol{\nabla} M^\dagger - \boldsymbol{\nabla} \cdot \left(\rho D_p \boldsymbol{\nabla} M^\dagger\right) - 2\rho C_0 M M^\dagger = 0, \tag{B.57}$$

$$\left[ M^\dagger \rho (\boldsymbol{u} \cdot \hat{\boldsymbol{n}}) - \rho D_p \frac{\partial M^\dagger}{\partial n} \right] \delta M + \left[\rho D_p M^\dagger\right] \frac{\partial \delta M}{\partial n} = 0 \text{ on boundaries}, \tag{B.58}$$

$$\begin{aligned} G_Y^\dagger \equiv & -\rho \boldsymbol{u} \cdot \boldsymbol{\nabla} Y^\dagger - \boldsymbol{\nabla} \cdot \left(\rho D_p \boldsymbol{\nabla} Y^\dagger\right) - \rho m_1 (E_0/Y)(\rho g - K n_s) Y^\dagger \\ & + \rho (E_0/Y)(\rho g - K n_s) g^\dagger \\ & + \left[ (\boldsymbol{q}(\boldsymbol{s}) - \boldsymbol{x})^\top \boldsymbol{\Sigma}_{\boldsymbol{x}}^{-1} \frac{\partial \boldsymbol{q}}{\partial Y} \right]_{\text{projected}} = 0, \end{aligned} \tag{B.59}$$

$$\left[ Y^\dagger \rho (\boldsymbol{u} \cdot \hat{\boldsymbol{n}}) - \rho D_p \frac{\partial Y^\dagger}{\partial n} \right] \delta Y + \left[\rho D_p Y^\dagger\right] \frac{\partial \delta Y}{\partial n} = 0 \text{ on boundaries}, \tag{B.60}$$

$$G_c^\dagger \equiv -\rho \boldsymbol{u} \cdot \boldsymbol{\nabla} c^\dagger - \boldsymbol{\nabla} \cdot \left(\rho D_c \boldsymbol{\nabla} c^\dagger\right) - \rho k g^\dagger + \rho k c^\dagger = 0, \tag{B.61}$$

$$\left[ c^\dagger \rho (\boldsymbol{u} \cdot \hat{\boldsymbol{n}}) - \rho D_c \frac{\partial c^\dagger}{\partial n} \right] \delta c + \left[\rho D_c c^\dagger\right] \frac{\partial \delta c}{\partial n} = 0 \text{ on boundaries}. \tag{B.62}$$

The adjoint boundary conditions depend on the boundary conditions of the direct equation. The particle model has the following boundary conditions:

$$\delta g = \delta M = \delta Y = 0 \text{ on the wall and inlet}, \tag{B.63}$$

$$\frac{\partial \delta g}{\partial n} = \frac{\partial \delta M}{\partial n} = \frac{\partial \delta Y}{\partial n} = 0 \text{ on the outlet}, \tag{B.64}$$

$$\delta c = 0 \text{ on the inlet}, \tag{B.65}$$

$$\frac{\partial \delta c}{\partial n} = 0 \text{ on the wall and outlet}. \tag{B.66}$$

Therefore, the adjoint boundary conditions that cancel the adjoint boundary integrals are:

$$g^\dagger = M^\dagger = Y^\dagger = 0 \text{ on the wall and inlet,} \tag{B.67}$$

$$\frac{\partial g^\dagger}{\partial n} = \frac{\partial M^\dagger}{\partial n} = \frac{\partial Y^\dagger}{\partial n} = 0 \text{ on the outlet,} \tag{B.68}$$

$$c^\dagger = 0 \text{ on the inlet,} \tag{B.69}$$

$$\frac{\partial c^\dagger}{\partial n} = 0 \text{ on the wall and outlet.} \tag{B.70}$$

And the final adjoint governing equations are:

$$\begin{aligned} G_g^\dagger \equiv & -\rho \boldsymbol{u} \cdot \boldsymbol{\nabla} g^\dagger - \boldsymbol{\nabla} \cdot \left(\rho D \boldsymbol{\nabla} g^\dagger\right) + \rho g^* \left(1 + 8\Theta/27 \ln^3 S_r\right) I_0 g^\dagger + \rho E_0 \rho g^\dagger \\ & - \rho \left(1 + 8\Theta/27 \ln^3 S_r\right) I_0 M^\dagger \\ & - \rho m_1 g^* \left(1 + 8\Theta/27 \ln^3 S_r\right) I_0 Y^\dagger - \rho m_1 E_0 \rho Y^\dagger = 0, \end{aligned} \tag{B.71}$$

$$G_M^\dagger \equiv -\rho \boldsymbol{u} \cdot \boldsymbol{\nabla} M^\dagger - \boldsymbol{\nabla} \cdot \left(\rho D_p \boldsymbol{\nabla} M^\dagger\right) - 2\rho C_0 M M^\dagger = 0, \tag{B.72}$$

$$\begin{aligned} G_Y^\dagger \equiv & -\rho \boldsymbol{u} \cdot \boldsymbol{\nabla} Y^\dagger - \boldsymbol{\nabla} \cdot \left(\rho D_p \boldsymbol{\nabla} Y^\dagger\right) - \rho m_1 (E_0/Y)(\rho g - K n_s) Y^\dagger \\ & + \rho (E_0/Y)(\rho g - K n_s) g^\dagger \\ & + f(Y) = 0, \end{aligned} \tag{B.73}$$

$$G_c^\dagger \equiv -\rho \boldsymbol{u} \cdot \boldsymbol{\nabla} c^\dagger - \boldsymbol{\nabla} \cdot \left(\rho D_c \boldsymbol{\nabla} c^\dagger\right) - \rho k g^\dagger + \rho k c^\dagger = 0, \tag{B.74}$$

where $f_i$ is the forcing produced by the projection of the variation of the objective function, $\delta J$.

The objective function term added to the governing equation of $Y^\dagger$ needs to be treated with care, since we need to make the model predictions compatible with the experimental measurement points. A solution that works and produces good results is to linearly interpolate the experimental measurements onto the modelling mesh, assuming a uniform value in the radial direction. This allows us to use the same volume integral for calculating the objective function as we use for deriving the adjoint equations. A more mathematically rigorous approach would be to project the model prediction onto the experimental points (which is easy), and then project the difference between the prediction and the observation back onto the modelling mesh (which is hard). Figure B.1 shows how such a projeting may look like. As there was not time to perfect the projection method, we use a simple linear interpolation of the observations to construct $(\boldsymbol{q}(\boldsymbol{s}) - \boldsymbol{x})^\top \boldsymbol{\Sigma}_{\boldsymbol{x}}^{-1} \partial \boldsymbol{q} / \partial Y$.

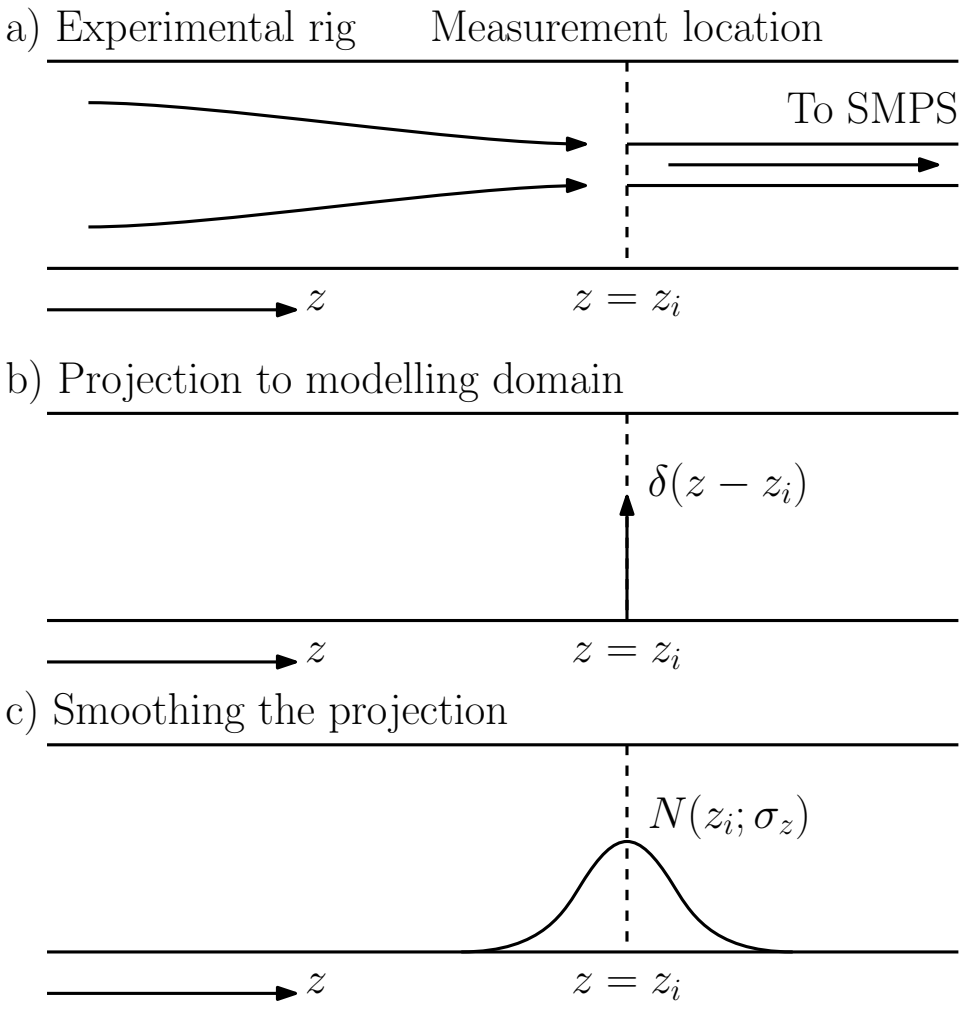


Figure B.1 Projection of the difference between the observations and model prediction $(\boldsymbol{q}(\boldsymbol{s}) - \boldsymbol{x})$ onto the modelling domain. The difference is a scalar value measured at a position $z_i$. This is first projected uniformly as a 1-dimensional line across the diameter of the reactor. Then this is further projected and smoothed-out as a Gaussian curve centred at $z_i$.

After removing the variations in the model's variables with the choice of the adjoint variables $\boldsymbol{\lambda}$ we are left with the terms that contain the variations of the model's parameters, $\langle \boldsymbol{\lambda}, \partial \boldsymbol{G}/\partial \boldsymbol{\theta} \delta \boldsymbol{\theta} \rangle$. Because the term $\partial \boldsymbol{G}/\partial \boldsymbol{\theta}$ does not contain any derivatives, the adjoint transform is linear and we have:

$$\left\langle \boldsymbol{\lambda}, \left( \frac{\partial \boldsymbol{G}}{\partial \boldsymbol{\theta}} \right) \delta \boldsymbol{\theta} \right\rangle = \left\langle \left( \frac{\partial \boldsymbol{G}}{\partial \boldsymbol{\theta}} \right) \boldsymbol{\lambda}, \delta \boldsymbol{\theta} \right\rangle = \left\langle \boldsymbol{G}_{\boldsymbol{\theta}}^{\dagger} \boldsymbol{\lambda}, \delta \boldsymbol{\theta} \right\rangle, \tag{B.75}$$

$$\begin{aligned} &= \int_V g^{\dagger} \frac{\partial G_1}{\partial \boldsymbol{\theta}} \delta \boldsymbol{\theta} \, \mathrm{d}V + \int_V M^{\dagger} \frac{\partial G_2}{\partial \boldsymbol{\theta}} \delta \boldsymbol{\theta} \, \mathrm{d}V + \int_V Y^{\dagger} \frac{\partial G_3}{\partial \boldsymbol{\theta}} \delta \boldsymbol{\theta} \, \mathrm{d}V \\ &\quad + \int_V c^{\dagger} \frac{\partial G_4}{\partial \boldsymbol{\theta}} \delta \boldsymbol{\theta} \, \mathrm{d}V, \end{aligned} \tag{B.76}$$

without any boundary conditions.

We group the terms in (B.29), (B.31), (B.33), and (B.35) by the variation in the model parameter $\delta \boldsymbol{\theta}$:

$$\left\langle \boldsymbol{G}_{\boldsymbol{\theta}}^{\dagger} \boldsymbol{\lambda}, \delta \boldsymbol{\theta} \right\rangle_{\delta k} = \int_V \left[ -g^{\dagger} \rho c \right] \delta k \, \mathrm{d}V + \int_V \left[ c^{\dagger} \rho c \right] \delta k \, \mathrm{d}V \tag{B.77}$$

$$= \int_V \rho c \left( c^{\dagger} - g^{\dagger} \right) \delta k \, \mathrm{d}V \tag{B.78}$$

$$= \int_V \rho c \left( c^{\dagger} - g^{\dagger} \right) \left( k \delta \beta - \delta T_a k / T \right) \mathrm{d}V \tag{B.79}$$

$$\left\langle G_{\boldsymbol{\theta}}^{\dagger} \boldsymbol{\lambda}, \delta g^* \right\rangle = \int_V \left[ g^{\dagger} \rho I \right] \delta g^* \, \mathrm{d}V \int_V \left[ -M^{\dagger} \rho I \right] \delta g^* \, \mathrm{d}V \int_V \left[ -Y^{\dagger} \rho I \right] \delta g^* \, \mathrm{d}V \tag{B.80}$$

$$= \int_V \left[ \rho I \left( g^{\dagger} - M^{\dagger} - Y^{\dagger} \right) \right] \delta g^* \, \mathrm{d}V \tag{B.81}$$

$$\left\langle G_{\boldsymbol{\theta}}^{\dagger} \boldsymbol{\lambda}, \delta K \right\rangle = \int_V \left[ -\rho E_0 n_s g^{\dagger} \right] \delta K \, \mathrm{d}V + \int_V \left[ \rho m_1 E_0 n_s Y^{\dagger} \right] \delta K \, \mathrm{d}V \tag{B.82}$$

$$= \int_V \left[ \rho m_1 E_0 n_s Y^{\dagger} - \rho E_0 n_s g^{\dagger} \right] \delta K \, \mathrm{d}V \tag{B.83}$$

$$\begin{aligned}\left\langle G_{\boldsymbol{\theta}}^{\dagger}\boldsymbol{\lambda}, \delta d_{p,0}\right\rangle &= \int_V \left[-\rho(E_0/d_{p,0})(n - Kn_s)g^{\dagger}\right] \delta d_{p,0}\,\mathrm{d}V \\ &\quad + \int_V \left[-\rho(C_0/2d_{p,0})M^2M^{\dagger}\right] \delta d_{p,0}\,\mathrm{d}V \\ &\quad + \int_V \left[\rho m_1(E_0/d_{p,0})(\rho g - Kn_s)Y^{\dagger}\right] \delta d_{p,0}\,\mathrm{d}V \qquad \text{(B.84)} \\ &= \int_V \rho(E_0/d_{p,0})(\rho g - Kn_s)\left[m_1Y^{\dagger} - g^{\dagger}\right] \delta d_{p,0}\,\mathrm{d}V \\ &\quad + \int_V \left[-\rho(C_0/2d_{p,0})M^2M^{\dagger}\right] \delta d_{p,0}\,\mathrm{d}V \qquad \text{(B.85)}\end{aligned}$$

We now have the required expressions to substitute into the expression of $\delta L$ (B.14). For each parameter, we add the Bayesian prior term, which gives us the final gradient term of the objective function,

$$\frac{\partial L}{\partial \beta} = (\beta - \mu_\beta)\sigma_\beta + \int_V \rho c\left(c^{\dagger} - g^{\dagger}\right) k\,\mathrm{d}V, \qquad \text{(B.86)}$$

$$\frac{\partial L}{\partial T_a} = (T_a - \mu_{T_a})\sigma_{T_a} + \int_V -\rho c\left(c^{\dagger} - g^{\dagger}\right) k/T\,\mathrm{d}V, \qquad \text{(B.87)}$$

$$\frac{\partial L}{\partial g^*} = (g^* - \mu_{g^*})\sigma_{g^*} + \int_V \rho I g^{\dagger} - \rho I M^{\dagger} - \rho I Y^{\dagger}\,\mathrm{d}V, \qquad \text{(B.88)}$$

$$\frac{\partial L}{\partial K} = (K - \mu_K)\sigma_K + \int_V \rho m_1 E_0 n_s Y^{\dagger} - \rho E_0 n_s g^{\dagger}\,\mathrm{d}V, \qquad \text{(B.89)}$$

$$\begin{aligned}\frac{\partial L}{\partial d_{p,0}} &= (d_{p,0} - \mu_{d_{p,0}})\sigma_{d_{p,0}} + \int_V \rho(E_0/d_{p,0})(\rho g - Kn_s)\left[m_1Y^{\dagger} - g^{\dagger}\right]\mathrm{d}V \\ &\quad + \int_V -\rho(C_0/2d_{p,0})M^2M^{\dagger}\,\mathrm{d}V, \qquad \text{(B.90)}\end{aligned}$$

where $\mu$ is the parameter prior mean, and $\sigma$ is the parameter prior deviation.